Theoretical Study on Activation Mechanism of Unreactive Bonds by Metal Cluster Catalysts

Ray Miyazaki

Hokkaido University

2020

金属クラスター触媒による
不活性結合の活性化機構に関する理論的研究

宮崎 玲

北海道大学

2020

Contents

Chapter 5. Theoretical Study for C-H bond Activation on Pd Cluster: Agostic Interaction on Pd Cluster Induced by OAc Ligands

Chapter 1.

General Introduction

1.1 Chemical Reactions with Catalysts

Making and breaking chemical bonds are one of the central issues of chemistry. Various chemical compounds are synthesized as the product of chemical reactions with bond making and/or bond breaking. However, a large amount of energy is usually required for breaking chemical bonds. For example, bond energy of O_2 is 500 kJ/mol, and CO oxidation reaction in gas phase requires 600 ℃ for O-O bond cleavage. On the other hand, CO oxidation can proceed under room temperature in the presence of the catalyst[1]. A schematic potential energy diagram for a model chemical reaction with the catalyst is shown as green line in Figure 1. The first step of the catalytic chemical reaction is adsorption of reactant molecules on catalyst surface. In this step, chemical bonds are formed between the adsorbates and catalyst. After the adsorption, reactant molecules (e.g. CO and O) react on the catalytic surface. Because this reaction proceeds with keeping bonds between the reactants and catalyst, probability for collision between reactants on two-dimensional catalyst surface is larger than that in three-dimensional gas phase. In addition, chemical bonds of the reactant molecules (e.g. O-O bond of O_2) are activated by the interaction with the catalyst. These effects reduce activation energy of the reaction being lower than that without catalyst (red line in Figure 1). After the reaction, the product molecule is desorbed from the catalyst surface, and the catalyst returns to the initial state. This is typical catalytic cycle based on Langmuir-Hinshelwood mechanism[2].

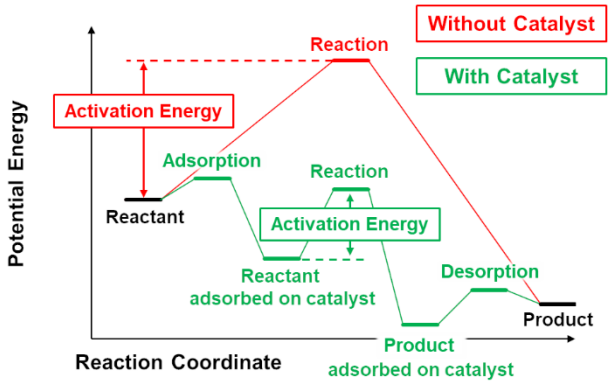

Figure 1. Schematic potential energy diagram of model chemical reaction with catalyst (green line) and without catalyst (red line).

1.2 Activation of Unreactive Bonds

Catalyst design for activation of unreactive bond is both fundamental and forefront issue in catalytic chemistry, which is explained here with the methane activation as an example. Methane is a main component of natural gas, and it is one of the abundant carbon resources. Conversion of methane to useful chemical compounds or fuels are highly desired. The dehydrogenative conversion of methane (DCM) is one of the straightforward process for the synthesis of higher hydrocarbons from methane. However, high reaction temperature (> 2000 K) is required for the C-H bond activation of methane due to the strong C(sp^3)-H bond (bond energy = 438 kJ/mol)[3]. Therefore, the C(sp^3)-H bond of methane can be considered as the *unreactive bond*. The activation of unreactive bond is achieved by using appropriate catalysts. For example, methane-to-benzene transformation via DCM proceeds at 973 K by using the Mo/zeolite catalyst[4]. However, coke formation deactivates the catalyst due to the carbon deposition. This result indicated that too strong catalyst or reaction condition induce over activation of methane, and decomposition to C and H_2 proceeds. Therefore, the *moderately active* catalytic system for the

selective C-H bond activation is important to enhance selectivity of products and reusability of the catalyst. Designing such moderately active catalytic system is a very challenging issue, and this arises from the difficulty of the activation of unreactive bonds. Recently, methane conversion to higher hydrocarbons without the carbon deposition were achieved by using single Fe catalyst in a silica matrix[5] and liquid indium catalyst[3]. Investigation and understanding of the reaction mechanisms on these efficient catalysts are one of the effective way to obtain the guidelines for designing new catalytic systems[6].

1.3 Shape of Catalysts and Active Sites

1.3.1 Homogeneous and Heterogeneous

Catalysts are generally divided into two types: homogeneous catalysts and heterogeneous catalysts. These two types of catalysts are focused on in this section although bio catalysts are also reported recently.

In homogeneous catalysts, reactants, products and catalysts are in same phase (e.g. liquid phase). One of the typical example of homogeneous catalysts is transition metal complex catalysts. In this class of catalysts, the active metal center is stabilized by ligands. The character of the catalyst can be modified precisely by controlling the bulkiness of the ligands or the electronic interaction between the metal center and the ligands. Therefore, the metal complex catalysts show high activity and selectivity for the target reactions through the ligand design.

In heterogeneous catalysts, reaction occurs at interfaces. Reactants and catalysts are in different phases (e.g. gas phase and solid phase, respectively). Therefore, separation of the catalyst and the product is comparably easy in the heterogeneous catalytic system. In addition, cleaning and reuse of the catalyst are also readily due to the same reason. These are one of the great advantages of the heterogeneous catalyst from the perspective of running cost of the

catalytic system and environmental aspects. From these advantages, heterogeneous catalysts are widely used as industrial catalysts. However, improvement of the selectivity is one of the challenges in the heterogeneous catalyst development.

Why the improvement of the selectivity is difficult in the heterogeneous catalyst? Because of the heterogeneity in the surface structure of the heterogeneous catalyst, there are a lot of regions or sites for the adsorption and the reaction in the catalyst. Therefore, it is difficult to know exactly where the reaction proceeds and what structure is optimal for the reaction. Such optimal sites where the reaction takes place are called active sites. In the heterogeneous catalyst, there are not only the active sites for the desired reaction but also those for the undesired reactions. In addition, the desired active sites are sometimes blocked by both products and byproducts, which causes the deactivation of the catalyst as written in Section 1.2. Therefore, the principles of the catalyst design should be developed by accumulating the knowledges of the active sites.

1.3.2 Active Sites of Supported Metal Catalyst

In this subsection, more details for the active sites of the heterogeneous catalysts and its complexity are discussed. Supported metal catalysts are one of the widely used heterogeneous catalysts. For example, it is used as automobile catalysts for exhaust gas cleaning. In this type of catalysts, metal nanoparticles are highly dispersed on the supporting materials (e.g. metal oxide).

As shown in Figure 2, there are several types of active sites in the supported metal catalysts. For example, perimeter region around the interface between the metal nanoparticle and the support material is known as one the typical and the unique active site of the supported metal catalyst[7-11]. Because the metal nanoparticle at the perimeter region is affected by the support, the situation (e.g. electronic structure) around the perimeter is different from the pure metallic surface where far from the support. Such interaction between the metal nanoparticle and the

support is known as the metal-support interaction. While broad meanings are contained in the metal-support interaction, electron transfer between the metal nanoparticle and the support material (electronic metal support interaction: EMSI)[9, 12] is one of the important interaction. For example, charge transfer from Pt nanoparticle to cerium oxide was reported, and it enhances water dissociation on the Pt/CeO_2 catalyst[13].

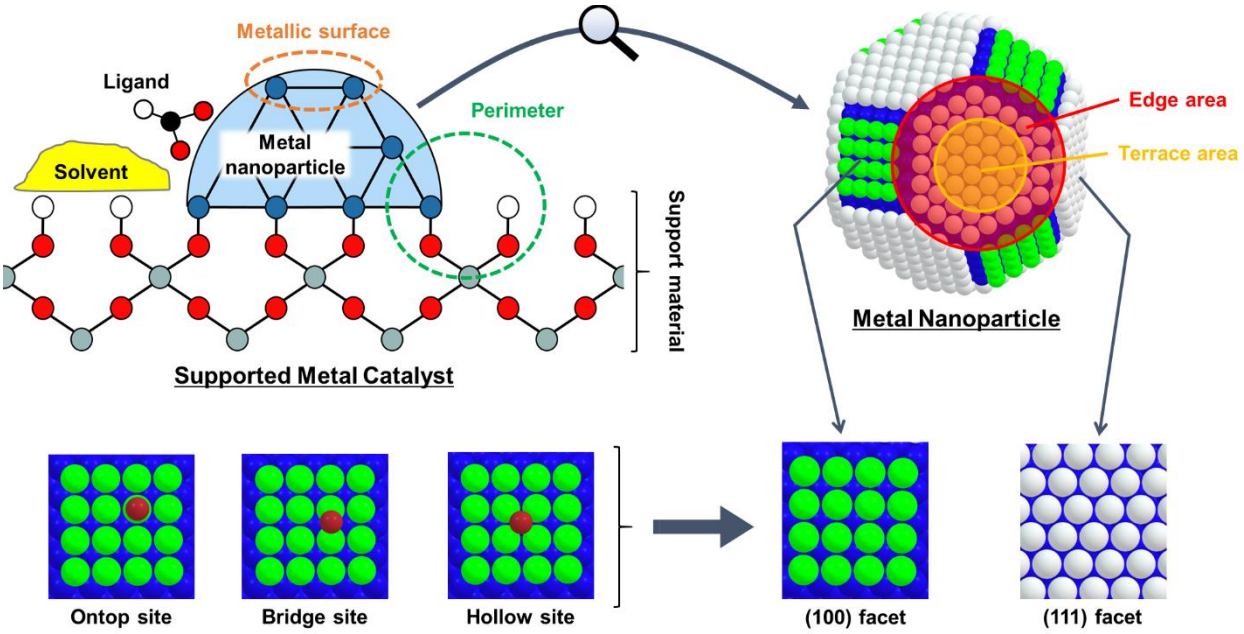

Figure 2. Schematic picture of the supported metal catalyst and its active sites.

Aside from the effect of the metal-support interaction, the metal nanoparticle itself also has several active sites (Figure 2). One of the advantages of the nanostructured metal is large specific surface area compared with the bulk structure. The surface of the metal nanoparticle can be divided into terrace area and edge area. The terrace area is closed packed flat surface. The edge area is in the terminal of the flat surface, and it is constructed by low-coordinated atoms. Such low-coordinated atoms in the edge area are also divided into several types; step, kink, corner and so on. These atoms are also considered as important active sites because the reactants are

strongly adsorbed and activated by the unsaturated atoms. Another advantage of nanostructured metal is high edge area ratio due to the polyhedral structure.

The polyhedral structure of the metal nanoparticle is constructed by the combination of different surface structures (facets) as shown in Figure 2. It was reported that there are some reactions which are affected by the surface structure[14-16]. Such reactions are called by structure sensitive reaction. For example, in the Fisher-Tropsch reaction on the ruthenium nanoparticle catalyst, the CO dissociation reaction proceeds on the specific step site[16]. In addition, several types of adsorption sites are contained in each facet. Examples of adsorption sites for single atom adsorption on the (100) facet of Pd nanoparticle were shown at bottom left in Figure 2 (a red ball indicates adsorption sites). In this case, there are three types of adsorption sites; ontop site (just above the Pd atom), bridge site (between two Pd atoms) and hollow site (hollow surrounded by four Pd atoms). Obviously, adsorption sites or adsorption modes vary by each facet, and the optimal adsorption site also varies depending on the combination of the adsorbate and metal. Because the adsorption is the first step of the catalytic reaction as shown in Section 1.1, investigating the adsorption mode (e.g. adsorption structure or energy) on each active site is also important step for understanding the catalytic reaction.

Furthermore, there are effects from other factors; solvents, ligands and so on. For example, it was reported that low temperature oxidation of CO on the Au/TiO_2 catalyst is accelerated by the presence of water[17, 18]. In addition, defect sites may exist in the metal surface or the support material although very clean (ordered) structure was supposed in Figure 2. Actually, it was reported that electron transfer from the support to Au cluster is induced by oxygen vacancy of MgO support[19].

As written in above, there are a lot of active sites in the supported metal catalyst. Therefore, it is difficult to figure out which reaction proceeds at a particular active site. In other words, elucidation of the reaction mechanism on the heterogeneous catalyst is a difficult task. However, understanding the structure and reactivity of the active site is required for new catalyst design. Therefore, we have to tackle this task by using all the possible methods.

1.4 Theoretical Chemistry for Catalytic Systems

As discussed in former sections, investigating and understanding the active sites of the catalyst is the important step to obtain the guides lines for the catalyst design. In other words, understanding the reaction mechanisms on the catalytic system is required for the development of the new catalyst. However, the actual catalytic system is very complicated system composed of several active sites and ingredients. Therefore, it is hard to figure out what is going on the catalyst, and what the nature of the catalytic activity is.

Theoretical (computational) chemistry is one of the effective way to investigate the reaction mechanism of the catalyst. Because the chemical reaction is governed by electrons, the reaction mechanism can be described by electronic state theory calculation based on the Schrödinger equation. For example, geometries and energies of the intermediate states and transition states are obtained by theoretical calculations. Consequently, the potential energy surfaces (in which the intermediates and transition states are extreme values) for the catalytic reaction are formed. Based on these calculations, several reaction pathways on each active site can be investigated. Furthermore, the key character of the catalyst is detected by the electronic structures of the catalyst materials. Therefore, we can tackle the difficult subjects through theoretical chemistry; what is going on the catalyst, and what the nature of the catalytic activity is.

1.4.1 Density Functional Theory

The solution of the Schrödinger equation is the exact electronic energy and the related wave functions of the system. However, we cannot access the exact solution of the Schrödinger equation for many-body (electrons) systems because N-electron wave function is 3N dimensional function even if spin variable is ignored. Therefore, we have to solve the Schrödinger equation approximately. Density functional theory (DFT) is one of the widely used theory for theoretical studies of catalytic chemistry. In DFT, the electronic energy of the system is described as a functional of electron density. The original concept of DFT is not approximate theory but the theory for the exact electronic energy. However, in practical, we have to use DFT approximately because the exact form of the energy functional is still unknown as discussed below.

The basis of DFT is two theorems proved by Hohenberg and Kohn in 1964[20]. The first Hohenberg-Kohn theorem proved that the ground state energy obtained from the Schrödinger equation is a unique functional of the ground state electron density. In brief, several properties of the ground state (e.g. energy) is determined by the ground state electron density. While N-electron wave function is 3N dimensional function (here, spin variable is ignored), electron density is only depended on three spatial variables. Therefore, the ground state energy can be solved as three dimensional functional, and this is one of the big advantage of DFT.

A way for approaching the exact ground state electron density was given by the second Hohenberg-Kohn theorem; the lowest energy is obtained from the energy functional only if the exact ground state electron density is adopted. In other words, the exact ground state electron density can be obtained by minimizing the energy functional, and the obtained lowest energy is the exact ground state energy. From these theorems, we can approach the exact ground state

energy of the system through the ground state electron density. The remaining problem is how to obtain the exact energy functional.

Energy functional E[ρ] can be written as Eq. 1.

$$\begin{aligned} E[\rho] &= F[\rho] + \int \rho(r) V_{Ne} dr \\ &= T[\rho] + J[\rho] + E_{ncl}[\rho] + \int \rho(r) V_{Ne} dr \end{aligned} \quad \cdots(1)$$

Where, V_{Ne} is electron-nuclei attraction potential, T[ρ] is the functional for kinetic energy, J[ρ] is the classical Coulomb interaction between electrons, E_{ncl}[ρ] is the non-classical contribution to the electron-electron interaction (i.e. self-interaction correction, exchange and Coulomb correlation[21]). F[ρ] is called as the Hohenberg-Kohn functional. In the Hohenberg-Kohn functional, only analytical form of J[ρ] is known. In 1965, Kohn and Sham approached to the energy functional through the non-interacting reference system[22]. They focused on describing the kinetic energy part. Because it is known that Slater determinants (Eq. 2) is the exact wave functions of the non-interacting reference system where electrons behave as uncharged fermions moving in the effective potential[21], the exact kinetic energy for this type of wave function can be written as Eq. 3.

$$\theta_s = \frac{1}{\sqrt{N!}} \begin{vmatrix} \varphi_1(x_1) & \varphi_2(x_1) & \cdots & \varphi_N(x_1) \\ \varphi_1(x_2) & \varphi_2(x_2) & \cdots & \varphi_N(x_2) \\ \vdots & \vdots & \cdots & \vdots \\ \varphi_1(x_N) & \varphi_2(x_N) & \cdots & \varphi_N(x_N) \end{vmatrix} \quad \cdots(2)$$

$$T_s = -\frac{1}{2} \sum_i^N \left\langle \varphi_i \left| \nabla^2 \right| \varphi_i \right\rangle \quad \cdots(3)$$

Where, N is number of electrons, {x} are variables of 3N spatial and N spin coordinates, {φ_i} are Kohn-Sham orbitals defined by Eq. 4.

$$f^{KS} \varphi_i = \varepsilon_i \varphi_i \quad \cdots(4)$$

$$f^{KS} = -\frac{1}{2}\nabla^2 + V_s(r) \quad \cdots(5)$$

$\hat{f}^{KS}$ is called as the one-electron Kohn-Sham operator, and V_s is the effective potential. It is important point of the Kohn-Sham approach that the non-interacting reference system is connected to the real system through the same ground state electron density. In brief, the ground state electron density of the non-interacting reference system is equivalent to the exact ground state density of the real system. Therefore, the effective potential V_s is set to fulfill this constraint. From this approach, a part of the kinetic energy functional of Hohenberg-Kohn functional (F[ρ]) is described by the exact kinetic energy of the non-interacting reference system with effective potential. Therefore, F[ρ] can be written as Eq. 6.

$$F[\rho] = T_s[\rho] + J[\rho] + E_{XC}[\rho] \quad \cdots(6)$$

$$E_{XC}[\rho] \equiv \left(T[\rho] - T_s[\rho]\right) + E_{ncl}[\rho] \quad \cdots(7)$$

E_{XC} is called as exchange-correlation energy. In brief, all of the non-classical contributions are included in the exchange-correlation energy functional.

As discussed above, the Kohn-Sham approach gives us way to describe a part of the kinetic energy functional. In addition, we can obtain the exact non-relativistic ground state energy within Born-Oppenheimer approximation through the Kohn-Sham approach if the exact ground state electron density is inserted in the exact energy functional. However, the exact form of the exchange-correlation energy functional is still unknown. Therefore, we have to use approximate exchange-correlation energy functional in practical calculation. Although a lot of approximate E_{XC} were reported (e.g. LDA type, GGA type, hybrid type and so on)[21], we cannot judge which is theoretically the best (or better) approximate functional because the exact form of E_{XC} is

completely unknown. Therefore, we have to compare the result obtained by the approximate functional with experimental results carefully.

1.4.2 Computational Modeling for Catalytic Systems

Based on DFT, we can calculate electronic structures of the catalyst. However, the catalytic system is still complicated even for DFT calculations. Of course, computational cost is a big problem of DFT calculations for the catalytic system. However, how to describe and incorporate the nature of the catalytic system from the complicated system are also important aspects of the theoretical study. From these points of view, efficient modeling of the catalytic system is required. For example, if all factors of the catalytic system are incorporated in the computational model, it is difficult to grasp the essential factor for the catalytic reaction.

By using DFT or other theoretical methods (e.g. post-Hartree-Fock methods, molecular mechanics and so on), atomic-scale modeling of active sites can be done. In this subsection, atomic-scale modeling for the supported metal catalyst was focused on. Cut off the active sites from the catalytic system is one of the straightforward way for the modeling. This simple method is called as cluster model (Figure 3a). In this model, high accurate calculation methods (e.g. hybrid DFT functional, post-Hartree-Fock methods with large basis set, and so on) can be adopted because computational cost can be kept lower. Therefore, several analysis based on molecular orbital interactions can be also adopted. In addition, handling of charged defects or spin multiplicity are relatively easy. However, terminal bonds have to be treated carefully. For example, dangling bonds of terminal oxygens cause strange electronic structure[23]. Therefore, terminal dangling bonds are usually saturated by hydrogen atoms as shown in Figure 3a. In addition, the accuracy of the model is directly affected by selection of the model size.

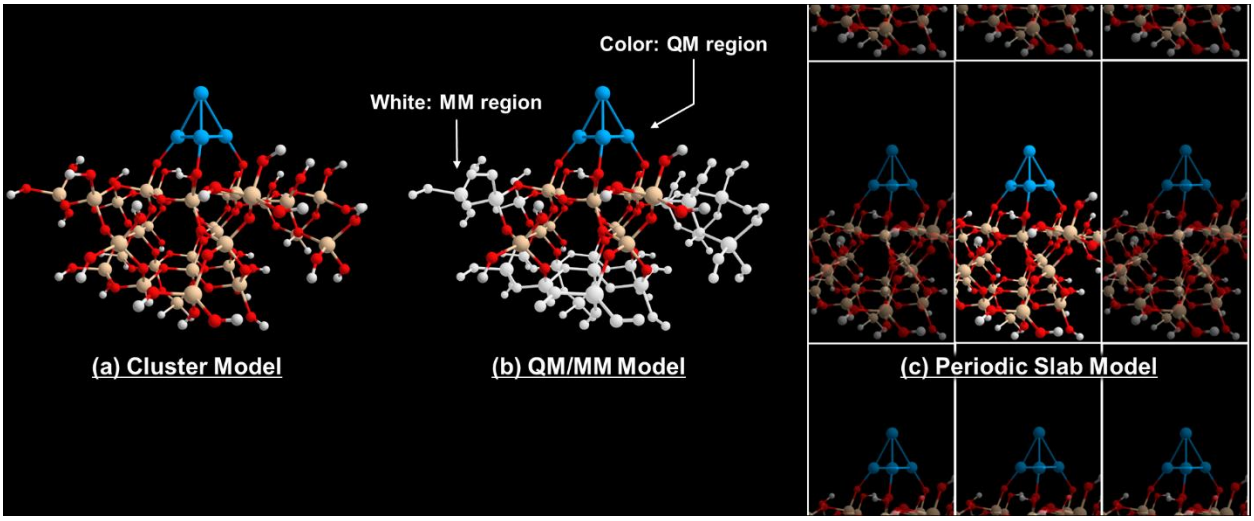

Figure 3. Atomic-scale modelling for the supported metal catalyst. (a) Cluster model, (b) QM/MM model, (c) Periodic slab model.

QM/MM model[24, 25] (or ONIOM model[26, 27]) is another choice of the cluster model (Figure 3b). In this model, important region (e.g. around active site) is calculated by using high accurate theory (e.g. DFT or post-Hartree-Fock methods), and the other region is calculated by low-cost theory (e.g. molecular mechanics or semi-empirical methods). The former region is called as QM region, and the latter region is called as MM region. Therefore, larger model can be calculated without deteriorating the accuracy. While strengths and weaknesses are almost same as those of the cluster model, treatment of boundary region between QM region and MM region is important. Recently, embedded cluster model is reported as theoretical modeling for the heterogeneous catalyst[23, 28]. In this model, QM region is embedded in the point charge (MM region) which represents the bulk effect of the support or metal.

Periodic slab model is one of the widely used model for the heterogeneous catalyst (Figure 3c). In this model, the structure in the unit cell is periodically repeated in three-dimensional direction. By using this model, bulk structure or its effect of the support material or metal surface can be described. In addition, supported metal nanoparticle can be modeled as an infinite rod for one

lateral direction[29, 30]. However, only limited method (e.g. LDA or GGA type DFT functional) can be adopted for this model due to the computational cost. In addition, it is difficult to apply molecular orbital based analysis, and the treatment for the excess charge or spin multiplicity are also difficult due to the periodic boundary condition.

As discussed in above, there is several ways for the atomic-scale modelling of the supported metal catalyst, and each model has both advantages and disadvantages. Therefore, we should use the model in which the true essence of the catalytic system is grasped.

1.5 Overviews of the Thesis

Chapter 1 gives general introduction. The importance of theoretical study for understanding catalytic systems is explained. In particular, the difficulty and importance in understanding the reaction mechanism of catalytic system are discussed, and theoretical methods for he catalysis research are described.

Chapter 2 is entitled as “Elucidation for the Effect of Hydrogen Acceptor Molecule to the Selective Aniline Synthesis by the Supported Pd Catalyst: Theoretical Study”. Role of hydrogen acceptor molecule for the selective aniline synthesis by the Pd cluster catalyst is investigated by DFT calculation. From the point of view of reaction step and atom economy, dehydrogenative aromatization of NH_3 and cyclohexanone is effective approach for the primary aniline synthesis. However, imine generation via condensation of aniline and cyclohexanone, and hydrogeneation of imine also proceed as undesirable reaction. This undesirable reaction is restrained in the presence of styrene, and the selective primary aniline synthesis via dehydrogenative aromatization was achieved on the supported Pd catalyst with styrene. Based on DFT calculations, it was suggested that adsorption of styrene on the Pd surface is stronger than that of imine. In addition, the experimental result of the competitive hydrogenation of styrene and imine

indicated that hydrogenation of imine occurs after the hydrogenation of styrene. From these results, it was suggested that styrene is adsorbed on Pd surface strongly and acts as hydrogen acceptor.

Chapter 3, “DFT Mechanistic Study on the Complete Oxidation of Ethylene by the Silica-Supported Pt Catalyst: C=C Activation via the Ethylene Dioxide Intermediate”, summarizes a study on the mechanism of complete oxidation mechanism of ethylene on the silica supported Pt catalyst based on DFT calculations. Low-temperature complete oxidation of ethylene by mesoporous silica-supported Pt catalyst is a forefront technology for food preservation. Public implementations of the Pt catalyst have already begun, and spectroscopic analyses on the catalytic mechanism have been reported. In this study, density-functional theory calculations were conducted to clarify the potential energy profile and electronic mechanism of the catalytic reaction. Based on the experimental findings, a reaction pathway was proposed for the ethylene oxidation up to CO_2 formation via HCHO intermediate. Among several possibilities, a reaction pathway via ethylene dioxide species is energetically plausible for the C-C bond cleavage to generate HCHO. Particular focus was given to the electronic effect of the silica support in the ethylene dioxide route. The reservoir effect, in which the siloxide groups take electrons from the Pt moiety, reduces the activation energy of the C-C bond cleavage step by taking electrons from the σ(C-C) orbital.

In Chapter 4, “Theoretical Study of C-H Activation by O_2 on Negatively Charged Au Cluster: α, β-dehydrogenation of 1-methyl-4-piperidone by the Au/OMS-2 Catalyst”, C-H bond activation mechanism of piperidone molecule on the Au cluster catalyst is described. Au nanoparticles catalyst supported on manganese oxide octahedral molecular sieve (OMS-2) is a heterogeneous catalyst for α, β-dehydrogenation of β-*N*-substituted saturated ketones. In this

study, reaction mechanism of aerobic C-H bond activation of 1-methyl-4-piperidone on the Au/OMS-2 catalyst was investigated by density functional theory calculations. In particular, the relationship between charge state of Au cluster and catalytic activity was focused on. Au cluster on the OMS-2 support is negatively charged due to the charge transfer from OMS-2 to the Au cluster. In addition, O_2 adsorbed on the negatively charged Au cluster is activated enough to abstract hydrogen atom. Therefore, C-H bond activation by adsorbed O_2 is favorable reaction pathway rather than that directly by Au surface. In addition, activation energy of the C-H bond by adsorbed O_2 becomes smaller with more negatively charged Au cluster because the adsorbed O_2 is activated more significantly.

Chapter 5, entitled as "Theoretical Study for C-H bond Activation on Pd Cluster: Agostic Interaction on Pd Cluster Induced by OAc Ligands", shows C-H bond activation mechanism by the Pd cluster catalyst investigated by DFT calculations. N1-substituted benzotriazole is payed attention as an important compound for cancer treatment. Recently, N1-substituted benzotriazole synthesis via 1,7-palladium migration reaction on the Pd nanoparticle catalyst was reported. In this reaction, Ph-H bond cleavage of the reactant molecule is one of the important step of the reaction. Furthermore, this reaction only proceeds in the presence of OAc ligands. From the results of DFT calculations, it was found that activation energy for Ph-H bond cleavage reaction is decreased more than 10 kcal/mol in the presence of OAc ligand. From the analysis based on the molecular orbital interactions, it was suggested that Ph-H bond is activated by the agostic interaction between Ph-H bond and the Pd cluster in the presence of OAc ligand.

Chapter 6 gives general conclusion of the thesis and summarizes the perspectives on the activation mechanisms of unreactive bonds obtained by the several important cases in the experimental catalysis researchers.

References

1. Haruta, M.; Kobayashi, T.; Sano, H.; Yamada, N., Novel Gold Catalysts for the Oxidation of Carbon Monoxide at a Temperature far Below 0 °C. *Chem. Lett.* **1987,** *16* (2), 405-408.
2. Rothenberg, G., *Catalysis: Concepts and Green Applications*. Wiley-VCH, Weinheim: 2008.
3. Nishikawa, Y.; Ogihara, H.; Yamanaka, I., Liquid-Metal Indium Catalysis for Direct Dehydrogenative Conversion of Methane to Higher Hydrocarbons. *Chemistryselect* **2017,** *2* (16), 4572-4576.
4. Wang, L. S.; Tao, L. X.; Xie, M. S.; Xu, G. F.; Huang, J. S.; Xu, Y. D., Dehydrogenation and Aromatization of Methane under Nonoxidizing Conditions. *Catal. Lett.* **1993,** *21* (1-2), 35-41.
5. Guo, X. G.; Fang, G. Z.; Li, G.; Ma, H.; Fan, H. J.; Yu, L.; Ma, C.; Wu, X.; Deng, D. H.; Wei, M. M.; Tan, D. L.; Si, R.; Zhang, S.; Li, J. Q.; Sun, L. T.; Tang, Z. C.; Pan, X. L.; Bao, X. H., Direct, Nonoxidative Conversion of Methane to Ethylene, Aromatics, and Hydrogen. *Science* **2014,** *344* (6184), 616-619.
6. Ohtsuka, Y.; Nishikawa, Y.; Ogihara, H.; Yamanaka, I.; Ratanasak, M.; Nakayama, A.; Hasegawa, J., Theoretical Study on the C-H Activation of Methane by Liquid Metal Indium: Catalytic Activity of Small Indium Clusters. *J. Phys. Chem. A* **2019,** *123* (41), 8907-8912.
7. Fu, Q.; Wagner, T., Interaction of nanostructured metal overlayers with oxide surfaces. *Surf. Sci. Rep.* **2007,** *62* (11), 431-498.
8. Pacchioni, G., Electronic interactions and charge transfers of metal atoms and clusters on oxide surfaces. *Phys. Chem. Chem. Phys.* **2013,** *15* (6), 1737-1757.
9. Pacchioni, G.; Freund, H. J., Controlling the charge state of supported nanoparticles in catalysis: lessons from model systems. *Chem. Soc. Rev.* **2018,** *47* (22), 8474-8502.
10. Ro, I.; Resasco, J.; Christopher, P., Approaches for Understanding and Controlling Interfacial Effects in Oxide-Supported Metal Catalysts. *ACS Catal.* **2018,** *8* (8), 7368-7387.
11. van Deelen, T. W.; Mejia, C. H.; de Jong, K. P., Control of metal-support interactions in heterogeneous catalysts to enhance activity and selectivity. *Nat. Catal.* **2019,** *2* (11), 955-970.
12. Campbell, C. T., Catalyst-support interactions: Electronic perturbations. *Nat Chem* **2012,** *4* (8), 597-8.
13. Bruix, A.; Rodriguez, J. A.; Ramirez, P. J.; Senanayake, S. D.; Evans, J.; Park, J. B.; Stacchiola, D.; Liu, P.; Hrbek, J.; Illas, F., A New Type of Strong Metal-Support Interaction and the Production of H-2 through the Transformation of Water on Pt/CeO2(111) and Pt/CeOx/TiO2(110) Catalysts. *J. Am. Chem. Soc.* **2012,** *134* (21), 8968-8974.
14. Andersson, M. P.; Abild-Pedersen, F.; Remediakis, I. N.; Bligaard, T.; Jones, G.; Engbwk, J.; Lytken, O.; Horch, S.; Nielsen, J. H.; Sehested, J.; Rostrup-Nielsen, J. R.; Norskov, J. K.; Chorkendorff, I., Structure sensitivity of the methanation reaction: H-2-induced CO dissociation on nickel surfaces. *J. Catal.* **2008,** *255* (1), 6-19.
15. Nørskov, J. K.; Studt, F.; Abild-Pedersen, F.; Bligaard, T., *Fundamental Concepts in Heterogeneous Catalysis*. John Wiley & Sons, Inc: Hoboken, NJ: 2014.
16. van Santen, R. A.; Ghouri, M. M.; Shetty, S.; Hensen, E. M. H., Structure sensitivity of the Fischer-Tropsch reaction; molecular kinetics simulations. *Catal. Sci. Technol.* **2011,** *1* (6), 891-911.

17. Date, M.; Okumura, M.; Tsubota, S.; Haruta, M., Vital role of moisture in the catalytic activity of supported gold nanoparticles. *Angew. Chem. Int. Ed.* **2004,** *43* (16), 2129-2132.
18. Fujitani, T.; Nakamura, I., Mechanism and Active Sites of the Oxidation of CO over Au/TiO2. *Angew. Chem. Int. Ed.* **2011,** *50* (43), 10144-10147.
19. Harding, C.; Habibpour, V.; Kunz, S.; Farnbacher, A. N. S.; Heiz, U.; Yoon, B.; Landman, U., Control and Manipulation of Gold Nanocatalysis: Effects of Metal Oxide Support Thickness and Composition. *J. Am. Chem. Soc.* **2009,** *131* (2), 538-548.
20. Hohenberg, P.; Kohn, W., Inhomogeneous Electron Gas. *Phys. Rev.* **1964,** *136*, B864-B871.
21. Koch, W.; Holthausen, M. C., *A Chemist's Guide to Density Functional Theory*. 2 ed.; Wiley-VCH, Weinheim: 2001.
22. Kohn, W.; Sham, L. J., Self-Consistent Equations Including Exchange and Correlation Effects. *Phys. Rev.* **1965,** *140*, A1133-A1138.
23. Matsui, M.; Sakaki, S., Embedded Cluster Model for Al2O3 and AlPO(4) Surfaces Using Point Charges and Periodic Electrostatic Potential. *J. Phys. Chem. C* **2017,** *121* (37), 20242-20253.
24. Warshel, A.; Karplus, M., Calculation of Ground and Excited-State Potential Surfaces of Conjugated Molecules .1. Formulation and Parametrization. *J. Am. Chem. Soc.* **1972,** *94* (16), 5612-5625.
25. Warshel, A.; Levitt, M., Theoretical studies of enzymic reactions: dielectric, electrostatic and steric stabilization of the carbonium ion in the reaction of lysozyme. *J. Mol. Biol.* **1976,** *103* (2), 227-49.
26. Maseras, F.; Morokuma, K., Imomm - a New Integrated Ab-Initio Plus Molecular Mechanics Geometry Optimization Scheme of Equilibrium Structures and Transition-States. *J. Comput. Chem.* **1995,** *16* (9), 1170-1179.
27. Dapprich, S.; Komaromi, I.; Byun, K. S.; Morokuma, K.; Frisch, M. J., A new ONIOM implementation in Gaussian98. Part I. The calculation of energies, gradients, vibrational frequencies and electric field derivatives. *Theochem-J. Mol. Struct.* **1999,** *461*, 1-21.
28. Berger, D.; Logsdail, A. J.; Oberhofer, H.; Farrow, M. R.; Catlow, C. R. A.; Sherwood, P.; Sokol, A. A.; Blum, V.; Reuter, K., Embedded-cluster calculations in a numeric atomic orbital density-functional theory framework. *J. Chem. Phys.* **2014,** *141* (2).
29. Ishida, T.; Koga, H.; Okumura, M.; Haruta, M., Advances in Gold Catalysis and Understanding the Catalytic Mechanism. *Chem. Rec.* **2016,** *16* (5), 2278-2293.
30. Sabbe, M. K.; Reyniers, M. F.; Reuter, K., First-principles kinetic modeling in heterogeneous catalysis: an industrial perspective on best-practice, gaps and needs. *Catal. Sci. Technol.* **2012,** *2* (10), 2010-2024.

Chapter 2

Elucidation for the Effect of Hydrogen Acceptor Molecule to the Selective Aniline Synthesis on the Supported Pd Catalyst: Theoretical Study

1. Introduction

Primary anilines are important and widely used chemical compounds as intermediates of pharmaceuticals, agrochemicals, dyes, polymers, and electronic materials[1, 2]. One of an effective approach for primary aniline synthesis is dehydrogenative aromatization by Pd catalysts[3-6]. From the point of view of reaction step and atom economy, NH_3 is a proper nitrogen source for chemical synthesis. However, selective synthesis of primary aniline from NH_3 and cyclohexanone via the dehydrogenative aromatization was not achieved until the development of the supported Pd nanoparticle catalyst on hydroxyapatite ($Ca_{10}(PO_4)_6(OH)_2$: HAP) (Pd/HAP catalyst) with hydrogen acceptor (e.g. styrene)[7]. Because the desired primary anilines are typically more reactive than NH_3 for the condensation with cyclohexanone substrates, the corresponding imines are also generated (Scheme 1a: step 2). The imines are reduced by adsorbed hydrogen to undesirable *N*-cyclohexylanilines (Scheme 1a: step 3). Therefore, selective synthesis of primary aniline from NH_3 and cyclohexanone via the dehydrogenative aromatization was difficult in previous catalytic systems[3-6, 8-14]. On the other hand, if a good hydrogen acceptor (e.g. styrene) exists in the catalytic system, the undesirable reductive amination is suppressed by hydrogenation of the hydrogen acceptor (Scheme 1b). Therefore, the Pd/HAP catalyst with hydrogen acceptor is efficient catalytic system for primary aniline synthesis from NH_3 and cyclohexanone via the dehydrogenative aromatization.

Scheme 1. Reaction scheme for primary aniline synthesis from NH_3 and cyclohexanone via the dehydrogenative aromatization by Pd catalyst[7]. (a) Possible reaction route by Pd catalytic system without hydrogen acceptor. (b) Strategy for selective aniline synthesis with hydrogen acceptor.

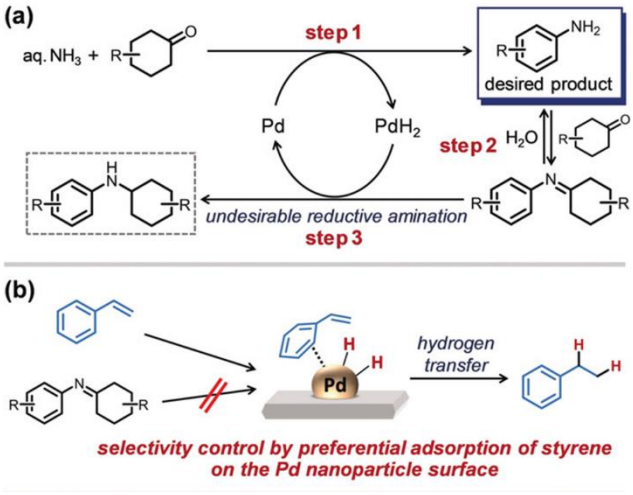

Primary aniline synthesis from NH_3 and cyclohexanone via the dehydrogenative aromatization was achieved by the Pd/HAP catalyst with hydrogen acceptor. The strength of adsorption is important factor for heterogeneously catalyzed hydrogenation because the hydrogenation proceeds according to Langmuir-Hinshelwood mechanism on heterogeneous catalyst[15]. Actually, it was expected that competitive adsorption of styrene and amine occurs in the Pd/HAP catalyst[7]. Therefore, if styrene acts as hydrogen acceptor in the catalytic system, adsorption energy of styrene on the Pd nanoparticle should be larger than that of imine. However, it is not clear whether adsorption energy of styrene on the Pd nanoparticle is larger than that of imine. Although theoretical studies for styrene adsorption on the Pd nanoparticle were reported[16, 17], that for imine was not reported in the best of our knowledge. Therefore, adsorption energies of styrene and imine on the Pd nanoparticle were investigated by density functional theory (DFT) calculations in this study. In particular, we focused on difference of the adsorption energy

between styrene and imine **6a** formed via the condensation of 4-methylcyclohexanone and *p*-toluidine (i.e. R = CH_3 in Scheme 1b).

This chapter is organized as follows. In the next section, computational models and the detail for DFT calculations are discussed. In Subsection 3.1 and 3.2, adsorption structures of styrene and imine **6a** on slab models and cluster models are investigated, respectively. In Subsection 3.3, calculated adsorption energies on each model are analyzed by energy decomposition analysis. A concluding remark is given in Section 4.

2. Computational Details

2.1 Pd_{13} Model

To investigate the adsorption energies of styrene and imine **6a** on the Pd nanoparticle, computational models of the Pd nanoparticle were constructed. First, equilibrium structure of the Pd nanoparticle was constructed by using Wulff construction[18]. Average particle size of the Pd/HAP catalyst (3.7 nm)[7] was adopted for Wulff construction, and surface energies of each Pd facet were taken from previous theoretical study[19]. As shown in Figure 1b, both (111) facet and (100) facet appear as stable surface in equilibrium structure of Pd nanoparticle (white area and green area in Figure 1b, respectively). In addition, edge area and interface between each facet occupy large surface area of Pd nanoparticle. In other words, terrace area of each facet is not so large. These results suggested that a cluster model is suitable better than a periodic model and was adopted as computational model of the Pd nanoparticle. Therefore, Pd_{13} model (Figure 1a) was constructed as computational model of the Pd nanoparticle. This model was pointed out as one of the most stable conformation of the Pd_{13} cluster in a previous theoretical calculation[20]. In addition, this model includes both (111) facet and (100) facet which are stable facets of Pd nanoparticle.

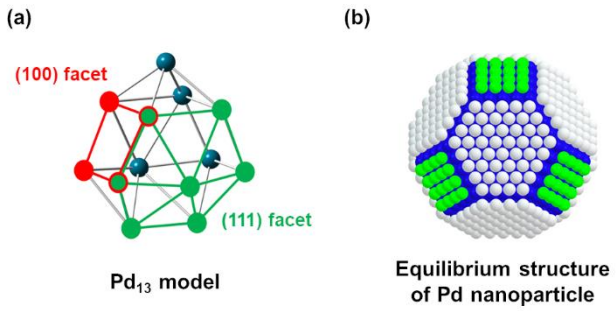

Figure 1. (a) Pd_{13} model, (b) Equilibrium structure of Pd nanoparticle constructed by Wulff construction (white area: (111) facet, green area: (100) facet).

Both geometry optimizations and single-point energy calculations for the Pd_{13} model were performed using DFT at the B3LYP functional level[21, 22] with the D3 version of Grimme's dispersion function[23]. We employed the Stuttgart/Dresden basis set with effective core potential[24] for Pd atoms. The 6-31G(d) basis sets[25] were used for the other atoms. All calculations were carried out using the Gaussian 16 program package[26]. The spin multiplicity of the Pd_{13} model and that with substrates were calculated to be quintet state and septet state, respectively.

2.2 Slab Models

To check validity of the Pd_{13} model (cluster model), surface slab models for (100) facet (Figure 2a: Pd(100) model) and (111) facet (Figure 2b: Pd(111) model) were also constructed by using periodic boundary condition. Both (100) facet and (111) facet were modeled by a (3 × 3) unit cell with 6 layers. The lattice constant of the Pd(111) model and Pd(100) model were set to a = b = 16.7 Å, c = 13.6 Å, $\alpha = \beta = 90°$, $\gamma = 120°$ and a = b = 16.7 Å, c = 11.8 Å, $\alpha = \beta = \gamma = 90°$, respectively. These values were determined by cell-optimization of the bulk structure of Pd. Calculated lattice constant of bulk structure (a = b = c = 3.94 Å) was in good agreement with the

experimental value (a = b = c = 3.96 Å)[27]. Each slab was separated by 25 Å vacuum layer perpendicular to each facet.

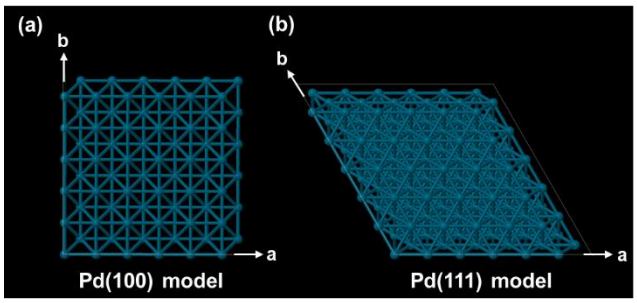

Figure 2. (a) Pd(100) model, (b) Pd(111) model.

These slab models were calculated by DFT calculation with FHI-aims code (version: 171221)[28]. The Perdew−Burke−Ernzerhof (PBE) functional[29] was used as the exchange-correlation functional. The numerical atom-centered orbitals (NAO) basis set[28] with the default "tight" settings were adopted for each atom. In addition, the atomic-scaled zeroth-order regular approximation (Atomic ZORA)[28] was adopted to incorporate the relativistic effects. Furthermore, the van der Waals correction was incorporated based on the Tkatchenko-Scheffler method[30]. A Γ-centered grid of 15 × 15 × 15 k-points were used for the cell-optimization of the bulk Pd structure, and a Γ-centered grid of 5 × 5 × 1 k-points were used for other slab models, respectively. The bottom 4 layers of slab models were fixed to the bulk structure during geometry optimization.

In this study, adsorption energy (E_{ads}) is defined as Eq.1.

$$E_{ads} = E(Ads) - E(Mol) - E(Slab) \quad \ldots (1)$$

Where, E(Ads), E(mol) and E(Slab) are potential energies of adsorption structure, isolated adsorbate molecule and clean slab model, respectively.

3. Results and Discussion

In this section, adsorption energies of styrene and imine **6a** were investigated by using the Pd_{13} model, Pd(100) model and Pd(111) model. As discussed in below, adsorption energies of styrene on both (100) facet and (111) facet were lager than those of imine **6a** in the Pd_{13} model. This tendency is in good agreement with experimental results. On the other hand, adsorption energy of **6a** on the Pd(111) model is larger than that of styrene while adsorption energy of styrene on the Pd(100) model is larger than that of **6a**.

3.1 Adsorption on the Slab Model

First, adsorption structures of styrene and imine **6a** on the Pd(100) model and Pd(111) model were investigated. Theoretical study for imine adsorption on Pd surface was not reported in the best of our knowledge. However, **6a** is adsorbed on Pd surface by nitrogen atom and benzene region, and several theoretical studies for benzene adsorption on Pd surface were reported[31-33]. In addition, styrene is adsorbed on Pd surface by benzene region and vinyl group. Therefore, most stable adsorption structure of benzene on Pd(111) facet and Pd(100) facet reported in previous theoretical studies[31-33] were adopted for initial adsorption structures of benzene region of styrene and **6a** for geometry optimization, respectively. Initial adsorption structure of vinyl group of styrene was also taken from previous theoretical studies for styrene adsorption on Pd(111) surface and Pd(100) surface[16, 17]. While these previous studies were only focused on adsorption structure of vinyl group, adsorption structure of both benzene region and vinyl group of styrene were considered in our present study.

From these initial structures, adsorption structures of styrene and **6a** on the Pd(100) model and Pd(111) model were investigated. As shown in Figure 3a and 3c, adsorption energy of styrene (E_{ads} = -85.2 kcal/mol) is larger than that of **6a** (E_{ads} = -80.6 kcal/mol) on the Pd(100) model. On

the other hand, adsorption energy of styrene (E_{ads} = -73.0 kcal/mol) is smaller than that of **6a** (E_{ads} = -76.6 kcal/mol) on the Pd(111) model as shown in Figure 3b and 3c. These results suggested that styrene adsorption is more favorable than **6a** on Pd(100) facet while adsorption of **6a** is more favorable than styrene on Pd(111) facet. However, experimental result of the competitive hydrogenation of styrene and imine indicated that hydrogenation of imine occurs after hydrogenation of styrene on the Pd/HAP catalyst. This result suggested that styrene is adsorbed on the Pd/HAP catalyst stronger than imine, and adsorption of imine is blocked by such strong adsorption of styrene. Therefore, the tendency of calculated adsorption energies of styrene and **6a** on the Pd(111) model is opposite to the experimental result. In particular, surface area of (111) facet is larger than (100) facet in the equilibrium Pd nanoparticle (*cf.* Figure 1b).

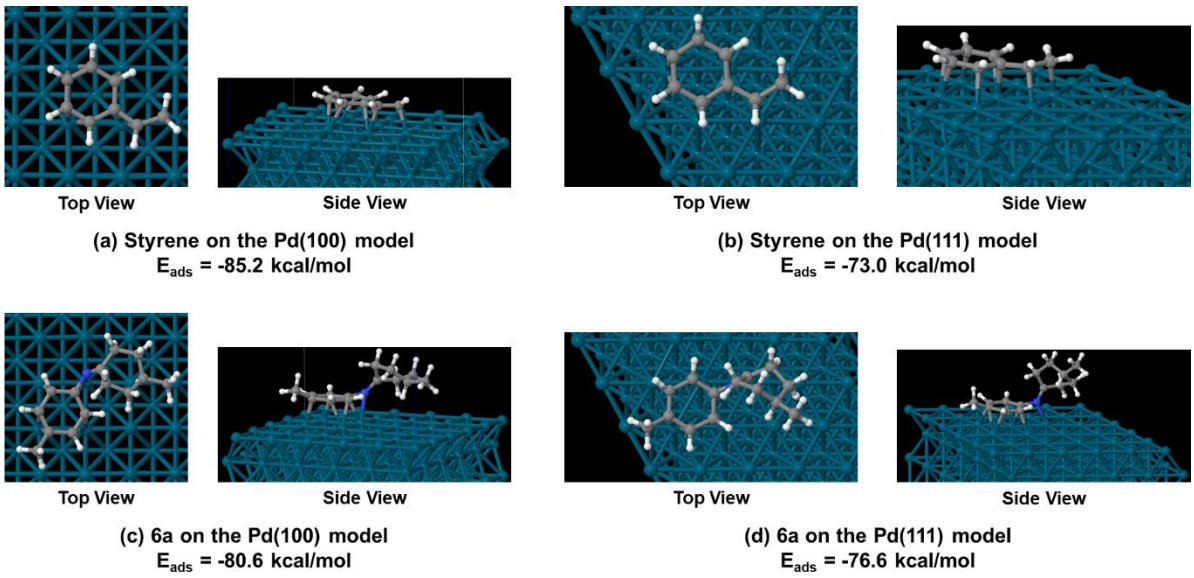

Figure 3. Adsorption structures of styrene and **6a**. (a) Styrene on the Pd(100) model, (b) styrene on the Pd(111) model, (c) **6a** on the Pd(100) model, (d) **6a** on the Pd(111) model.

3.2 Adsorption on the Pd_{13} Model

In this subsection, adsorption structures of styrene and **6a** on (100) facet and (111) facet of the Pd_{13} model (Figure 1a) were investigated. Initial adsorption structures for geometry optimization were determined by same process as discussed in Subsection 3.1. The adsorption energies of styrene on the (111) facet is larger than that of imine **6a** by 3.5 kcal/mol as shown in Figure 4. In addition, the adsorption energy of styrene on (100) facet is also larger than that of imine **6a** by 3.2 kcal/mol (Figure 4). These results suggest that styrene is adsorbed on both facet of Pd nanoparticle more strongly than imine **6a**, which is consistent with the experimental result of the competitive hydrogenation of styrene and imine.

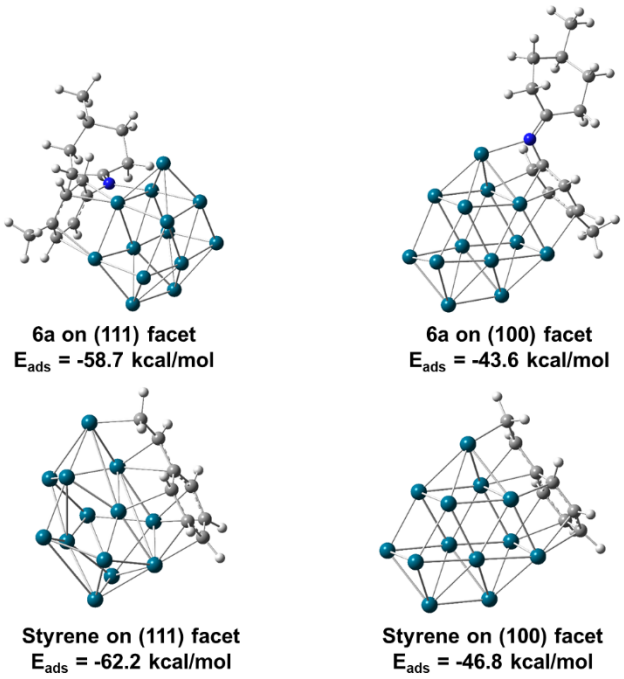

Figure 4. Adsorption structures and adsorption energies (E_{ads}) of styrene and imine **6a** on the Pd_{13} model.

3.3 Energy Decomposition Analysis

To investigate the difference of adsorption tendency between the slab models and cluster model, energy decomposition analysis[34] was performed for each adsorption structure. In this analysis, adsorption energy (E_{ads}) is decomposed into interaction energy (E_{int}) and deformation energy (E_{def}).

$$E_{ads} = E_{int} + E_{def} \quad \dots (2)$$

Deformation energy is also decomposed into two components; deformation energy of Pd model (E_{def_Pd}) and deformation energy of adsorbate molecule (E_{def_Mol}).

$$E_{def} = E_{\mathrm{def\_}Pd} + E_{\mathrm{def\_Mol}} \quad \dots (3)$$

These two components were obtained by potential energy difference between each region in the adsorption structure and the equilibrium structure in isolated system. Interaction energy is defined as remaining component of adsorption energy. One example for energy decomposition analysis was shown in Scheme 2.

Scheme 2. Energy decomposition analysis for the adsorption structure of styrene on (111) face of the Pd13 model[a].

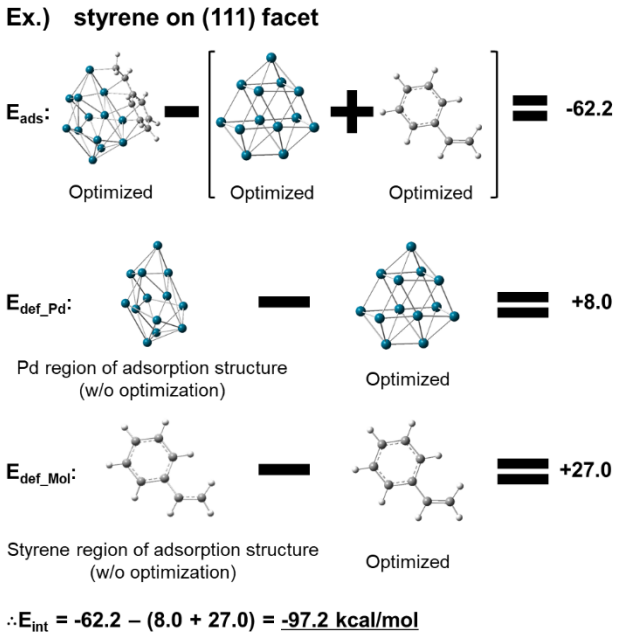

[a]Unit is kcal/mol.

Results of energy decomposition analysis for each adsorption structure were shown in Table 1. First, deformation energy of Pd model (E_{def_Pd}) are lower than 10 kcal/mol in all structures even though geometry change of the Pd_{13} model is large in the adsorption structure of styrene on (111) facet (Figure 4). On the other hand, deformation energy of adsorbate (E_{def_Mol}) are higher than 15 kcal/mol except for **6a** on (111) facet of the Pd_{13} model. In particular, E_{def_Mol} of styrene on the Pd(111) model (E_{def_Mol} = +41.5 kcal/mol) is higher than those of other adsorption structures. Actually, E_{def_Mol} of styrene on (111) facet of the Pd_{13} model (E_{def_Mol} = +27.0 kcal/mol) is lower than that on the Pd(111) model by 14.5 kcal/mol. As a result, interaction energies (E_{int}) of styrene on the Pd(111) model is higher than that of **6a** by 11.7 kcal/mol. In addition, difference of E_{int} of styrene between the Pd(111) model and Pd(100) model is only 0.8 kcal/mol. From these results,

it was suggested that adsorption energy of styrene on the Pd(111) model is decreased by the deformation of styrene due to the less flexibility of the slab model. On the other hand, deformation energy of styrene on (111) facet of the Pd_{13} model is reduced because the Pd_{13} model can change its conformation with low deformation energy. The Pd_{13} model is rather simple computational model for the Pd nanoparticle, and there is a possibility of overestimation of the flexibility or the effect from edge structure between (111) facet and (100) facet. However, these results suggested that rigid and flat slab models could not represent the experimental result, and the flexibility and edge structure are important factors for preferential adsorption of styrene on the Pd nanoparticle.

Table 1. Results of energy decomposition analysis for each adsorption structure.

[kcal/mol]		E_{ads}	E_{def_Pd}	E_{def_Mol}	E_{int}
Slab Model	Styrene on (100)	-85.2	4.2	29.3	-118.7
	Styrene on (111)	-73.0	5.0	41.5	-119.5
	6a on (100)	-80.6	3.3	24.1	-108.0
	6a on (111)	-76.6	5.3	25.9	-107.8
Cluster Model	Styrene on (100)	-46.8	3.9	29.6	-80.3
	Styrene on (111)	-62.2	8.0	27.0	-97.2
	6a on (100)	-43.6	4.7	16.4	-64.7
	6a on (111)	-58.7	0.7	5.8	-65.2

4. Conclusions

The Pd/HAP catalyst with hydrogen acceptor (e.g. styrene) is an efficient catalytic system for the primary aniline synthesis from NH_3 and cyclohexanone via the dehydrogenative aromatization. The undesirable reductive amination of imine formed via the condensation of cyclohexanone and aniline is suppressed by hydrogenation of the hydrogen acceptor. To investigate whether styrene acts as the hydrogen acceptor in the catalytic system, difference of

adsorption energy between styrene and imine on the Pd nanoparticle were investigated by DFT calculations in this study. Adsorption of styrene and imine on the Pd nanoparticle were calculated by using both the cluster model and slab model. In the slab model, adsorption energy of styrene on Pd(100) facet is larger than that of imine by 4.6 kcal/mol. However, adsorption energy of styrene on Pd(111) facet is lower than that of imine by 3.6 kcal/mol. This result is opposite to experimental result of competitive hydrogenation of styrene and imine on the Pd/HAP catalyst[7]; hydrogenation of imine occurs after hydrogenation of styrene on the Pd/HAP catalyst. On the other hand, in the cluster model, adsorption energies of styrene are higher than those of imine both on (100) facet and (111) facet by 3.2 kcal/mol and 3.5 kcal/mol, respectively. Therefore, results of the cluster model are in good agreement with the experimental result. Energy decomposition analysis for each adsorption structure indicated that deformation energy of styrene on the Pd(111) facet in the slab model is larger than that in the cluster model by 14.5 kcal/mol. In addition, interaction energies of styrene on Pd(111) facet is larger than that of imine by 11.7 kcal/mol in the slab model. Furthermore, deformation energy of the Pd_{13} model is lower than 10 kcal/mol even though conformation change of the Pd_{13} model induced by adsorption of molecule is rather large. These results suggested that flexibility and edge structure of the Pd nanoparticle are important factor for the preferential adsorption of styrene. Therefore, the cluster model is suitable model for the Pd nanoparticle rather than the slab model without edge structure, and the result of cluster model suggested that styrene is adsorbed on the Pd nanoparticle stronger than imine.

REFERENCES

1. Vogt, P. F.; Gerulis, J. J., Amines, Aromatic. In *Ullmann's Encyclopedia of Industrial Chemistry*, Wiley-VCH, Weinheim: 2012; Vol. 2, pp 699-718.
2. Amini, B.; Lowenkron, S., Aniline and Its Derivatives. In *Kirk-Othmer Encyclopedia of Chemical Technology*, Wiley, Hoboken: 2003; Vol. 2, pp 783-809.
3. Izawa, Y.; Pun, D.; Stahl, S. S., Palladium-Catalyzed Aerobic Dehydrogenation of Substituted Cyclohexanones to Phenols. *Science* **2011,** *333* (6039), 209-213.
4. Iosub, A. V.; Stahl, S. S., Palladium-Catalyzed Aerobic Dehydrogenation of Cyclic Hydrocarbons for the Synthesis of Substituted Aromatics and Other Unsaturated Products. *ACS Catal.* **2016,** *6* (12), 8201-8213.
5. Girard, S. A.; Huang, H. W.; Zhou, F.; Deng, G. J.; Li, C. J., Catalytic dehydrogenative aromatization: an alternative route to functionalized arenes. *Org. Chem. Front.* **2015,** *2* (3), 279-287.
6. Liu, X. L.; Chen, J.; Ma, T. L., Catalytic dehydrogenative aromatization of cyclohexanones and cyclohexenones. *Organic & Biomolecular Chemistry* **2018,** *16* (45), 8662-8676.
7. Koizumi, Y.; Jin, X. J.; Yatabe, T.; Miyazaki, R.; Hasegawa, J.; Nozaki, K.; Mizuno, N.; Yamaguchi, K., Selective Synthesis of Primary Anilines from NH3 and Cyclohexanones by Utilizing Preferential Adsorption of Styrene on the Pd Nanoparticle Surface. *Angew. Chem. Int. Ed.* **2019,** *58* (32), 10893-10897.
8. Jin, X. J.; Koizumi, Y.; Yamaguchi, K.; Nozaki, K.; Mizuno, N., Selective Synthesis of Primary Anilines from Cyclohexanone Oximes by the Concerted Catalysis of a Mg-Al Layered Double Hydroxide Supported Pd Catalyst. *J. Am. Chem. Soc.* **2017,** *139* (39), 13821-13829.
9. Koizumi, Y.; Taniguchi, K.; Jin, X. J.; Yamaguchi, K.; Nozaki, K.; Mizuno, N., Formal arylation of NH3 to produce diphenylamines over supported Pd catalysts. *Chem. Commun.* **2017,** *53* (78), 10827-10830.
10. Taniguchi, K.; Jin, X. J.; Yamaguchi, K.; Mizuno, N., Supported gold-palladium alloy nanoparticle catalyzed tandem oxidation routes to N-substituted anilines from non-aromatic compounds. *Chem. Commun.* **2015,** *51* (81), 14969-14972.
11. Taniguchi, K.; Jin, X. J.; Yamaguchi, K.; Mizuno, N., Facile access to N-substituted anilines via dehydrogenative aromatization catalysis over supported gold-palladium bimetallic nanoparticles. *Catalysis Science & Technology* **2016,** *6* (11), 3929-3937.
12. Jin, X. J.; Taniguchi, K.; Yamaguchi, K.; Mizuno, N., Au-Pd alloy nanoparticles supported on layered double hydroxide for heterogeneously catalyzed aerobic oxidative dehydrogenation of cyclohexanols and cyclohexanones to phenols. *Chem. Sci.* **2016,** *7* (8), 5371-5383.
13. Taniguchi, K.; Jin, X. J.; Yamaguchi, K.; Nozaki, K.; Mizuno, N., Versatile routes for synthesis of diarylamines through acceptorless dehydrogenative aromatization catalysis over supported gold-palladium bimetallic nanoparticles. *Chem. Sci.* **2017,** *8* (3), 2131-2142.
14. Jin, X. J.; Taniguchi, K.; Yamaguchi, K.; Nozaki, K.; Mizuno, N., A Ni-Mg-Al layered triple hydroxide-supported Pd catalyst for heterogeneous acceptorless dehydrogenative aromatization. *Chem. Commun.* **2017,** *53* (38), 5267-5270.
15. Chorkendorff, I.; Niemantsverdriet, J. W., *Concepts of Modern Catalysis and Kinetics*. Wiley-VCH, Weinheim: 2003; p 23-78.
16. Shamsiev, R. S.; Danilov, F. O.; Flid, V. R.; Shmidt, E. Y., Theoretical modeling of the interaction of phenylacetylene and styrene molecules with Pd{111}. *Russ. Chem. Bull.* **2017,** *66* (12), 2234-2240.

17. Shamsiev, R. S.; Finkelshtein, E. I., Adsorption of phenylacetylene and styrene on palladium surface: a DFT study. *J. Mol. Model.* **2018,** *24* (7), 143.
18. Wulff, G., XXV. Zur Frage der Geschwindigkeit des Wachsthums und der Auflösung der Krystallflächen. *Z. Kristallogr.* **1901,** *34* (1-6), 449-530.
19. Tran, R.; Xu, Z.; Radhakrishnan, B.; Winston, D.; Sun, W.; Persson, K. A.; Ong, S. P., Surface energies of elemental crystals. *Sci Data* **2016,** *3*, 160080.
20. Koster, A. M.; Calaminici, P.; Orgaz, E.; Roy, D. R.; Reveles, J. U.; Khanna, S. N., On the Ground State of Pd-13. *J. Am. Chem. Soc.* **2011,** *133* (31), 12192-12196.
21. Becke, A. D., Density-functional thermochemistry .3. The role of exact exchange. *J. Chem. Phys.* **1993,** *98* (7), 5648-5652.
22. Lee, C. T.; Yang, W. T.; Parr, R. G., Development of the colle-salvetti correlation-energy formula into a functional of the electron-density. *Phys. Rev. B* **1988,** *37* (2), 785-789.
23. Grimme, S.; Antony, J.; Ehrlich, S.; Krieg, H., A consistent and accurate ab initio parametrization of density functional dispersion correction (DFT-D) for the 94 elements H-Pu. *J. Chem. Phys.* **2010,** *132* (15).
24. Andrae, D.; Haussermann, U.; Dolg, M.; Stoll, H.; Preuss, H., Energy-adjusted abinitio pseudopotentials for the 2nd and 3rd row transition-elements. *Theoret. Chim. Acta* **1990,** *77* (2), 123-141.
25. Hehre, W. J.; Ditchfield, R.; Pople, J. A., Self-consistent molecular-orbital methods .12. Further extensions of gaussian-type basis sets for use in molecular-orbital studies of organic-molecules. *J. Chem. Phys.* **1972,** *56* (5), 2257-2261.
26. M. J. Frisch, G. W. T., H. B. Schlegel, G. E. Scuseria, M. A. Robb, J. R. Cheeseman, G. Scalmani, V. Barone, G. A. Petersson, H. Nakatsuji, X. Li, M. Caricato, A. V. Marenich, J. Bloino, B. G. Janesko, R. Gomperts, B. Mennucci, H. P. Hratchian, J. V. Ortiz, A. F. Izmaylov, J. L. Sonnenberg, D. Williams-Young, F. Ding, F. Lipparini, F. Egidi, J. Goings, B. Peng, A. Petrone, T. Henderson, D. Ranasinghe, V. G. Zakrzewski, J. Gao, N. Rega, G. Zheng, W. Liang, M. Hada, M. Ehara, K. Toyota, R. Fukuda, J. Hasegawa, M. Ishida, T. Nakajima, Y. Honda, O. Kitao, H. Nakai, T. Vreven, K. Throssell, J. A. Montgomery, Jr., J. E. Peralta, F. Ogliaro, M. J. Bearpark, J. J. Heyd, E. N. Brothers, K. N. Kudin, V. N. Staroverov, T. A. Keith, R. Kobayashi, J. Normand, K. Raghavachari, A. P. Rendell, J. C. Burant, S. S. Iyengar, J. Tomasi, M. Cossi, J. M. Millam, M. Klene, C. Adamo, R. Cammi, J. W. Ochterski, R. L. Martin, K. Morokuma, O. Farkas, J. B. Foresman, and D. J. Fox, *Gaussian 16, revision A.01* **2016,** *Gaussian, Inc., Wallingford, CT*.
27. Hull, A. W., X-ray crystal analysis of thirteen common metals. *Phys. Rev.* **1921,** *17* (5), 571-588.
28. Blum, V.; Gehrke, R.; Hanke, F.; Havu, P.; Havu, V.; Ren, X. G.; Reuter, K.; Scheffler, M., Ab initio molecular simulations with numeric atom-centered orbitals. *Comput. Phys. Commun.* **2009,** *180* (11), 2175-2196.
29. Perdew, J. P.; Burke, K.; Ernzerhof, M., Generalized gradient approximation made simple. *Phys. Rev. Lett.* **1996,** *77* (18), 3865-3868.
30. Tkatchenko, A.; Scheffler, M., Accurate Molecular Van Der Waals Interactions from Ground-State Electron Density and Free-Atom Reference Data. *Phys. Rev. Lett.* **2009,** *102* (7).
31. Ruiz, V. G.; Liu, W.; Zojer, E.; Scheffler, M.; Tkatchenko, A., Density-Functional Theory with Screened van der Waals Interactions for the Modeling of Hybrid Inorganic-Organic Systems. *Phys. Rev. Lett.* **2012,** *108* (14).

32. Liu, W.; Carrasco, J.; Santra, B.; Michaelides, A.; Scheffler, M.; Tkatchenko, A., Benzene adsorbed on metals: Concerted effect of covalency and van der Waals bonding. *Phys. Rev. B* **2012,** *86* (24).
33. Canduela-Rodriguez, G.; Sabbe, M. K.; Reyniers, M. F.; Joly, J. F.; Marin, G. B., Periodic DFT Study of Benzene Adsorption on Pd(100) and Pd(110) at Medium and Saturation Coverage. *J. Phys. Chem. C* **2014,** *118* (37), 21483-21499.
34. Morokuma, K.; Kitaura, K., Energy Decomposition Analysis of Molecular Interactions. In *Chemical Applications of Atomic and Molecular Electrostatic Potentials*, Politzer, P., Truhlar, D. G., Ed. Springer: Boston, MA: 1981; pp 215-242.

Chapter 3.

DFT Mechanistic Study on the Complete Oxidation of Ethylene by the Silica-Supported Pt Catalyst: C=C Activation via the Ethylene Dioxide Intermediate

1. Introduction

Aging and spoiling of fruits and vegetables are accelerated by a trace amount of the plant hormone ethylene. For transportation and preservation of agricultural products, catalyst development is necessary to decompose ethylene at refrigeration temperatures. Although improvements have been made to lower the working temperature,[1-3] the removal of trace amounts of ethylene at 0 ℃ did not progress until the development of a mesoporous silica-supported Pt catalyst (Pt/MCM-41).[4] This catalyst, as well as recently developed Pt/SBA-15,[5, 6] can completely oxidize 50 ppm of ethylene to CO_2 and H_2O at around 0 ℃. Public implementation is ongoing, and these catalysts have already been installed in commercially available refrigerators.

Besides the successful practical applications, fundamental research interests are also focused on the mechanism of the low-temperature complete oxidation of ethylene. In particular, the reaction mechanism of the C=C bond cleavage of ethylene, which easily occurs on the Pt catalysts, even at low temperatures, is of particular interest. Fukuoka *et al*. investigated the mechanism by using diffuse reflectance infrared Fourier transform (DRIFT) analysis.[4] The results showed that ethylene is oxidized to CO_2 and H_2O via CO on the Pt/MCM-41 catalyst. Additional control experiments suggested that HCHO is an important intermediate state before the CO formation. The proposed mechanism is shown in Scheme 1.[4] To the best of our knowledge from reviews of the literature, there is currently no other useful information on the issue. Although an X-ray analysis of the ethylene oxidation on Pt(111) surface was conducted, neither HCHO nor CO intermediates were observed clearly,[7] which indicates that the reaction on Pt(111) is different from that on mesoporous silica-supported Pt nanoparticles. Theoretical studies have only been conducted for C-C cracking on Pt surface.[8, 9]

Scheme 1. Proposed reaction mechanism of complete C_2H_4 oxidation on the Pt/MCM-41 catalyst.[4]

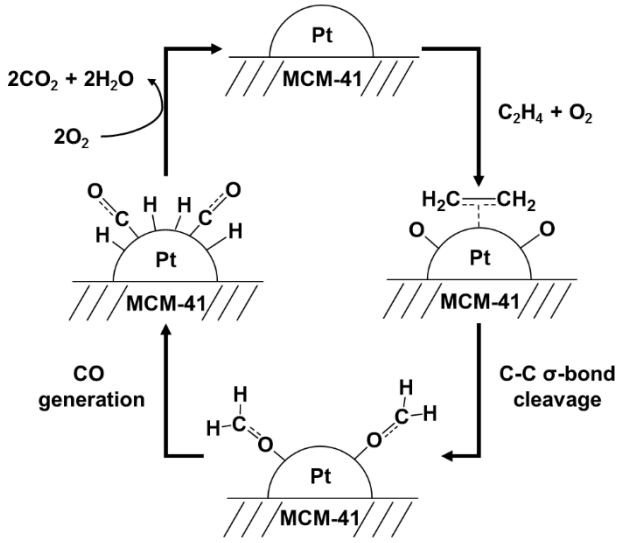

As a next step, a mechanistic investigation with electronic structure calculations should be conducted for clarifying the complete ethylene oxidation mechanism based on the experimental results. Here, we report density functional theory (DFT) calculations on potential energy profiles for the complete oxidation of ethylene. In particular, the electronic structural effect of the metal-support interaction on catalytic reactivity was investigated. The metal-support interaction has been widely studied for many years.[10-12] Even though several studies on supported Pt catalysts have been reported with both experimental[13, 14] and theoretical aspects,[9, 15] the details of the metal-support interaction are not yet fully understood.

The chaper is organized as follows. In the next section, the computational models and details of the DFT calculations are given. In section 3.1, the reaction pathway from ethylene to HCHO is discussed, and the activation energy of each reaction step is compared between the edge and terrace areas of Pt clusters (subsection 3.1.1) and between the computational model with and

without silica support (subsection 3.1.2a–c). The electronic effect from silica support on the C=C bond cleavage reaction is analyzed by using population and molecular orbital analyses (subsection 3.1.2d). Furthermore, the possibility of other reaction pathways (subsection 3.2) is also discussed. In subsection 3.3, the reaction pathway of CO_2 formation from HCHO on the Pt/MCM-41 catalyst is discussed. The H_2O formation pathway was also investigated and is described in subsection 3.4. A concluding remark is given in section 4.

2. Computational Details

2.1 Computational models

To investigate the mechanism of the catalytic role of Pt/MCM-41, several computational models were designed to mimic specific parts of the catalyst and metal-support interactions in their simplest forms. Details on the models are described below.

(a) Pt_7 model (Figure 1a)

This model is for evaluating the activity of the Pt(0) catalyst without silica support. The potential energy profile of the reaction at the edge of the Pt_7 cluster was compared with the reaction at the terrace. In other words, the effect of the coordination number of Pt was analyzed with this model. Seven Pt atoms were placed as the Pt(111) surface. Each Pt-Pt bond length was fixed to that of bulk Pt crystal (2.77Å).[16]

(b) Pt_2 model (Figure 1b)

This model is a minimum model for the low-coordinated part of the Pt(0) cluster and mimics the edge area of the Pt cluster. The positions of Pt atoms are relaxed during structural optimization.

(c) Pt_2-SiO_4 model (Figure 1c)

This model is for analyzing the electronic effect of the silica support. A Pt_2 model is supported on a single silica unit capped by two H atoms, $SiO_2(OH)_2$. The Pt_2 model is directly connected to the oxygen atoms of the silanol groups to mimic a typical mesoporous silica surface with abundant silanol groups.[17] This Pt-silica interaction was also adopted by Lambrecht *et al*. in their theoretical study on the model construction of Pt nanoparticles supported on amorphous silica.[18] Furthermore, EXAFS analysis for the Pt/SiO_2 catalyst suggested that Pt particles are in direct contact with the oxygen atoms of the silica support in the previous experimental study by Mojet *et al*.[19]

(d) Pt_2-Si_{surf} model (Figure 1d)

This model mimics a more realistic silica support effect. A Pt_2 model is supported on a silica surface model which contains 31 units of SiO_2. To make the initial structure of this silica surface model, the bulk crystal structure of α-quartz was sliced as reported in a previous study.[20] The atomic coordinates of the inner 11 units of SiO_2 and two Pt atoms were relaxed in the structural optimization, while the surrounding 20 units of SiO_2 were fixed to the crystal structure. Dangling bonds of 44 oxygen atoms were capped by H atoms. Terminated Si-H bond length and O-H bond length were scaled by pre-defined factors (for Si-H: 0.862226, for O-H: 0.528893) which were used in the ONIOM calculation of Gaussian09. In Figure 1d, the fixed atoms are shown in gray.

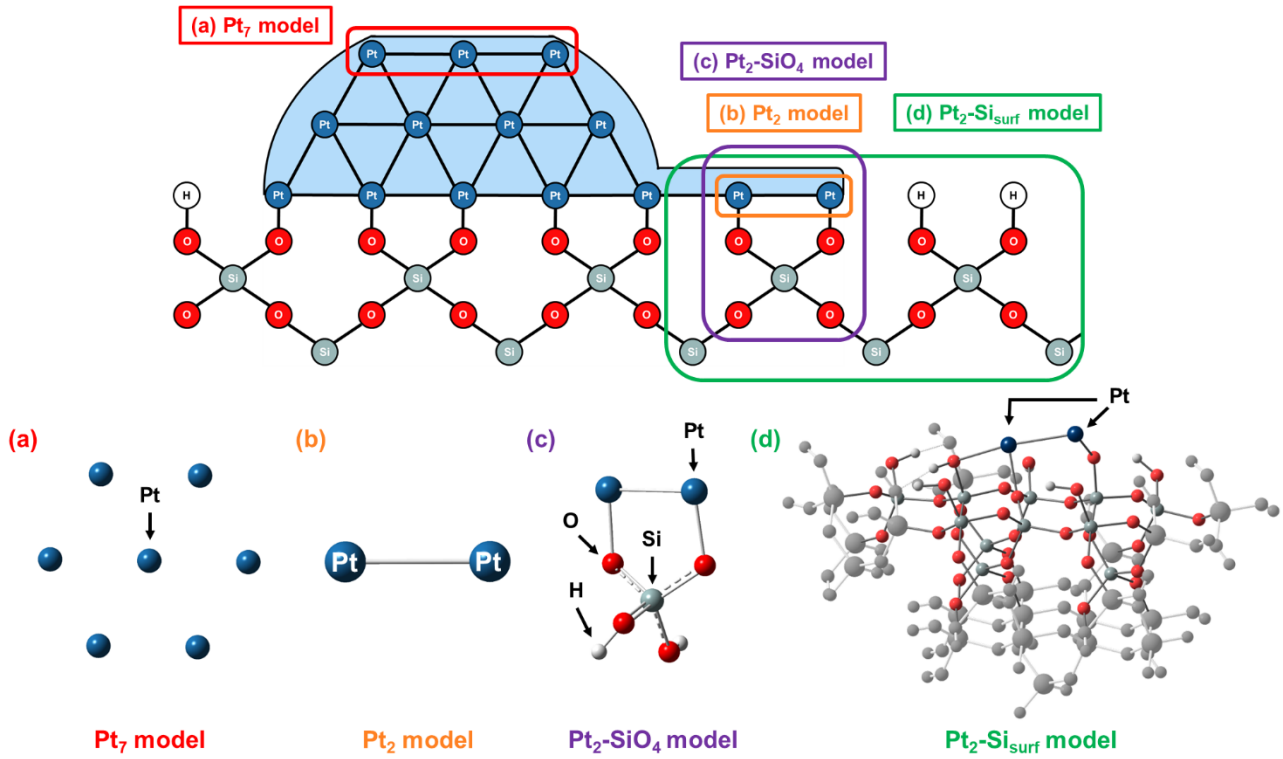

Figure 1. Computational models of the activity of the Pt/MCM-41 catalyst. (a) Pt_7 model, (b) Pt_2 model, (c) Pt_2-SiO_4 model, and (d) Pt_2-Si_{surf} model. The atomic coordinates of the gray-colored atoms are fixed during the structure optimization.

Because this work is a model study to investigate key factors of catalytic activity for the complicated oxidation reaction on supported metal catalyst, we focused on the specific parts of the Pt/MCM-41 catalyst with simple computational models. Therefore, there are possibilities of overestimation of the activity in our computational models while our models are based on both theoretical and experimental results as written in above.

2.2 DFT calculations

Both geometry optimizations and energy calculations were performed using DFT at the B3LYP functional level.[21, 22] We employed the Stuttgart/Dresden effective core potential (ECP60MWB)[23] coupled with (611111/22111/411) basis sets[24] for Pt atoms. The 6-31G(d) basis sets[25] were used for the other atoms. All calculations were carried out using the Gaussian 09 program package.[26] All reactant, product, and transition state structures are connected by intrinsic reaction coordinate calculations. In addition, normal mode analysis was performed, and we confirmed that each of the equilibrium and transition states contained zero and one imaginary frequency, respectively.

3. Results & Discussion

3.1 Reaction pathway of the ethylene-to-formaldehyde conversion

First, we focused on the reaction pathway of the HCHO formation because the IR spectrum of the control experiment implies that HCHO is the intermediate state before ethylene is oxidized to CO.[4] This part of the reaction involves C=C bond cleavage, which would be one of the most difficult steps in the course of the reaction. As described below, our model calculations showed that the silica-support effect is essential for reducing the activation energy for the decomposition of ethylene dioxide into HCHO. Scheme 2 shows the proposed reaction pathway, in which ethylene is sequentially oxidized to the alkoxide and ethylene dioxide intermediates.

Scheme 2. Reaction scheme of the HCHO generation.

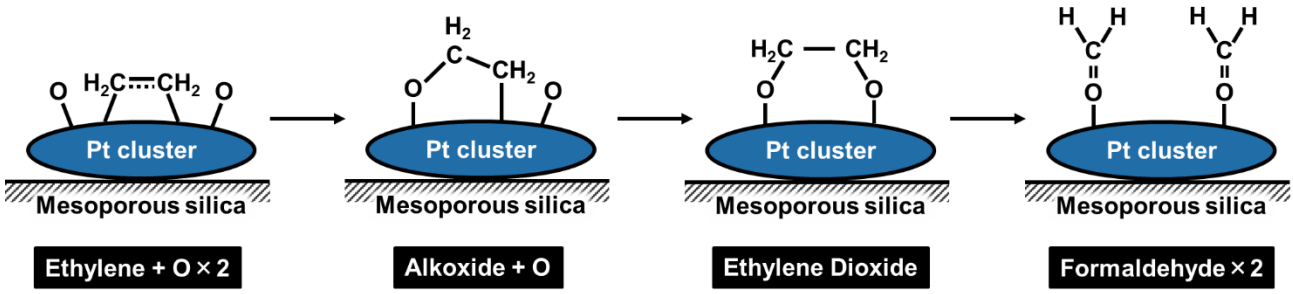

3.1.1 Potential energy profile of the reaction on Pt(0) cluster

The reactivity at the edge area of the Pt(0) cluster was investigated with the Pt_7 model. According to previous experimental studies of Pt(111) surface[27-29], O_2 is dissociatively adsorbed on the Pt cluster. In addition, possibility of dissociative adsorption of oxygen molecule was also investigated on the Pt_7 model. First, adsorption structures of an oxygen molecule on the terrace area and on the edge area were calculated as reactant, respectively (Figure 2: R1S and R2S). These structures were also optimized as triplet state (Figure 2: R1T and R2T). Next, reaction pathways of O=O bond cleavage reaction from those reactant structures were calculated (Figure 2: red line and blue line). From the results in Figure 2, it was suggested that dissociative adsorption of oxygen molecule easily occurs on the terrace area of Pt cluster because of low activation energies (+2.5 kcal/mol (in singlet state) and +8.9 kcal/mol (in triplet state)) and large reaction energies (-58.5 kcal/mol (in singlet state) and -53.7 kcal/mol (in triplet state)). In addition, there are more stable adsorption structures of two oxygen atoms both in singlet state and triplet state (Figure 2: P3S and P3T). Therefore, once O=O bond cleavage occurs, dissociative adsorption structure of oxygen molecule exists on Pt cluster stably even though O=O bond cleavage reaction on the edge area was calculated as endothermically. From these results,

dissociative oxygen molecule (i.e. oxygen atoms) and ethylene molecule are treated as reactant in this study.

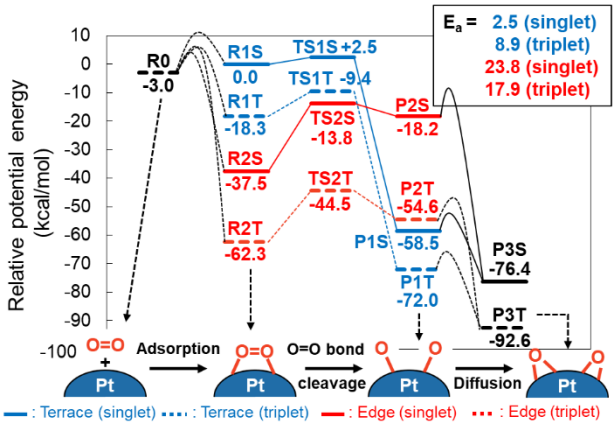

Figure 2. Potential energy diagram of O_2 dissociation on the Pt_7 model. Blue: O_2 dissociation on the terrace area of the Pt_7 model (solid line: singlet state, dashed line: triplet state), red: O_2 dissociation on the edge area of the Pt_7 model (solid line: singlet state, dashed line: triplet state), R0: Sum of potential energy of a Pt_7 model and an O_2.

We started with a reactant state in which an ethylene molecule and two oxygen atoms are adsorbed at the edge of the Pt cluster (A1) as shown in Figure 3a. The calculated potential energy profile is shown in Figure 4 (red line) and the optimized structures are shown in Figure 3a. The co-adsorption of O_2 and ethylene is thermodynamically stable. In the first step, alkoxide intermediate (A2) is formed with an activation energy of 17.2 kcal/mol. The second step is additional C-O bond formation to generate the ethylene dioxide intermediate (A3). This step is the rate-determining step with an activation energy of 49.2 kcal/mol. Before C-C σ-bond cleavage occurs, the adsorption structure of ethylene dioxide is changed from A3 to A4. The activation barrier of this step is 5.3 kcal/mol (Figure 4: E_{aA3}). Formaldehyde formation is completed by the C-C σ-bond cleavage (A5) with an energy barrier of 18.0 kcal/mol.

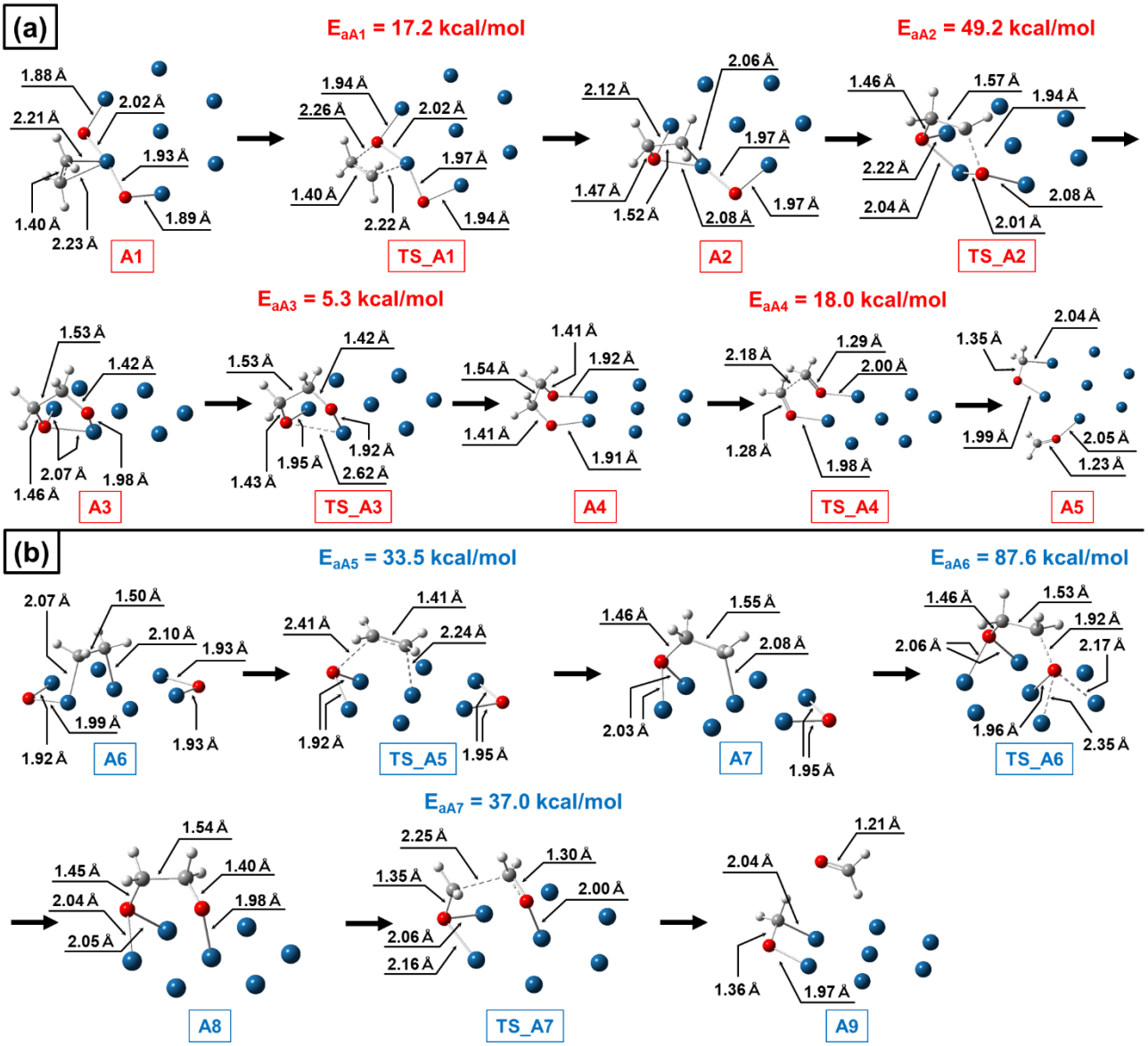

Figure 3. Optimized structures of a reactant, intermediates, transition states and a product of HCHO generation on Pt_7 model. (a) On the edge area, (b) on the terrace area. White ball: hydrogen, gray ball: carbon, red ball: oxygen, blue ball: platinum

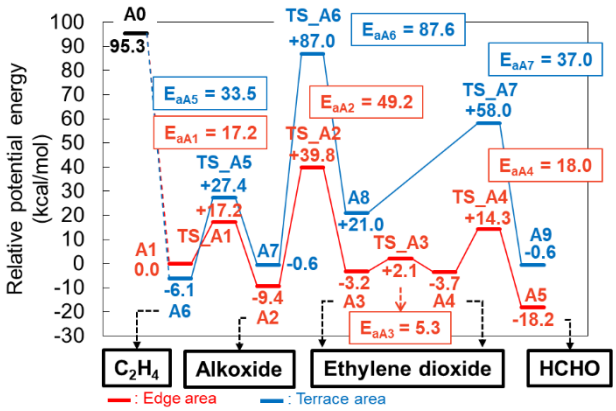

Figure 4. Potential energy diagram of HCHO generation from C_2H_4 on the Pt_7 model. A0: Sum of potential energies of the isolated species, a Pt_7, an O_2, and a C_2H_4.

The same reaction pathway was also found on the terrace area of the Pt_7 model (Figure 4: blue line). The optimized structures are shown in Figure 3b. In the reactant state (A6 state in Figure 3b), an ethylene and two oxygen atoms are adsorbed on the terrace area of the Pt_7 model. As in the edge case, ethylene is adsorbed in the bridge site with a di/ σ bond, which agrees with the results of a previous electron-energy loss spectroscopic study.[30] Ethylene is oxidized to HCHO through the same intermediates, i.e. alkoxide intermediate (A7) and ethylene dioxide intermediate (A8). The rate-determining step is also the ethylene dioxide generation step. The calculated activation energy was 87.6 kcal/mol (Figure 4: E_{aA6}), which is much larger than that at the edge area. From this result, the HCHO formation at low-coordinated Pt atoms at the edge area occurs more easily than on the terrace area.

3.1.2 Effect of silica support

As described previously, our model calculations show that the ethylene oxidation to the HCHO intermediate occurs preferably at less coordinated Pt atoms on the edge area in the Pt_7

cluster. However, the activation energy of the rate-determining step was still too high. A previous study of CO oxidation by a Pt/mesoporous silica catalyst[17] showed that the active site is the Pt-support interface. Therefore, the effect of silica-support was introduced into the computational model. A minimal model, the Pt_2 model, was adopted to check if this model can represent the edge part of the Pt cluster. The $SiO_2(OH)_2$ unit was introduced into the Pt_2 model to investigate the silica support effect on the edge of the Pt cluster.

3.1.2a Potential energy profiles with the Pt2 model

A potential energy profile for the HCHO formation were calculated with the Pt_2 model as shown in Figure 5 (blue line). The optimized structures are shown in Figure 6. Ethylene is oxidized to HCHO through alkoxide intermediate (B2) and ethylene dioxide intermediate (B3) in the same pathway as the reaction at the edge area of the Pt_7 model. The rate-determining step is also the ethylene dioxide generation step with an activation energy of 35.5 kcal/mol (Figure 5: E_{aB2}).

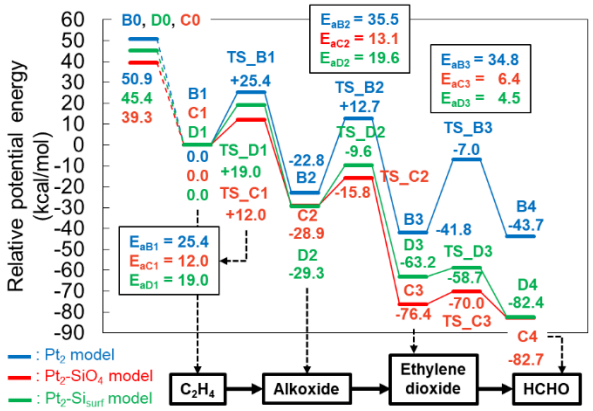

Figure 5. Potential energy diagram of the HCHO formation from C_2H_4. Energies of B0, C0, and D0 states are defined as sum of the energies of the isolated species: Pt_2, O_2, and C_2H_4 for B0; Pt_2-SiO_4, O_2, and C_2H_4 for C0; Pt_2-Si_{surf}, O_2, and C_2H_4 for D0.

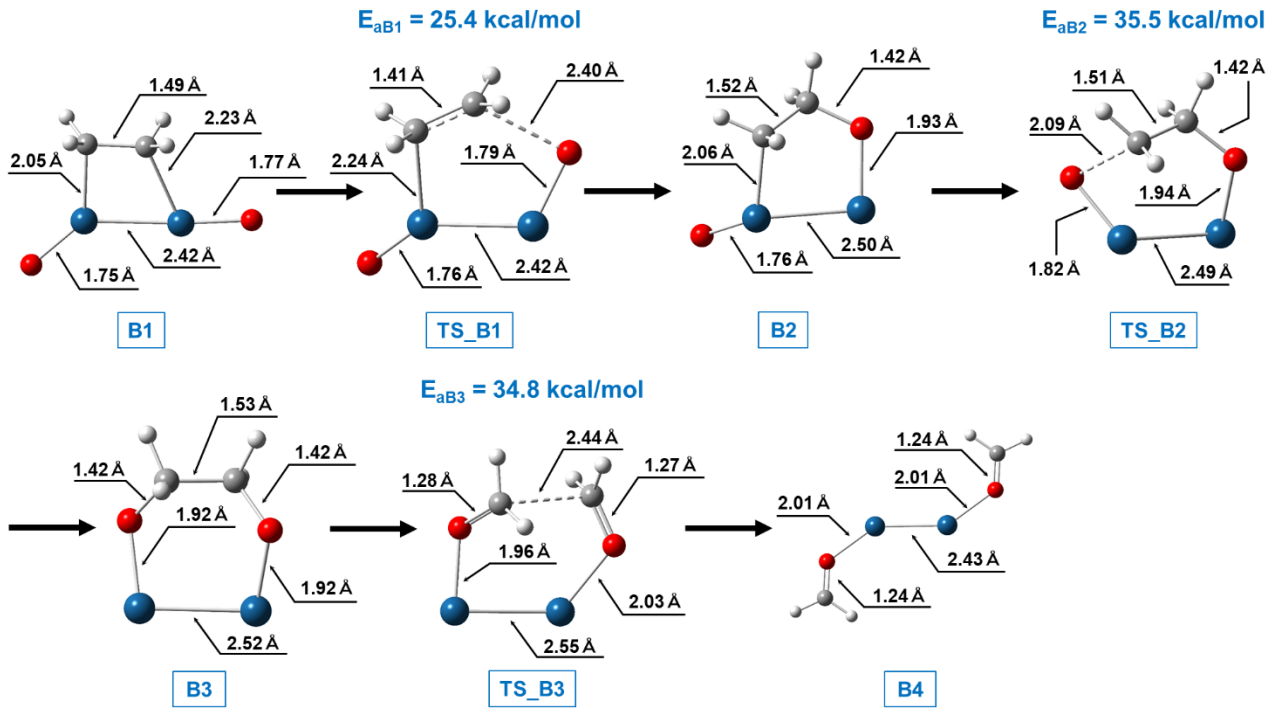

Figure 6. Optimized structures of a reactant, intermediates, transition states and a product of HCHO generation on the Pt_2 model. White ball: hydrogen, gray ball: carbon, red ball: oxygen, blue ball: platinum

3.1.2b Potential energy profile with the Pt_2-SiO_4 model

Next, the reaction pathway was calculated by using the Pt_2-SiO_4 model (Figure 5: red line). The optimized structures are shown in Figure 8. The co-adsorption of two oxygen atoms and ethylene (C1) is energetically stable, which agrees with the previous infrared experiment at 303 K.[17] Therefore, this result supports our simple computational modeling for the interface area between Pt and silica support while formal oxidation state of Pt is calculated as +Ⅲ in C1 structure. Furthermore, this result was also supported by our XAFS analysis. *In situ* XAFS analysis for the Pt catalyst was performed using Pt/SBA-15, which was prepared on SBA-15, one of the common mesoporous silica supports. XAFS measurements at Pt L_{III}-edge were conducted

in transmission mode at BL14B2 of SPring-8 by using Si(311) monochromator. *In situ* XANES spectra and Fourier transformed k^3-weighted EXAFS oscillations of Pt/SBA-15 catalyst before and under reaction are shown in Figure 7. 80 mg of 1wt% Pt/SBA-15 catalyst was placed in a glass tube and pretreated under H_2 flow at 473K for 1 h. After cooling to room temperature under He, the XAFS spectra of the catalyst before the reaction were collected. The catalyst was successively treated with a gas mixture of 500 ppm of C_2H_4, 20 vol% of O_2 and 80 vol% of He with its total flow rate 40 mL/min at room temperature for 10 min, followed by raising the reaction temperature at a rate of 4.5 K/min. Simultaneous analysis of the gas composition using a mass spectrometer revealed that the conversion of C_2H_4 and the formation of CO_2 obviously initiated around at 350-370 K, The XAFS spectra of the catalyst under the reaction were collected at this range of the reaction temperature. As shown in Table 1, Pt-Pt coordination number (*N*) of the Pt/SBA-15 catalyst is obviously smaller than that of Pt foil (10.5) even before the reaction and close to that of a monolayer Pt(111) facet (6.0). This result suggests that thin layered Pt clusters are formed on the SBA-15 support. In addition, the coordination number of Pt-Pt became smaller (6.2 → 4.7), and Pt-O bond was formed under the reaction condition. This result suggests that oxygen atoms are adsorbed on Pt surface because dissociative adsorption of O_2 on the silica supported Pt and spillover of oxygen atoms to the interface between Pt and silica support were detected in the previous experimental study[17]. Furthermore, XANES spectra showed that the Pt under the reaction condition is in higher oxidation state (Figure 7a). These results suggest that thin layered Pt clusters have adsorbed oxygen atoms. The Pt atoms are partially oxidized under the reaction condition. Therefore, these results support our computational modeling for the silica supported Pt catalyst.

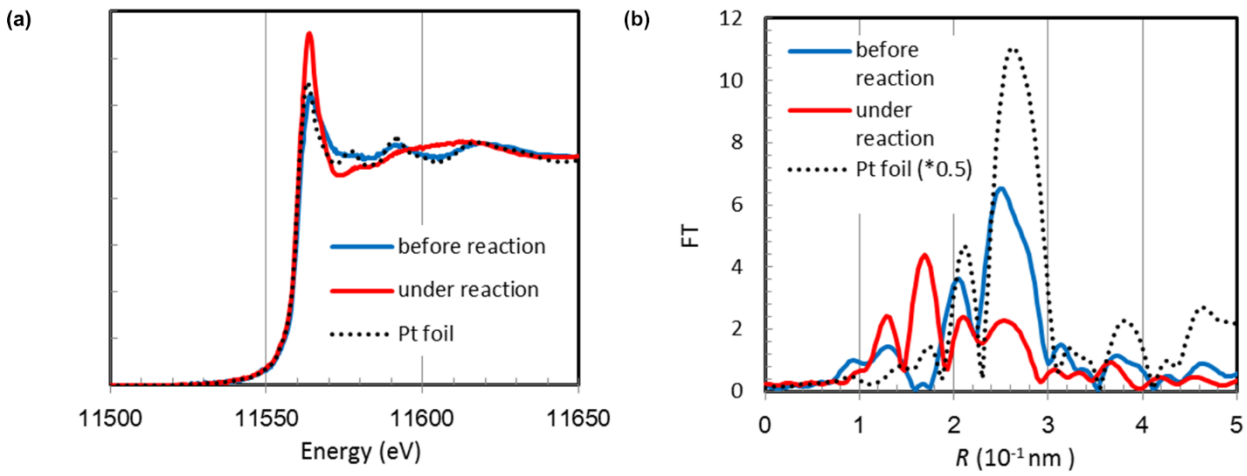

Figure 7. (a) *In situ* XANES spectra and (b) Fourier transformed k^3-weighted EXAFS oscillations of the Pt/SBA-15 catalyst before and under the reaction.

Before reaction: catalyst (1wt% Pt) after H_2 treatment = 0.080 g, under He, SV = 30000 $mLh^{-1}g^{-1}$; under reaction: catalyst (1wt% Pt) after H_2 treatment = 0.080 g, C_2H_4 = 500 ppm, O_2 = 20 vol% He = balance, SV = 30000 $mLh^{-1}g^{-1}$

Table 1. Structural parameters of the Pt/SBA-15 catalyst and Pt foil extracted from the EXAFS fitting.

Samples	Shell	*R* / Å	*N*	σ^2 / Å^2	R factor / %
Pt/SBA-15 before reaction	Pt-Pt	2.719	6.2	0.0083	3.7
Pt/SBA-15 under reaction	Pt-Pt Pt-O (C)	2.676 2.020	4.7 1.0	0.0119 0.0020	3.8
Pt foil	Pt-Pt	2.766	10.5	0.0050	1.6

N: coordination number, *R*: interatomic distance, σ^2: Debye-Waller factor

The adsorption energy of ethylene and O_2 in the Pt_2-SiO_4 model, however, is lower than that in the Pt_2 model by 11.6 kcal/mol. The adsorption structure clearly shows the weak interaction

between ethylene and Pt. The di/σ bond was observed between ethylene and Pt in the Pt_2 model, while molecular adsorption was seen in the Pt_2-SiO_4 model. A weak adsorption with moderate C-Pt interactions is preferable for the subsequent C-O formation (alkoxide formation) because the C-Pt bond has to be dissociated before the C-O bond is made. Consequently, the calculated activation energy of the alkoxide formation step in the Pt_2-SiO_4 model is 12.0 kcal/mol, which is lower than that in the Pt_2 model by 13.4 kcal/mol.

We also found a reaction pathway similar to that with Pt_2 model. Ethylene is also oxidized to HCHO through alkoxide intermediate (C2) and ethylene dioxide intermediate (C3). Although the rate-determining step is also the formation of ethylene dioxide, the calculated activation energy was only 13.1 kcal/mol (Figure 5: E_{aC2}), which is 22.4 kcal/mol lower than that without the silica-support effect (Pt_2 model). In addition, the activation barrier of the C-C σ-bond cleavage was calculated as 6.4 kcal/mol (Figure 5: E_{aC3}), which is 28.4 kcal/mol lower than that of the Pt_2 model.

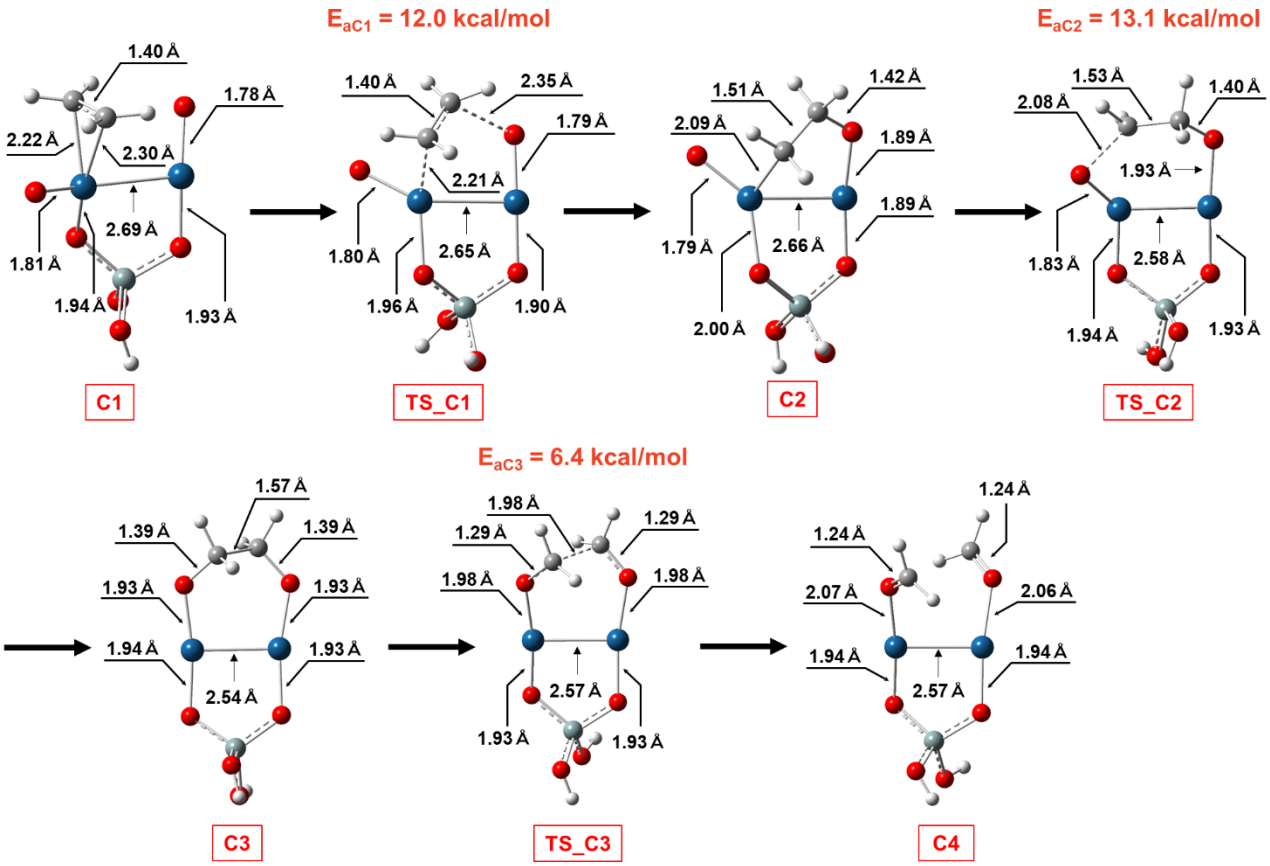

Figure 8. Optimized structures of the reactant, intermediate, transition, and product states of HCHO generation on the Pt_2-SiO_4 model. White: hydrogen, gray: carbon, red: oxygen, blue: platinum, green: silicon.

3.1.2c Potential energy profile with the Pt_2-Si_{surf} model

As shown in Figure 9, a similar reaction pathway was also found in the Pt_2-Si_{surf} model. The calculated potential energy profile is shown in Figure 5 (green line). The rate-determining step is the formation of ethylene dioxide with an activation energy of 19.6 kcal/mol (Figure 5: E_{aD2}), which is close to the result of the Pt_2-SiO_4 model. In addition, the calculated activation barrier of the C-C σ-bond cleavage was only 4.5 kcal/mol (Figure 5: E_{aD3}), which is comparable to that of the Pt_2-SiO_4 model (6.4 kcal/mol) but much lower than that of the Pt_2 model (34.8 kcal/mol).

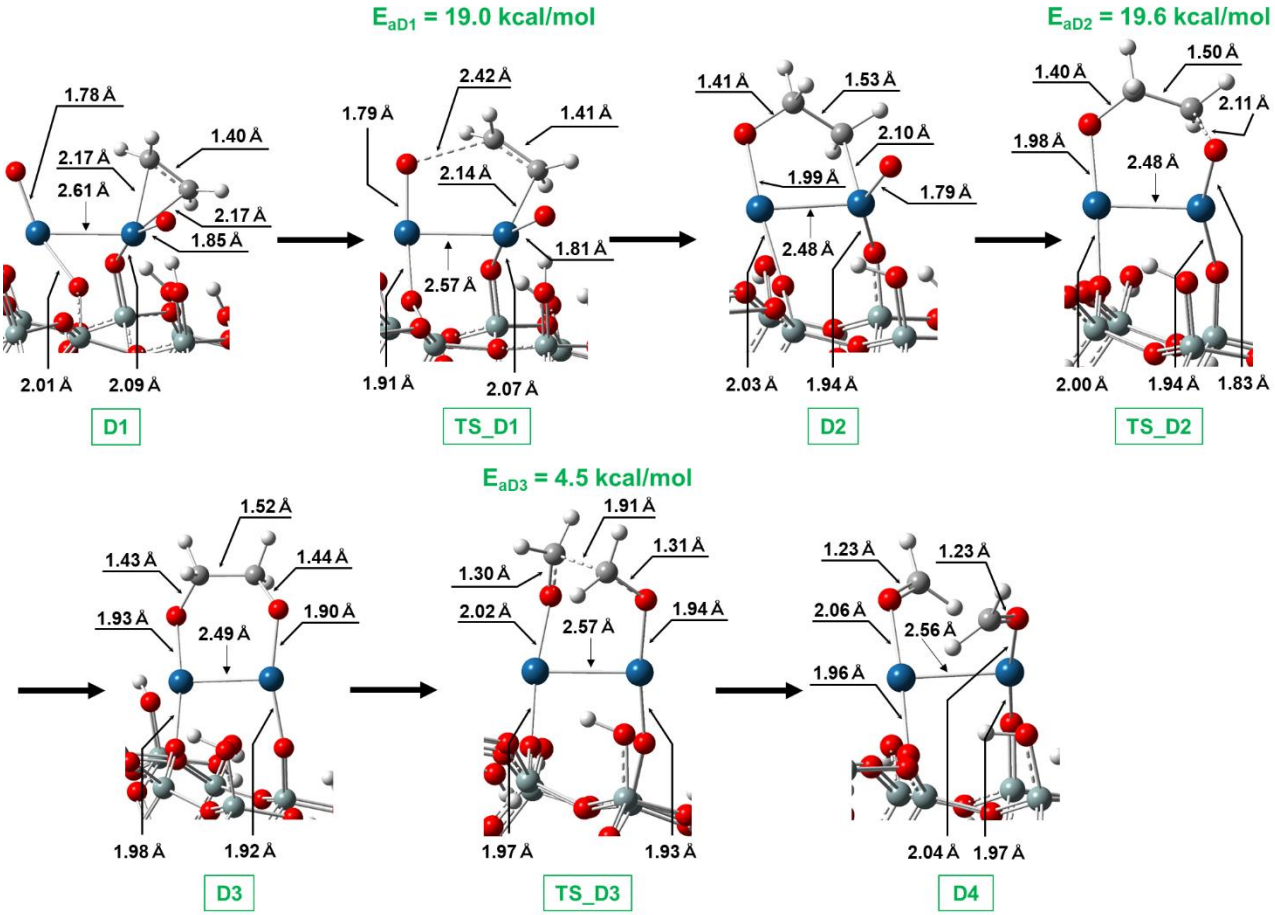

Figure 9. Optimized structures of the reactant, intermediate, transition, and product states of the HCHO generation on the Pt_2-Si_{surf} model. White: hydrogen, gray: carbon, red: oxygen, blue: platinum, green: silicon.

3.1.2d Analysis of the silica support effect

To understand why the activation barriers decrease by the Pt-support interaction introduced in the Pt_2-SiO_4 model, an energy decomposition analysis[31] was performed for each state. The support effect, ΔE^{sup}, was defined as the potential energy change from the Pt_2 model to the Pt_2-SiO_4 model. The B0 and C0 states, which are composed of isolated ethylene, O_2, and catalyst,

are taken as the reference point, and their energy was shifted to 0.0 kcal/mol. The potential energies of other states in the Pt_2 and Pt_2-SiO_4 models were also shifted relative to the B0 and C0 states, respectively. For example, the energies of the B1 and C1 states were shifted to -50.9 and -39.3 kcal/mol, respectively. The ΔE^{sup} was decomposed into structural deformation, $\Delta E^{\mathrm{struct}}$, and electronic, ΔE^{elec}, effects. The structural deformation effect represents the energy change due to the structural deformation induced by the support. To evaluate the structural effect, we defined a Pt_2-rmSiO_4 model in which the atomic coordinates of the Pt_2 model were simply changed into those of the Pt_2-SiO_4 model. A single-point energy, E(Pt_2-rmSiO_4), was calculated with the Pt_2-rmSiO_4 model, and the structural deformation contribution was evaluated as $\Delta E^{\mathrm{struct}}$ = E(Pt_2-rmSiO_4) - E(Pt_2). The electronic contribution was defined as the remaining contributions, $\Delta E^{\mathrm{elec}} = \Delta E^{\mathrm{sup}} - \Delta E^{\mathrm{struct}}$. The results are shown in Table 2.

Table 2. Energy decomposition analysis of the silica support effect in the Pt_2-SiO_4 model. Units are in kcal/mol.

Components[a]	Reactant, intermediate, and transition states in Pt_2-SiO_4 model						
	C1	TS_C1	C2	TS_C2	C3	TS_C3	C4
ΔE^{sup}	11.6	-1.8	5.5	-16.9	-23.0	-51.4	-27.4
ΔE^{elec}	-25.7	-27.7	-10.7	-24.5	-29.0	-57.6	-69.3
$\Delta E^{\mathrm{struct}}$	37.3	25.9	16.2	7.6	6.0	6.2	41.9

[a] ΔE^{sup} was calculated as E(Pt_2-SiO_4)-E(Pt_2). E(Pt_2-SiO_4) and E(Pt_2) are the relative potential energy as described in the main text. Structural deformation effect, $\Delta E^{\mathrm{struct}}$, denotes E(Pt_2-rmSiO_4)-E(Pt_2). Electronic effect, ΔE^{elec}, was calculated as $\Delta E^{\mathrm{sup}} - \Delta E^{\mathrm{struct}}$.

This energy decomposition analysis was also performed with the Pt_2-Si_{surf} model. As shown in Table 3, qualitative tendencies of each component (ΔE^{sup}, ΔE^{elec}, $\Delta E^{\mathrm{struct}}$) are almost same with those of the Pt_2-SiO_4 model. These results suggested that there is no big difference between the

Pt_2-SiO_4 model and that on the Pt_2-Si_{surf} model in the mechanism of formaldehyde generation from ethylene.

Table 3. Energy decomposition analysis of the silica support effect in the Pt_2-Si_{surf} model. Units are in kcal/mol.

Components[a]	Reactant, intermediate, and transition states in Pt_2-Si_{surf} model						
	D1	TS_D1	D2	TS_D2	D3	TS_D3	D4
ΔE^{sup}	5.5	-0.9	-1.0	-16.9	-15.9	-46.2	-33.2
ΔE^{elec}	-31.2	-19.8	-11.9	-20.6	-17.2	-51.0	-71.1
ΔE^{struct}	36.7	18.9	10.9	3.8	1.3	4.8	37.9

[a] ΔE^{sup} was calculated as E(Pt_2-Si_{surf})-E(Pt_2). E(Pt_2-Si_{surf}) and E(Pt_2) are the relative potential energy as described in the main text. Structural deformation effect, ΔE^{struct}, denotes E(Pt_2-rmSi_{surf})-E(Pt_2). Electronic effect, ΔE^{elec}, was calculated as $\Delta E^{sup} - \Delta E^{struct}$.

Alkoxide intermediate (C2) generation step. Due to the support effect, the energy of the C1 state became unstable by 11.6 kcal/mol, while that of the TS_C1 state slightly changed by -1.8 kcal/mol. The decomposition analysis showed that the structural deformation effect in the C1 state (37.3 kcal/mol) is greater than that in the TS_C1 state by 11.4 kcal/mol. This is because the structures of the C1 and B1 states are clearly different as shown in Figure 8 and Figure 6, respectively. In the B1 state of the Pt_2 model, ethylene is adsorbed in the bridge site with two σ(Pt-C) bonds (di/σ bond) as observed in the Pt(111) surface at room temperature.[30] The C-C bond length (1.49 Å) indicates that the π-bond is already broken and that ethylene interacts as an alkyl group. In the C1 state of the Pt_2-SiO_4 model, ethylene is adsorbed at the on-top site. This change in the binding site could be ascribed to the instability of the electronic state of Pt. If the two σ(Pt-C) bonds, which were observed in the Pt_2 model, were kept in the Pt_2-SiO_4

model, the formal oxidation state of each Pt atom would become IV. Each Pt atom has 14-electrons, which is relatively unstable due to the electron deficiency.

Ethylene dioxide (C3) generation step. As shown in Table 2, the energy of the C2 state became unstable by 5.5 kcal/mol, while that of the TS_C2 state was stabilized by 16.9 kcal/mol. The silica support reduced the activation energy of this step by 22.4 kcal/mol. The electronic effect of the silica support in the C2 state is lower than that in the TS_C2 state by 13.8 kcal/mol. The structural deformation effect in the C2 state is larger than that in the TS_C2 state by 8.6 kcal/mol.

The electronic effect, which reduced the activation energy of the ethylene dioxide formation, could be ascribed to the instability of the 14-electron Pt(IV) atom (the left one in C2 of Figure 8) in the alkoxide intermediate. The electronic effect of the silica-support also weakens the Pt($5d_{xy}$)-C(2p) σ-bond, which is represented in the energy levels of molecular orbitals (MOs) with σ(Pt-C) bonding character as shown in Figure 10. The energy levels of HOMO-10 in the Pt_2-rmSiO_4 and HOMO-1 in the Pt_2-SiO_4 models were -10.1 and -7.1 eV, respectively. In the Pt_2-SiO_4 model, the σ-bond in the Pt-C moiety has anti-bonding interaction with the oxygen 2p-orbital of the silica support (see Figure 10), which increased the orbital energy level.

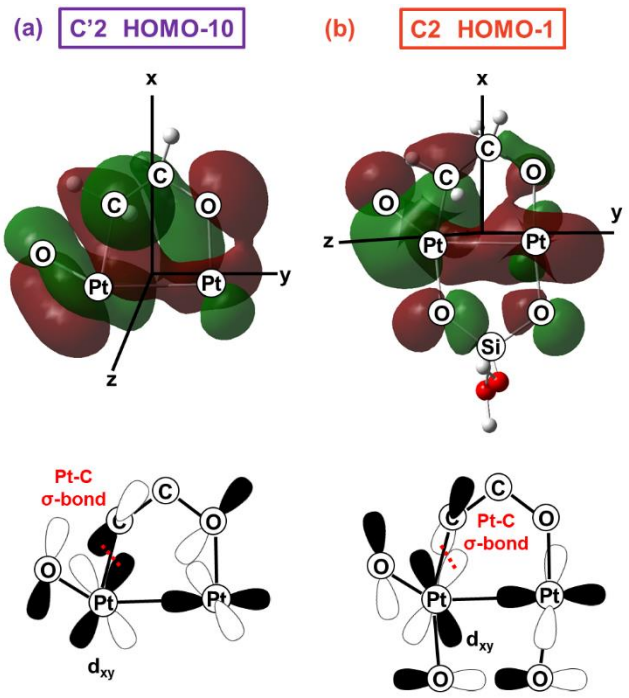

Figure 10. (a) HOMO-10 of the Pt_2-rmSiO_4 model at the C'2 structure and (b) HOMO-1 of the Pt_2-SiO_4 model at the C2 structure

The structural deformation effect also contributes to the total support effect. Comparing the structures in the Pt_2 model (Figure 6) with those in the Pt_2-SiO_4 (Figure 8) model, the structural deformation in the C2 state is relatively larger than that of the TS_C2 and C3 states.

C-C σ-bond cleavage step. The silica effect, which is introduced in the Pt_2-SiO_4 model, reduced the potential energy of the TS_C3 state by 51.4 kcal/mol and that of the C3 state by 23.0 kcal/mol as shown in Table 2. The activation energy of the σ(C-C) bond cleavage in the Pt_2-SiO_4 model became only 6.4 kcal/mol, which is reduced by 28.4 kcal/mol from that in the Pt_2 model (see Figure 5). The reason clearly lies in the electronic effect. The TS_C3 state is stabilized by 57.6 kcal/mol, although the C3 state is only stabilized by 29.0 kcal/mol.

The electronic stabilization by the silica support effect can be understood as follows. In Table 4, the electron population of Pt 5d orbitals in the Pt_2-SiO_4 model (the C3 state) is compared with that in the Pt_2 model (the B3 state), where natural bond orbital analysis was employed. The population of the $5d_{xz}$ orbital in the C3 state (1.59 and 1.51 for the Pt^1 and Pt^2 atoms, respectively) is smaller than that in the B3 state (1.99 for both Pt^1 and Pt^2 atoms) by 0.40 and 0.48, respectively. This result indicates that an electron from the Pt $5d_{xz}$ orbital is taken by the silica support.

Table 4. Electron population of the Pt 5d orbitals in the B3 (Pt_2 model) and C3 (Pt_2-SiO_4 model) states. For the definitions of Pt^1 and Pt^2, see Figure 11.

	B3 (w/o silica support)		C3 (w/ silica support)	
	Pt^1	Pt^2	Pt^1	Pt^2
d_{xy}	1.95	1.95	1.89	1.98
d_{xz}	1.99	1.99	1.59	1.51
d_{yz}	1.85	1.85	1.97	1.99
d_{x2y2}	1.16	1.16	1.19	1.14
d_{z2}	1.90	1.90	1.89	1.89

The decrease in the d_{xz} population can be interpreted by the Pt-silica orbital interaction. Two important σ(C-C) orbitals in the TS_C3 state of the Pt_2-SiO_4 model are shown in Figure 11. The Pt d_{xz} orbitals in the LUMO and HOMO-1 make a δ-anti-bonding (δ*) interaction between the two Pt atoms. In addition, the Pt-Pt δ*-bond interacts with both the ethylene dioxide (C-C σ-bond) and silica support (O2p orbitals). Based on this observation, an orbital correlation diagram was drawn and is shown in Figure 12. In the Pt_2 model without the silica support, the d_{xz} orbitals (and therefore the Pt-Pt δ*-bonds) are fully occupied. As a result, the σ(C-C) bond becomes

strong due to the electron occupation. In contrast, the support effect decreases the occupation of the Pt-Pt δ*-bond, and the MO in Figure 11a becomes unoccupied (LUMO). As a result, the transition state is stabilized because the electron occupation at the high-energy Pt-O(silica) anti-bonding orbital can be avoided. At the same time, the σ(C-C) bond is weakened because of the lessened occupation of the σ(C-C) moiety. In this way, the transition state of the C-C σ-bond cleavage is stabilized by orbital interaction through the Pt-Pt δ-bond in the silica support model.

The present results are reminiscent of the reservoir concept proposed in 1988 by Hoffmann,[32] who stated that a two-orbital four-electron interaction can be bonding due to the hole reservoir effect of the surface. In our system, the reservoir effect stabilized the Pt-O(ethylene dioxide) moiety and weakened the C-C σ-bond at the same time. In other theoretical studies, Lambrecht and Johnson *et al.* reported that Pt atoms in the interface between Pt nanoparticles and the silica support have positive charges.[15, 18, 33] Mikhailov *et al.* reported in their theoretical study that the activation barrier of the C-C bond cleavage in an alkane cracking reaction decreased via the cationic Pt atoms in a Pt/zeolite catalyst.[9] Our present results are consistent with these previous results.

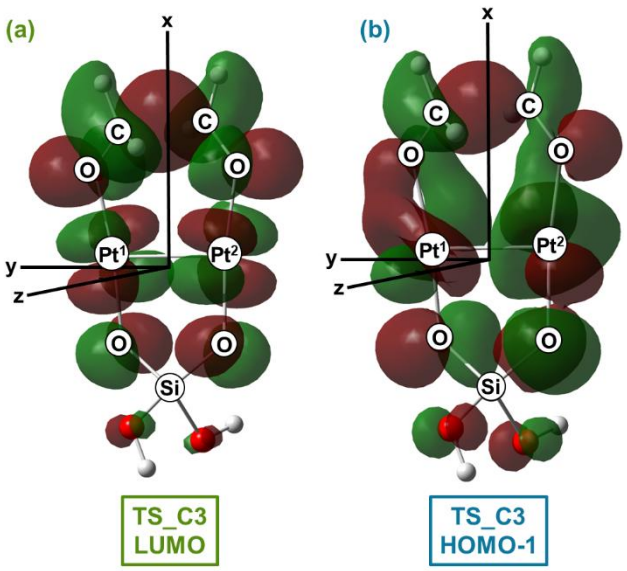

Figure 11. (a) LUMO and (b) HOMO-1 of the TS_C3 state of the Pt_2-SiO_4 model.

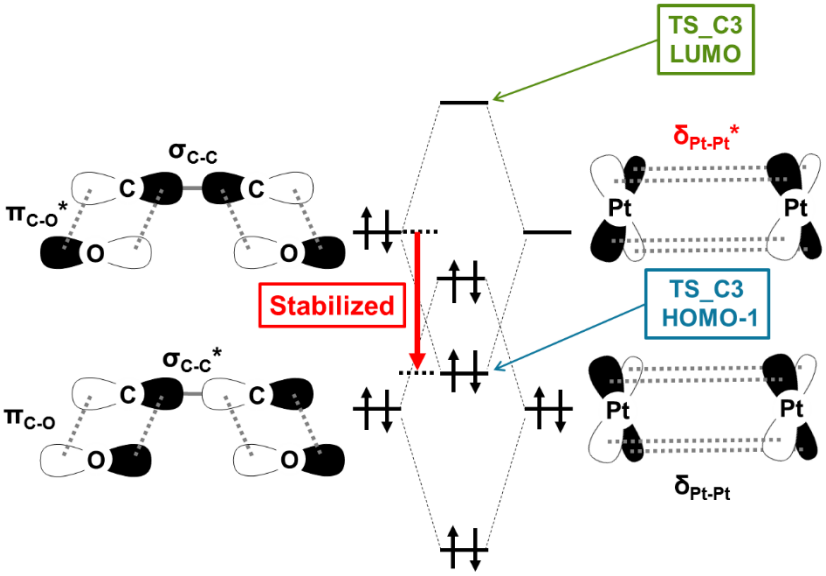

Figure 12. Orbital interactions between ethylene dioxide and Pt-Pt δ- and δ*-bonds.

Table 2 also shows that the structural deformation effect in the C4 state is significantly large (+41.9 kcal/mol). The reason is clearly indicated in Figures S1 and 5. The structures of the B3 and TS_B3 states are similar to those of the C3 and TS_C3 states, respectively, while that of the

B4 state is rather different from that of the C4 state. Two HCHO molecules in the B4 state repel each other, while those in the C4 state maintain their structure in the transition state. As explained above, the Pt-O(dioxide) anti-bonding orbital is not occupied due to the reservoir effect of the silica support, which stabilizes the Pt-O bond and keeps the two HCHO in a meta-stable position.

3.2 Possibility of other reaction pathways

3.2.1 Reaction pathways through epoxide intermediate

The possibility of a reaction pathway through an epoxide intermediate was also investigated with the Pt_2-SiO_4 model. The epoxide species can be formed via both Eley-Rideal (ER) and Langmuir-Hinshelwood (LH) pathways. In the ER mechanism, ethylene directly attacks adsorbed oxygen atoms. In the LH pathway, the alkoxide intermediate could isomerize to epoxide.

As explained below, a reaction pathway through the epoxide intermediate is unfavorable in comparison with the pathway through alkoxide and ethylene dioxide intermediates. The results of the investigation are shown in Figure 13. In the ER mechanism, the energy of the epoxide intermediate (C19) is lower than that of the alkoxide species (C2) by 7.5 kcal/mol. However, the calculated activation energy of epoxide generation via the ER mechanism (22.6 kcal/mol) is higher than that of the alkoxide intermediate formation from ethylene (12.0 kcal/mol) by 10.6 kcal/mol. In the LH mechanism, the energy of the epoxide intermediate (C20) is close to that in the ER mechanism. However, the activation energy of the isomerization to epoxide (30 kcal/mol) is higher than that of the ethylene dioxide formation from the alkoxide intermediate by 16.9 kcal/mol. Therefore, both ER and LH pathways for the epoxide formation are unfavorable

because the activation barriers in these pathways are much greater than those through alkoxide and ethylene dioxide intermediates.

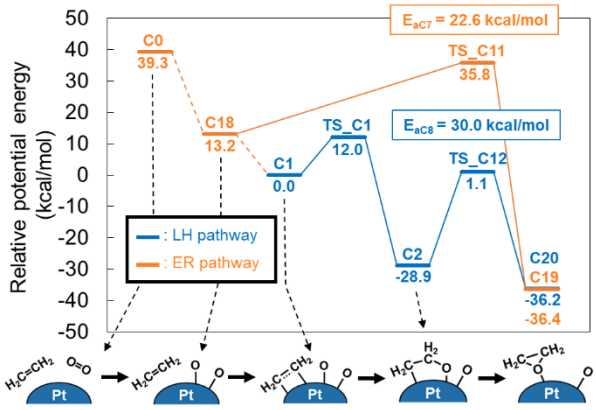

Figure 13. Potential energy profile for epoxide formation pathways on the Pt_2-SiO_4 model. Orange line: ER pathway, blue line: LH pathway

3.2.2 A reaction pathway via isomers of alkoxide and dioxide

A C-C σ-bond cleavage pathway directly from the alkoxide intermediate (C2 in Figure 8) was also investigated using the Pt_2-SiO_4 model (see Scheme 2). The present calculation showed that the C-C σ-bond cleavage to form HCHO and CH_2 species is endothermic by 8.7 kcal/mol. The calculated activation barrier was 25.1 kcal/mol, which is larger than that of the ethylene dioxide formation by 12.0 kcal/mol. In addition, the barrier is also larger than that of the C-C σ-bond cleavage from ethylene dioxide intermediate by 18.7 kcal/mol. Therefore, the C-C σ-bond cleavage directly from the alkoxide intermediate is energetically unfavorable and thus can be safely ruled out.

To investigate other reaction pathways from ethylene dioxide to reach HCHO, relative stability of structural isomers of the ethylene dioxide intermediate was investigated. The isomers we selected have a -O-C-C-O- skeleton common to ethylene dioxide. Valence of C, H and O

atoms were kept to 4, 1, and 2, respectively. Resultant four isomers were considered, and their potential energy relative to ethylene dioxide is shown in Figure 14a.

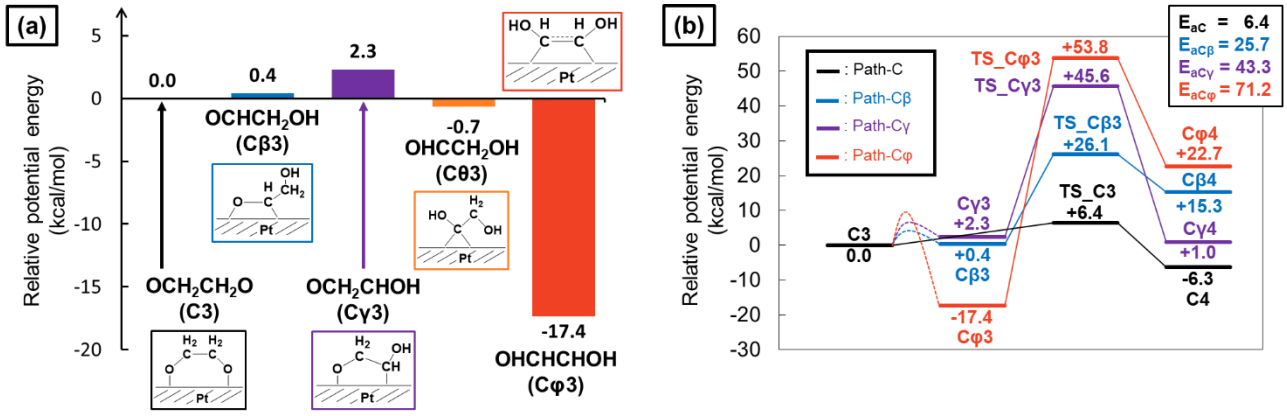

Figure 14. (a) Potential energy of the structural isomers of the ethylene dioxide relative to ethylene dioxide intermediate (C3). The Pt_2-SiO_4 model was used for the computational model. (b) Potential energy diagram of the C-C σ-bond cleavage from the isomers. Black: reaction from C3 (Path-C), blue: reaction from Cβ3 (Path-Cβ), purple: reaction from Cγ3 (Path-Cγ), red: reaction from Cφ3 (Path-Cφ).

The relative energy of the isomers, Cβ3, Cγ3, and Cθ3 are +0.4, +2.3, and -0.7 kcal/mol, respectively, which are close to that of C3. In contrast, the Cφ3 isomer with OHCHCHOH (Cφ3) structure is more stable than C3 by 17.4 kcal/mol. However, activation energy of C-C σ-bond cleavage from Cφ3 was 71.2 kcal/mol, which is by 64.8 kcal/mol larger than that from C3 as shown in Figure 14b. The next stable isomer is Cθ3. However, transition state for the C-C dissociation from Cθ3 (Path-Cθ) could not be found, probably due to the instability of the product. From the other two isomers, Cβ3 and Cγ3, transition state for the C-C dissociation was obtained. However, calculated activation energy of the Paths-Cβ and Cγ is 25.7 and 43.3 kcal/mol, respectively, which are larger than that of Path-C by 19.3 and 36.9 kcal/mol, respectively.

Among the reaction pathway investigated here, Path-C is the most favorable in terms of both activation energy and reaction energy. Path-C ends up with the formation of two HCHO which is adsorbed on the Pt_2-SiO_4 model stably (*cf.* Figure 5: C0 and C4). This is one of the possible reason why only Path-C proceeded exothermically. These results suggested that ethylene dioxide is a reasonable intermediate of the C-C σ-bond cleavage to produce HCHO on the Pt catalyst.

3.3 Reaction pathway of the HCHO-to-CO_2 conversion on a Pt cluster

In this subsection, we discuss the reaction pathway of CO_2 formation from HCHO, which is the latter half of the complete oxidation pathway of ethylene (see Scheme 1). Potential energy profiles were calculated with the Pt_7, Pt_2, and Pt_2-SiO_4 models.

First, reaction pathway of CO_2 generation from formaldehyde was calculated on the edge area of the Pt_7 model (Figure 17: blue line). On the edge area of the Pt_7 model, C-H bonds cleavages from a formaldehyde occur stepwise (Figure 15: A11, A12) and then CO is generated (Figure 15: A13). The activation barrier of CO generation from formaldehyde is calculated as +19.3 kcal/mol (Figure 17: E_{aA6}). Reaction pathway of CO_2 generation from the intermediate structure which contains a generated CO and an oxygen atom (Figure 15: A14) was also investigated. The activation barrier of CO_2 generation from CO is calculated as +33.1 kcal/mol (Figure 17: E_{aA7}). From these results, the complete oxidation pathway of ethylene on the edge area of the Pt_7 model was investigated. The rate-determining step of whole reaction cycle is ethylene dioxide generation reaction (Figure 4: E_{aA2}) and the activation barrier is +49.2 kcal/mol.

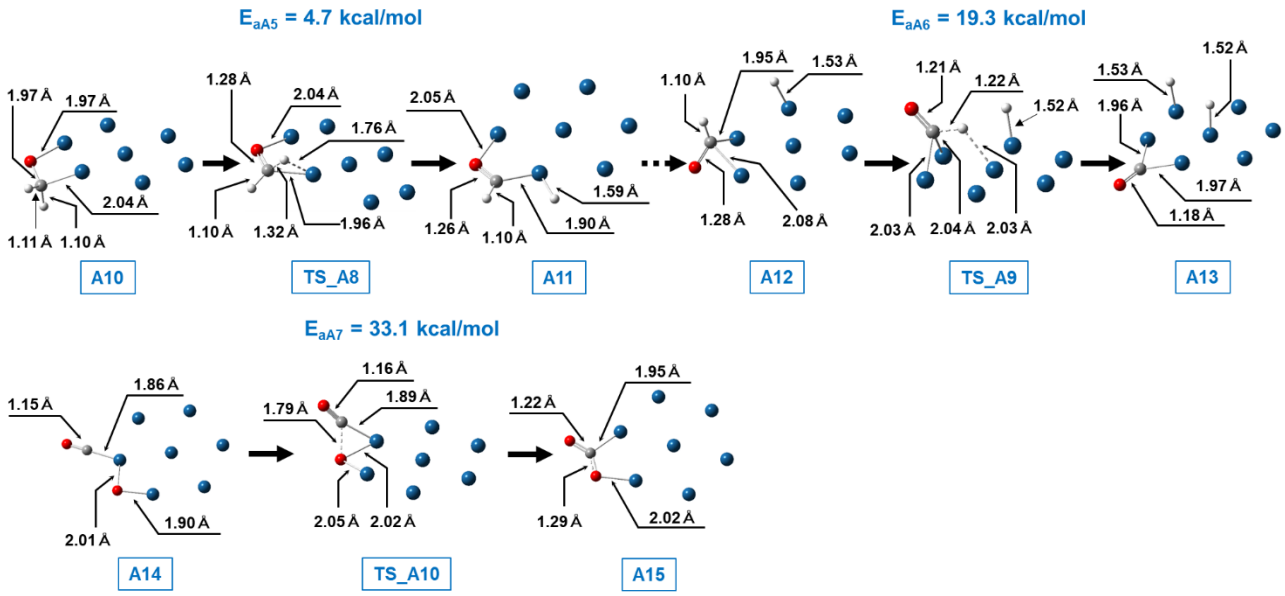

Figure 15. Optimized structures of a reactant, intermediates, transition states and a product of CO_2 generation from HCHO on the edge area of the Pt_7 model. White ball: hydrogen, gray ball: carbon, red ball: oxygen, blue ball: platinum

Note that relative potential energy between structures which contain different number of elements (i.e. between A13 and A14 of Figure 17 and Figure 15) was calculated by Eq. 1 to match the number of contained elements.

$$\Delta\mathrm{E(A14)} = \left[E(A14) - E(A10) + \left\{E\left(2H_{Pt_7}\right) - E(Pt_7)\right\} - \left\{E\left(O_{Pt_7}\right) - E(Pt_7)\right\}\right] \times 627.5 \quad \ldots (1)$$

Where, $\Delta E(A14)$ is relative potential energy of A14 compared with A10 [kcal/mol]. $E(A14)$ and $E(A10)$ are potential energies of A14 and A10, respectively [a.u.]. $E(2H_{Pt7})$ is potential energy of adsorption structure of two hydrogen atoms on the Pt_7 model [a.u.]. $E(O_{Pt7})$ is also potential energy of adsorption structure of an oxygen atom on the Pt_7 model [a.u.]. $E(Pt_7)$ is potential energy of the Pt_7 model [a.u.]. Eq. 1 was also applied for TS_A10 and A15 to match number of contained elements with A10.

Next, reaction pathway of CO_2 generation from formaldehyde was calculated on the Pt_2 model (Figure 17: green line). On the Pt_2 model, CO_2 generation pathway from formaldehyde is almost same as that on the Pt_7 model and Pt_2-SiO_4 model (Figure 16). Activation energies of CO generation from formaldehyde and CO_2 generation from CO on the Pt_2 model were calculated as +26.5 kcal/mol (Figure 17: E_{aB4}) and +28.0 kcal/mol (Figure 17: E_{aB6}), respectively. Therefore, the complete oxidation pathway of ethylene on the Pt_2 model was also investigated. The rate-determining step of whole reaction cycle is ethylene dioxide generation reaction (Figure 5: E_{aB2}) and the activation barrier is +35.5 kcal/mol.

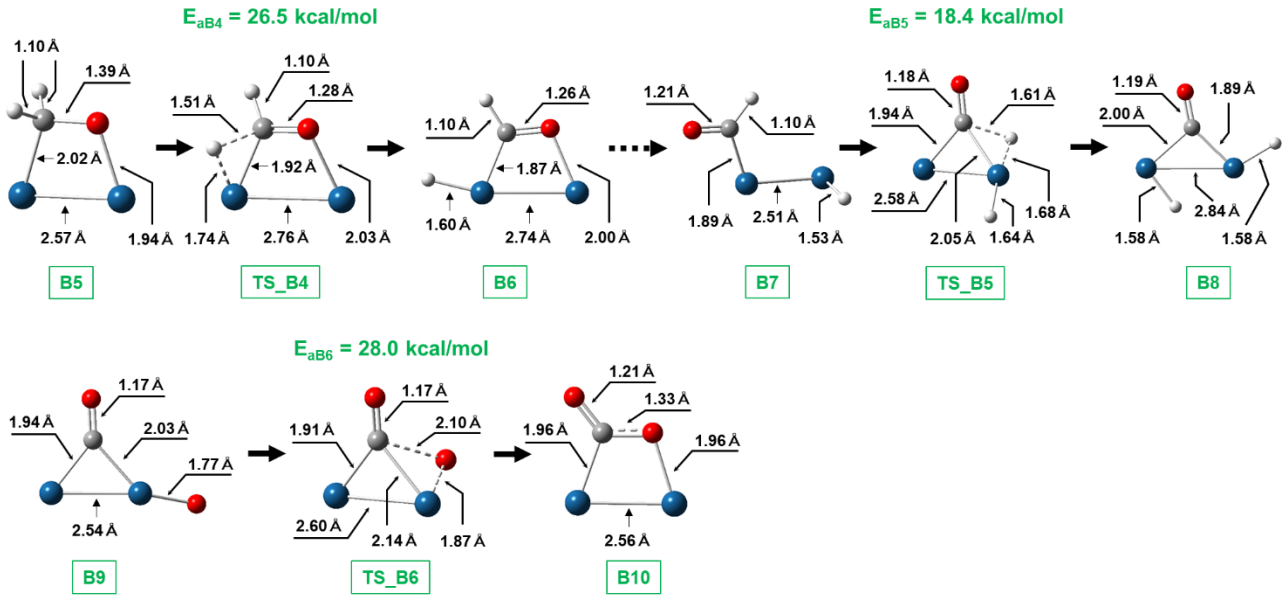

Figure 16. Optimized structures of a reactant, intermediates, transition states and a product of CO_2 generation from HCHO on the Pt_2 model. White ball: hydrogen, gray ball: carbon, red ball: oxygen, blue ball: platinum

Note that relative potential energy between structures which contain different number of elements (i.e. between B8 and B9 of Figure 17 and Figure 16) was calculated by Eq. 2 to match the number of contained elements.

$$\Delta E(B9) = \left[E(B9) - E(B5) + \left\{E\left(2H_{Pt_2}\right) - E(Pt_2)\right\} - \left\{E\left(O_{Pt_2}\right) - E(Pt_2)\right\}\right] \times 627.5 \quad \ldots (2)$$

Where, $\Delta E(B9)$ is relative potential energy of B9 compared with B5 [kcal/mol]. $E(B9)$ and $E(B5)$ are potential energies of B9 and B5, respectively [a.u.]. $E(2H_{Pt2})$ is potential energy of adsorption structure of two hydrogen atoms on the Pt_2 model [a.u.]. $E(O_{Pt2})$ is also potential energy of adsorption structure of an oxygen atom on the Pt_2 model [a.u.]. $E(Pt_2)$ is potential energy of the Pt_2 model [a.u.]. Eq. 2 was also applied for TS_B6 and B10 to match number of contained elements with B5.

Finally, the calculated potential energy profile with the Pt_2-SiO_4 model is shown in Figure 17 (red line). The C-H bonds of HCHO dissociate in a stepwise manner (see structures of TS_C4 and TS_C5 in Figure 18) to produce CO. The activation energies of the first and second C-H bond cleavages are 1.7 (E_{aC4}) and 19.4 (E_{aC5}) kcal/mol, respectively. A transition state TS_C5 is connected to an intermediate state C8 where two hydrogen atoms are dissociatively adsorbed on the same Pt atom. Since H_2 formation is energetically unstable by 5.8 kcal/mol, these hydrogen atoms would stay on the Pt cluster in a dissociated state. As described below, the remaining H atoms would be removed by H_2O formation. The CO molecule is finally oxidized to CO_2 via TS_C6 with an activation barrier of 21.5 kcal/mol (Figure 17: E_{aC6}), which is the rate-determining step of the whole reaction cycle. In the experimental DRIFT measurement, a strong band at 2048 cm^{-1} appeared immediately and was assigned to CO.[4] Our results agree with the experimental finding and support the proposed reaction mechanism via the formation of the HCHO intermediate state.

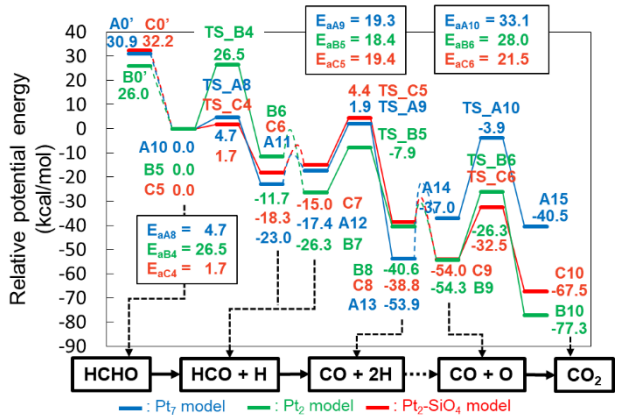

Figure 17. Potential energy diagram of CO_2 generation from HCHO. Potential energies of the A0', B0', and C0' states are defined as sums of the potential energies of the isolated catalyst and an HCHO.

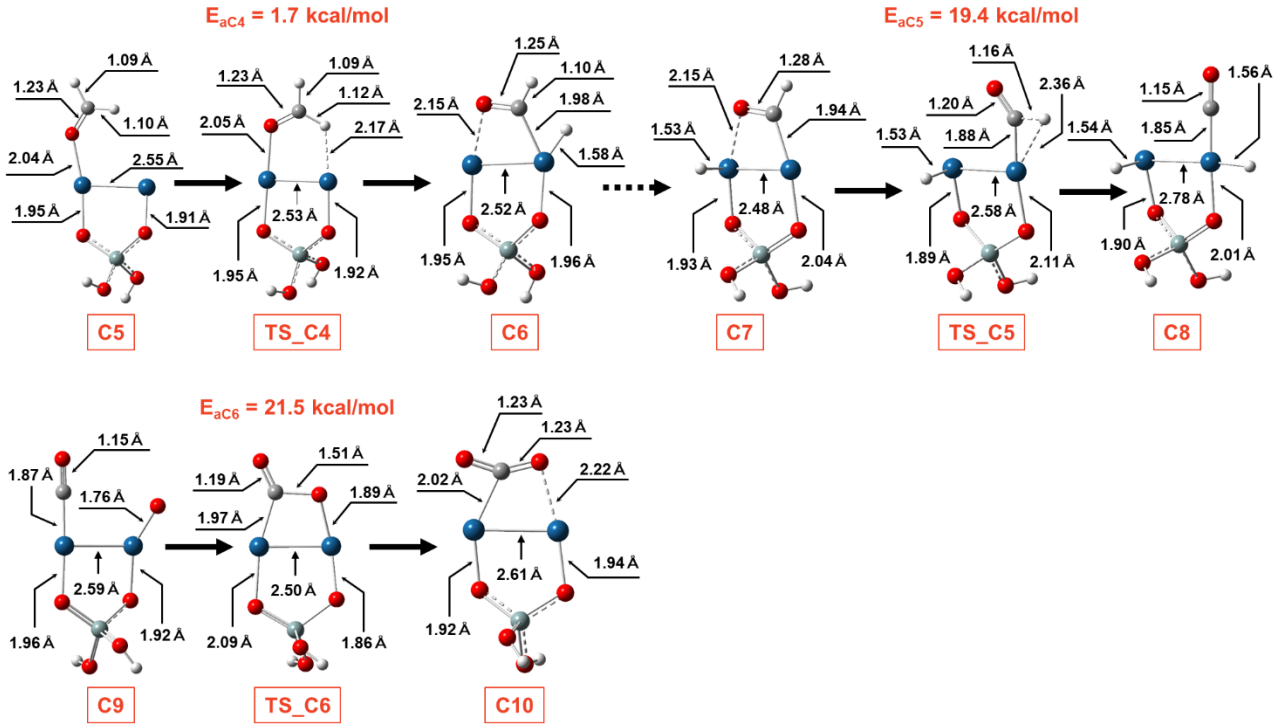

Figure 18. Optimized structures of the reactant, intermediate, transition, and product states of the CO_2 generation from HCHO on the Pt_2-SiO_4 model. White: hydrogen, gray: carbon, red: oxygen, blue: platinum, green: silicon.

3.4 H_2O formation pathway

The DRIFT measurement[4] also suggested that the H atoms, which are generated from HCHO, react with the O atom at the Pt cluster to form H_2O molecules. Since the experiment was performed under oxygen-rich conditions,[4] we adopted a model with two co-adsorbed hydrogen atoms and an oxygen atom as the reactant state (C11 in Figure 19).

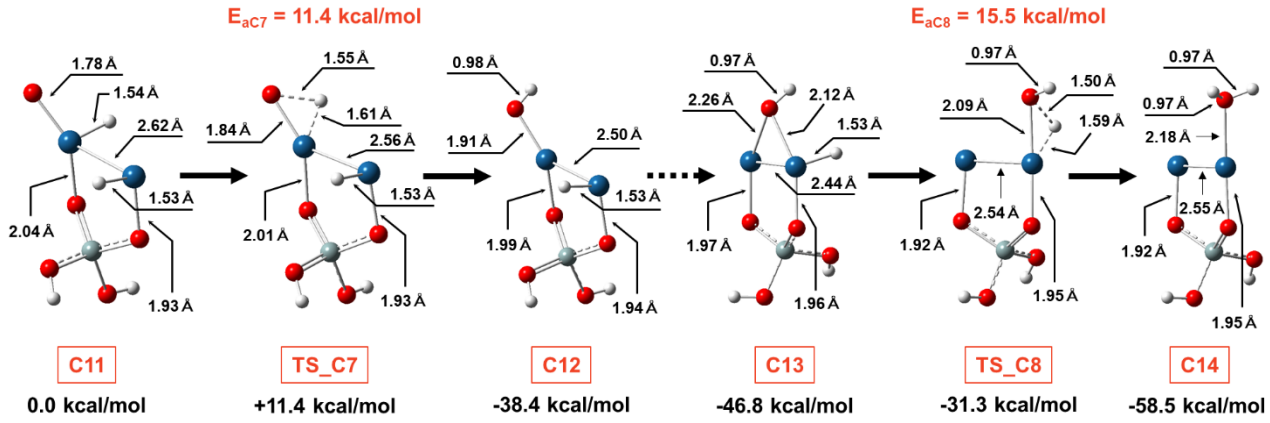

Figure 19. Optimized structures of a reactant state, intermediate state, transition states, and a product state of the H_2O generation on the Pt_2-SiO_4 model. White: hydrogen, red: oxygen, blue: platinum, grey: silicon. Numbers below the structure names are the potential energies relative to C11.

At the C11 state, hydrogenation of atomic oxygen occurs via the TS_C7 state with an activation energy of 11.4 kcal/mol. The OH group at the on-top site (C12) moves to the bridge site (C13), which is more stable than the C12 state by 8.4 kcal/mol. The hydroxy group undergoes hydrogenation with an activation energy of 15.5 kcal/mol to generate H_2O molecule (TS_C8). The barrier heights for the two hydrogenation steps are lower than that of the rate-determining step of the CO oxidation (E_{aC6} = 21.5 kcal/mol with the Pt_2-SiO_4 model, see Figure 17), which indicates that the H_2O formation step is not a rate-determining step.

Furthermore, we investigated the possibility of H_2O formation directly from HCHO, where the H atoms of HCHO are directly abstracted by the adsorbed O atom (see Figure 20). After the O atom attacks one of the H atoms, a C-OH bond is sequentially formed to produce a HCOOH, not a HCO + OH species, with an activation barrier of 21.3 kcal/mol. Although an intramolecular dehydration of formic acid might produce an H_2O molecule, the possibility is safely ruled out by the calculated activation energy (65.9 kcal/mol) and endothermic reaction energy (14.3 kcal/mol). All these investigations suggested that the H_2O formation pathway shown in Figure 19 is reasonable.

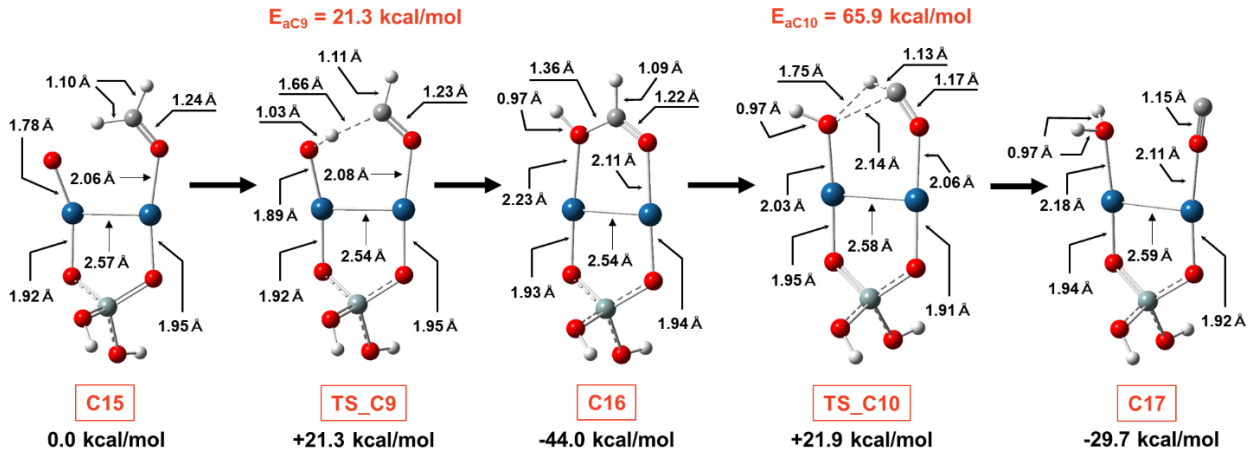

Figure 20. Optimized structures of a reactant, intermediates, transition states and a product of direct dehydration of HCHO by the adsorbed O atom on the Pt_2-SiO_4 model. White ball for hydrogen, red ball for oxygen, blue ball for platinum, and green ball for silicon atom. Numbers below captions of structure names are relative potential energies of each structure in comparison with C15.

We also checked the possibility of H_2 production that could compete with the H_2O formation. Although the activation barrier of the H_2 formation from adsorbed H atoms was calculated to be only 6.8 kcal/mol with the Pt_2-SiO_4 model, the reaction is endothermic (reaction energy of 5.6 kcal/mol), which is in clear contrast to the exothermicity in the H_2O formation. The dissociative adsorption of H_2 molecules proceeds with an activation energy of 1.2 kcal/mol, which is smaller

than the H_2 formation. Therefore, the H_2O formation from adsorbed H and O atoms is a favorable pathway.

4. Conclusions

A mesoporous silica-supported Pt catalyst converts ethylene to CO_2 at low temperatures. Increasing attention has been paid to this system for application to refrigerators and containers for food preservation. From a mechanistic point of view, the reaction mechanism of the C=C bond cleavage is an intriguing subject to be resolved for future catalysis development. In this study, the mechanism of complete oxidation of ethylene on the supported Pt catalyst was studied by DFT calculations. The overall elementary steps are summarized in Scheme 3. Particularly, we focused on the electronic mechanism of the C=C bond breaking in terms of the silica support effect.

Scheme 3. Overall reaction steps investigated in the present study. The numbers below the arrows denote activation energies.

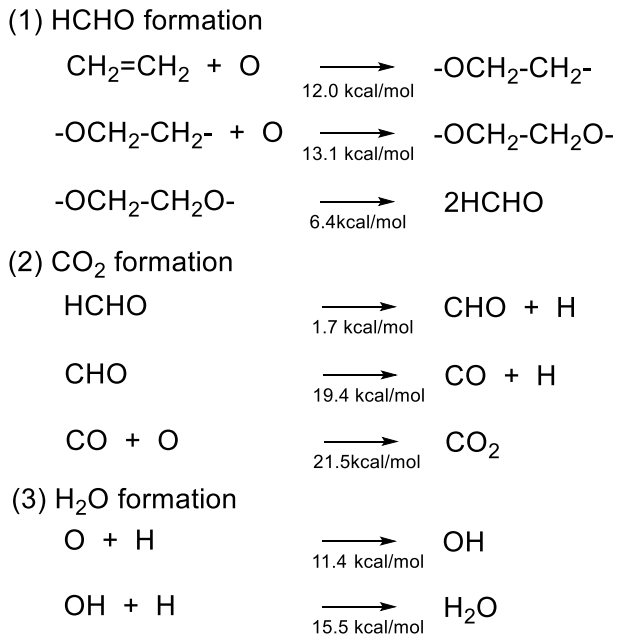

Ethylene is adsorbed on the Pt cluster and sequentially oxygenized to the dioxide intermediate. The silica-support effect weakens the adsorption of ethylene on the Pt catalyst. This moderately weak adsorption reduces the activation energy of the alkoxide formation step. This reaction pathway is energetically more favorable than that via the epoxide intermediate. The dioxide intermediate undergoes C-C σ-bond cleavage to form HCHO. Based on the result of the additional model calculations for analysis, the activation energy of the C-C σ-bond cleavage could be reduced by the edge effect and by the silica support effect. These are the reasons why the C=C bond cleavage reaction occurs easily even at low temperatures. Orbital correlation analysis showed that the electron occupation of the C-C σ-bond orbital is reduced by the reservoir effect of the siloxide group via the Pt δ* orbitals.

Furthermore, the reaction pathway from HCHO to CO and then to CO_2 was also investigated. The results showed that the CO oxidation step is the rate-determining step of all the elementary steps in the complete ethylene oxidation. This result supports and corroborates the proposed reaction mechanism via the HCHO intermediate state.[4] The H_2O formation process was also investigated, and the calculated activation energy was smaller than that in the CO oxidation step.

REFERENCES

1. Imanaka, N.; Masui, T.; Terada, A.; Imadzu, H., Complete oxidation of ethylene at temperatures below 100 degrees C over a $Pt/Ce_{0.64}Zr_{0.16}Bi_{0.20}O_{1.90}$/gamma-$Al_2O_3$ catalyst. *Chem. Lett.* **2008,** *37* (1), 42-43.
2. Ma, C. Y.; Mu, Z.; Li, J. J.; Jin, Y. G.; Cheng, J.; Lu, G. Q.; Hao, Z. P.; Qiao, S. Z., Mesoporous Co_3O_4 and Au/Co_3O_4 catalysts for low-temperature oxidation of trace ethylene. *J. Am. Chem. Soc.* **2010,** *132* (8), 2608-2613.
3. Xue, W. J.; Wang, Y. F.; Li, P.; Liu, Z. T.; Hao, Z. P.; Ma, C. Y., Morphology effects of Co_3O_4 on the catalytic activity of Au/Co_3O_4 catalysts for complete oxidation of trace ethylene. *Catal. Commun.* **2011,** *12* (13), 1265-1268.
4. Jiang, C. X.; Hara, K.; Fukuoka, A., Low-temperature oxidation of ethylene over platinum nanoparticles supported on mesoporous silica. *Angew. Chem. Int. Ed.* **2013,** *52* (24), 6265-6268.
5. Satter, S. S.; Hirayama, J.; Nakajima, K.; Fukuoka, A., Low temparature oxidation of trae ethylene over Pt nanoparticles supported on hydrophobic mesoporus silica. *Chem. Lett.* **2018,** *47*, 1000-1002.
6. Satter, S. S.; Yokoya, T.; Hirayama, J.; Nakajima, K.; Fukuoka, A., Oxidation of trace ethylene at 0 ˚C over platinum nanoparticles supported on silica. *ACS Sustainable Chem. Eng.* **2018,** *6*, 11480-11486.
7. Burnett, D. J.; Gabelnick, A. M.; Fischer, D. A.; Marsh, A. L.; Gland, J. L., In situ soft X-ray studies of ethylene oxidation mechanisms and intermediates on the Pt(111) surface. *J. Phys. Chem. B* **2005,** *109* (12), 5659-66.
8. Wang, H. F.; Wang, D.; Liu, X. H.; Guo, Y. L.; Lu, G. Z.; Hu, P. J., Unexpected C-C bond cleavage mechanism in ethylene combustion at low temperature: Origin and implications. *ACS Catal.* **2016,** *6* (8), 5393-5398.
9. Mikhailov, M. N.; Mishin, I. V.; Kustov, L. M., Platinum nanoparticles as active sites for C-C bond activation in high-silica zeolites. *Microporous Mesoporous Mater.* **2009,** *117* (3), 603-608.
10. Tauster, S. J.; Fung, S. C.; Garten, R. L., Strong metal-support interactions - Group-8 noble-metals supported on TiO_2. *J. Am. Chem. Soc.* **1978,** *100* (1), 170-175.
11. Fu, Q.; Wagner, T., Interaction of nanostructured metal overlayers with oxide surfaces. *Surf. Sci. Rep.* **2007,** *62* (11), 431-498.

12. Freund, H. J.; Pacchioni, G., Oxide ultra-thin films on metals: new materials for the design of supported metal catalysts. *Chem. Soc. Rev.* **2008,** *37* (10), 2224-2242.
13. Isaifan, R. J.; Baranova, E. A., Effect of ionically conductive supports on the catalytic activity of platinum and ruthenium nanoparticles for ethylene complete oxidation. *Catal. Today* **2015,** *241*, 107-113.
14. Ramaker, D. E.; de Graaf, J.; van Veen, J. A. R.; Koningsberger, D. C., Nature of the metal-support interaction in supported Pt catalysts: Shift in Pt valence orbital energy and charge rearrangement. *J. Catal.* **2001,** *203* (1), 7-17.
15. Ewing, C. S.; Veser, G.; McCarthy, J. J.; Lambrecht, D. S.; Johnson, J. K., Predicting catalyst-support interactions between metal nanoparticles and amorphous silica supports. *Surf. Sci.* **2016,** *652*, 278-285.
16. Sutton, L. E., *Tables of Interatomic Distances and Configuration in Molecules and Ions*. London: The Chemical Society: 1965.
17. Huang, S. J.; Hara, K.; Fukuoka, A., Intrinsic catalytic role of mesoporous silica in preferential oxidation of carbon monoxide in excess hydrogen. *Chem. Eur. J.* **2012,** *18* (15), 4738-4747.
18. Ewing, C. S.; Hartmann, M. J.; Martin, K. R.; Musto, A. M.; Padinjarekutt, S. J.; Weiss, E. M.; Veser, G.; McCarthy, J. J.; Johnson, J. K.; Lambrecht, D. S., Structural and electronic properties of Pt_{13} nanoclusters on amorphous silica supports. *J. Phys. Chem. C* **2015,** *119* (5), 2503-2512.
19. Mojet, B. L.; Miller, J. T.; Koningsberger, D. C., The effect of CO adsorption at room temperature on the structure of supported Pt particles. *J. Phys. Chem. B* **1999,** *103* (14), 2724-2734.
20. Ugliengo, P.; Sodupe, M.; Musso, F.; Bush, I. J.; Orlando, R.; Dovesi, R., Realistic models of hydroxylated amorphous silica surfaces and MCM-41 mesoporous material simulated by large-scale periodic B3LYP calculations. *Adv. Mater.* **2008,** *20* (23), 4579-4583.
21. Becke, A. D., Density-functional thermochemistry .3. The role of exact exchange. *J. Chem. Phys.* **1993,** *98* (7), 5648-5652.
22. Lee, C. T.; Yang, W. T.; Parr, R. G., Development of the colle-salvetti correlation-energy formula into a functional of the electron-density. *Phys. Rev. B* **1988,** *37* (2), 785-789.
23. Andrae, D.; Haussermann, U.; Dolg, M.; Stoll, H.; Preuss, H., Energy-adjusted abinitio pseudopotentials for the 2nd and 3rd row transition-elements. *Theoret. Chim. Acta* **1990,** *77* (2), 123-141.
24. Ehlers, A. W.; Bohme, M.; Dapprich, S.; Gobbi, A.; Hollwarth, A.; Jonas, V.; Kohler, K. F.; Stegmann, R.; Veldkamp, A.; Frenking, G., A set of f-polarization functions for pseudo-potential basis-sets of the transition-metals Sc-Cu, Y-Ag and La-Au. *Chem. Phys. Lett.* **1993,** *208* (1-2), 111-114.
25. Hehre, W. J.; Ditchfield, R.; Pople, J. A., Self-consistent molecular-orbital methods .12. Further extensions of gaussian-type basis sets for use in molecular-orbital studies of organic-molecules. *J. Chem. Phys.* **1972,** *56* (5), 2257-2261.
26. Frisch, M. J.; Trucks, G. W.; Schlegel, H. B.; Scuseria, G. E.; Robb, M. A.; Cheeseman, J. R.; Scalmani, G.; Barone, V.; Mennucci, B.; Petersson, G. A., *et al.*, *Gaussian 09*, revision B.01; Gaussian, Inc.: Wallingford, CT, 2009.
27. Gland, J. L., Molecular and atomic adsorption of oxygen on the Pt(111) and Pt(S)-12(111)X(111) surfaces. *Surf. Sci.* **1980,** *93* (2-3), 487-514.

28. Gland, J. L.; Sexton, B. A.; Fisher, G. B., Oxygen interactions with the Pt(111) surface. *Surf. Sci.* **1980,** *95* (2-3), 587-602.
29. Saliba, N.; Tsai, Y. L.; Panja, C.; Koel, B. E., Oxidation of Pt(111) by ozone (O_3) under UHV conditions. *Surf. Sci.* **1999,** *419* (2-3), 79-88.
30. Ibach, H.; Lehwald, S., Identification of surface radicals by vibration spectroscopy: Reactions of C_2H_2, C_2H_4, and H_2 on Pt (111) *J. Vac. Sci. Technol.* **1978,** *15* (2), 407-415.
31. Morokuma, K.; Kitaura, K., Energy Decomposition Analysis of Molecular Interactions. In *Chemical Applications of Atomic and Molecular Electrostatic Potentials*, Politzer, P.; Truhlar, D. G., Eds. Springer: Boston, MA, 1981; pp 215-242.
32. Hoffmann, R., A chemical and theoretical way to look at bonding on surfaces. *Rev Mod Phys* **1988,** *60* (3), 601-628.
33. Ewing, C. S.; Veser, G.; McCarthy, J. J.; Johnson, J. K.; Lambrecht, D. S., Effect of support preparation and nanoparticle size on catalyst-support interactions between Pt and amorphous silica. *J. Phys. Chem. C* **2015,** *119* (34), 19934-19940.

Chapter 4.

Theoretical Study of C-H Activation by O_2 on Negatively Charged Au Cluster: α, β-dehydrogenation of 1-methyl-4-piperidone by the Au/OMS-2 Catalyst

1. Introduction

β-*N*-substituted α, β-unsaturated ketones (enaminones) are very important compounds for fine chemical and pharmaceutical productions as synthetic intermediates for natural products[1-4]. One approach for enaminones synthesis is selective α, β-dehydrogenation of β-*N*-substituted saturated ketones, and several efficient homogeneous catalysts were developed for this reaction[5-13]. On the other hand, heterogeneous catalytic system has advantages for reusability and recovery of products compared with homogeneous catalyst. Although supported Pd nanoparticle catalysts for dehydrogenation of cyclohexanone were reported[14, 15], selective α, β-dehydrogenation of β-*N*-substituted saturated ketones by heterogeneous catalyst was not reported until the development of Au nanoparticles catalyst supported on manganese oxide octahedral molecular sieve OMS-2 (KMn_8O_{16}) (Au/OMS-2 catalyst)[16].

The Au/OMS-2 catalyst is a reusable heterogeneous catalyst for α, β-dehydrogenation of 1-methyl-4-piperidone (Scheme 1). However, detail of the reaction mechanism on this catalyst is not fully understood. Especially, the mechanism of aerobic α, β C-H bonds activation of 1-methyl-4-piperidone on the Au nanoparticle catalyst is particularly interesting. Several previous theoretical studies for C-H bond activation of phenylacetylene[17], methoxy species[18], p-hydroxybenzyl alcohol[19], phenylethanol[20] and small hydrocarbon species[21] on Au cluster catalyst were reported. In these studies, it was pointed out that there are two types of reaction pathways for C-H bond activation; direct C-H bond activated by Au surface or indirect C-H activation by O_2 or oxygen atom adsorbed on the Au cluster. On the other hand, charge state of the Au cluster is changed by interaction between support materials or polymer ligands, and it is also important factor for the catalytic activity as reported in previous theoretical studies[17, 19, 22-29]. In addition, several theoretical study for the relationship between O_2 activation and the charge state of the Au cluster were also reported[30-33]. From these reports, it was suggested that the C-H bond activation

of 1-methyl-4-piperidone on the Au/OMS-2 catalyst is affected by charge state of the Au cluster and adsorbed O_2. However, relationship between the charge state of Au cluster and its effect for the C-H bond activation mechanism of β-*N*-substituted saturated ketone on the heterogeneous Au catalyst have not been reported to the best of our knowledge. Therefore, the reaction mechanism for α, β-dehydrogenation of 1-methyl-4-piperidone on the Au/OMS-2 catalyst was investigated by density functional theory (DFT) calculations in this study. In particular, we focused on the charge state of Au cluster on the OMS-2 support and the relationship between charge state of Au cluster and the C-H bond activation mechanism of 1-methyl-4-piperidone.

Scheme 1. Reaction scheme of α, β-dehydrogenation of 1-methyl-4-piperidone on the Au/OMS-2 catalyst[16]

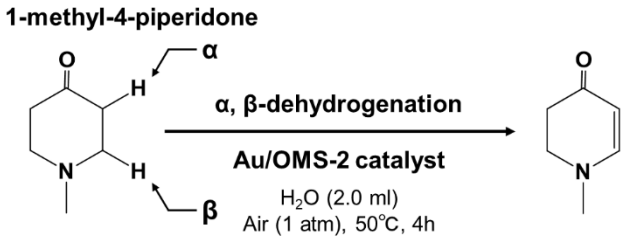

This chapter is organized as follows. In the next section, computational models and details of DFT calculations are shown. In Section 3.1, electronic structure of the Au cluster on the OMS-2 support is discussed (Subsection 3.1.1), and adsorption structure and electronic structure of O_2 on the Au/OMS-2 catalyst are also discussed (Subsection 3.1.2). In Section 3.2, the difference of activation barriers between C-H bond activation of 1-methyl-4-piperidone by Au surface and by O_2 adsorbed on the Au cluster are discussed as the 1st step of the reaction. In addition, the effect of charge state of the Au cluster for each reaction pathway is also discussed. In Section 3.3, the

activity of O_2 adsorbed on the Au cluster, and the effect from charge state of the Au cluster for the O_2 activation are discussed. In Section 3.4, reaction pathways at the 2nd step of the reaction (activation of the remaining C-H bond of 1-methyl-4-piperidone) are discussed. In Section 3.5, the effect from charge state of the Au cluster to reaction pathways at the 2nd step of the reaction is discussed. A concluding remark is given by Section 4.

2. Computational Details

2.1 Au_{10}/OMS-2 Model

To investigate the electronic structure of Au cluster on the OMS-2 support, Au_{10} cluster on the surface slab model of OMS-2 (Au_{10}/OMS-2 model: Figure 1a) was constructed with periodic boundary condition.

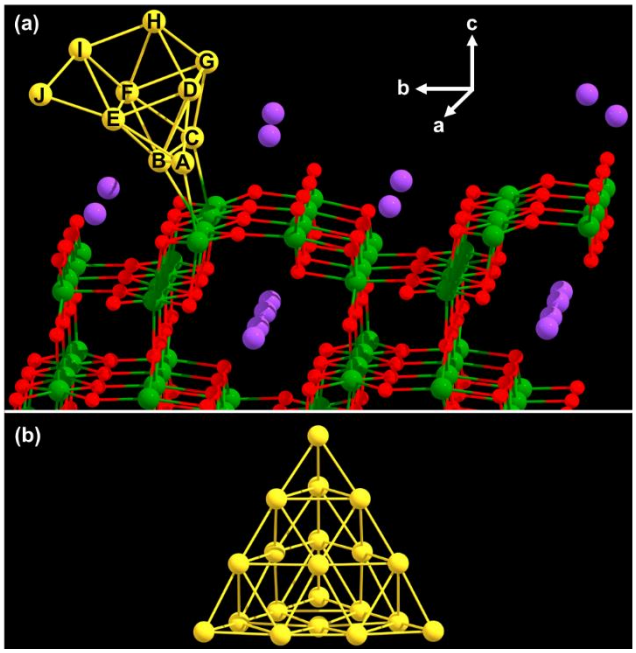

Figure 1. (a) Au_{10}/OMS-2 model. (b) Au_{20} model. Red: oxygen, green: manganese, purple: potassium, yellow: gold.

Tompsett and Islam *et al.* reported that the (100) surface is the most stable surface of α-MnO_2 (i.e. OMS-2 without K atoms) in their previous theoretical calculation[34]. In our calculation, surface energy of the (100) surface of OMS-2 is also more stable than that of (110) surface (the next stable surface of α-MnO_2)[34] by 0.07 J m^{-2}. Therefore, the (100) surface was used for the computational model of the OMS-2 surface in this study. The (100) surface of OMS-2 was modeled by a (4 × 2) unit cell with 25-layers ($K_{40}Mn_{128}O_{256}$: Figure 2). The lattice constant of this slab was set to a = 11.5 Å, b = c = 19.6 Å, α = β = γ = 90 °, which were determined by cell-optimization of the bulk structure of OMS-2. The calculated lattice constant of bulk OMS-2 was in good agreement with the experimental value (a = 11.4 Å, b = c = 19.6 Å (these are multiplied value for (4 × 2) super cell))[35]. Each slab was separated by 25 Å vacuum layer perpendicular to the (100) surface.

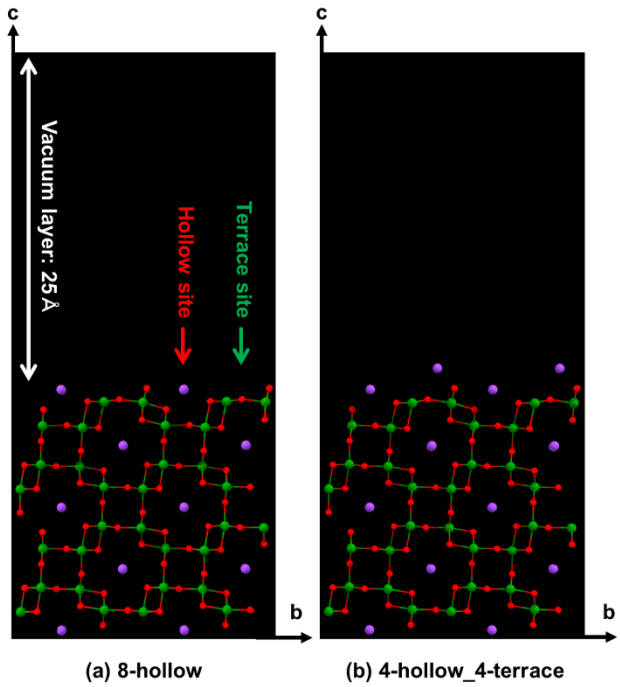

Figure 2. Slab models of the (100) surface of OMS-2 ($K_{40}Mn_{128}O_{256}$). (a) 8-hollow structure (b) 4-hollow_4-terrace structure. Red: oxygen, green: manganese, purple: potassium.

K atoms are at the hollow site, on the (100) surface of OMS-2 if (100) surface is simply cut from the bulk structure as shown in Figure 2a (8-hollow structure). However, once a K atom is moved from the hollow site to the terrace site, such structure (7-hollow_1-terrace structure) is more stable than the 8-hollow structure by 24.0 kcal/mol. Furthermore, when 8-terrace structure (i.e. all K atoms were put on the terrace site) was used as initial surface structure, half of K atoms occupied the terrace site, and the other half K atoms occupied hollow site after the geometry optimization (Figure 2b: 4-hollow_4-terrace structure). The 4-hollow_4-terrace structure is more stable than the 8-hollow structure by 47.1 kcal/mol. While other surface structures (e.g. the 5-hollow_3-terrace structure or the 3-hollow_5-terrace structure) were also constructed, these structures are unstable than the 4-hollow_4-terrace structure. From these results, the 4-hollow_4-terrace structure was adopted in this study. In addition, the Au_{10} model could be adsorbed only on the terrace site of the OMS-2 surface because other adsorption sites were occupied by K atoms in the 4-hollow_4-teracce structure. According to these procedures, the Au_{10}/OMS-2 model (Figure 1a) was constructed to investigate the electronic structure of Au cluster on the OMS-2 surface.

The Au_{10}/OMS-2 model was calculated by spin-polarized DFT calculation with FHI-aims code (version: 171221)[36]. The Perdew−Burke−Ernzerhof (PBE) functional[37] was used as the exchange-correlation functional. The numerical atom-centered orbitals (NAO) basis set[36] with the default “light” settings were used for geometry optimizations, and single-point energy calculations of optimized structures were performed with the default “tight” settings (only the confinement radius for K atoms was changed to 4.0 Å), respectively. In addition, the atomic-scaled zeroth-order regular approximation (Atomic ZORA)[36] was adopted to incorporate the relativistic effects. A Γ-centered grid of 18 × 6 × 6 k-points were used for the cell-optimization

of the bulk OMS-2 structure, and a Γ-centered grid of 5 × 3 × 1 k-points were used for other slab models, respectively. The bottom 11 layers of OMS-2 were fixed to the bulk structure during geometry optimization. Initial spin state of OMS-2 was obtained from previous theoretical calculation by Cockayne *et al*[38].

2.2 Au_{20} Model

The α, β-dehydrogenation of 1-methyl-4-piperidone also proceeds on the Au/C catalyst. This result suggested that lattice oxygen or its vacancy of the OMS-2 support are not essential factors for understanding the reaction mechanism. Therefore, Au_{20} model (cluster model, Figure 1b) was adopted to investigate the reaction pathways of α, β-dehydrogenation of 1-methyl-4-piperidone. Because previous theoretical study[39] showed that tetrahedral pyramidal structure is the most stable conformation of Au_{20}, we adopted tetrahedral pyramidal structure. As shown in Subsection 3.1.1, Au cluster on the OMS-2 support is negatively charged. Therefore, total charge of the Au_{20} model was changed to incorporate the interaction between Au and OMS-2, and three types of Au_{20} models; $Au_{20}^{0\pm}$, Au_{20}^{1-} and Au_{20}^{2-} models were constructed, respectively.

DFT calculation was performed for the Au_{20} model with Gaussian 09 code[40]. The M06 functional[41] was adopted for the exchange-correlation functional. The Stuttgart/Dresden basis set with effective core potential[42] was employed for Au atom, and the 6-31G(d, p) basis sets[43] were used for the other atoms, respectively. The Ultra Fine Grid (99,590 grid) was used for the integration grid of numerical integration. All reactants, products, and transition state structures were connected by intrinsic reaction coordinate (IRC) calculations. In addition, normal mode analysis was performed, and we confirmed that each of the equilibrium and transition states contained zero and one imaginary frequency, respectively.

3. Results and Discussion

3.1 Electronic Structure of Au Cluster and Adsorbed O_2 on the Au/OMS-2 Catalyst

In this section, electronic structure of Au cluster on the OMS-2 support was investigated with the Au_{10}/OMS-2 model. In addition, adsorption structure of O_2 on the Au_{10}/OMS-2 model was also investigated. As discussed below, Au cluster on the OMS-2 support was negatively charged due to charge transfer from OMS-2. Furthermore, adsorbed O_2 was activated by charge transfer from the negatively charged Au cluster.

3.1.1 Electronic Structure of Au Cluster on the OMS-2 Support

In this subsection, electronic structure of Au cluster on the OMS-2 support was investigated by using the Au_{10}/OMS-2 model (Figure 1a). First, Hirshfeld charge analysis[44] was performed to analyze atomic charges of each Au atom (Table 1). As shown in Table 1, total Hirshfeld charge of the Au_{10} cluster in the Au_{10}/OMS-2 model was calculated as -0.42. Especially, Au atoms at 2nd and 3rd layers of the Au_{10} cluster (i.e. Au^D ~ Au^J) are charged more negatively (except for Au^E). From this result, it was suggested that Au cluster on the OMS-2 support is negatively charged.

Table 1. Hirshfeld charge of each Au atom[a]

Au^A	Au^B	Au^C	Au^D	Au^E	Au^F	Au^G	Au^H	Au^I	Au^J	Au_{10}
0.00	0.13	0.02	-0.06	0.01	-0.06	-0.13	-0.09	-0.09	-0.15	-0.42

[a]Indexes of each Au atom are same as shown in Figure 1a.

Next, the electron density difference induced by interaction between the Au_{10} cluster and the OMS-2 support was calculated according to Eq. (1) (Figure 3).

$$\Delta\rho(Au_{10}/OMS\text{-}2) = \rho(Au_{10}/OMS\text{-}2) - \rho(Au_{10}) - \rho(OMS\text{-}2) \quad \dots (1)$$

Where, $\Delta\rho(Au_{10}/OMS\text{-}2)$ is the electron density difference of the Au_{10}/OMS-2 model. ρ(*model name*) is total electron density of each model. $\rho(Au_{10})$ and ρ(OMS-2) were obtained by single point calculation of each region in the Au_{10}/OMS-2 model (i.e. Au_{10} without OMS-2, and OMS-2 without Au_{10}, respectively) with keeping its geometry. As shown in Figure 3, electron density around Au_{10} region is increased. Especially, electron density around Au-Mn bonds and Au atoms at 2nd and 3rd layer of the Au_{10} cluster are increased. In addition, this result is in good agreement with the result of Hirshfeld charge analysis (*cf.* Table 1). On the other hand, electron density around Mn atoms and O atoms of the OMS-2 support are decreased. These results suggested that charge transfer from the OMS-2 support to the Au cluster occurs through Au-Mn bonds. While electron density around K atoms on the surface were also changed, it was expected that that change was induced by charge separation of K atoms against negative charge of the Au cluster rather than charge transfer from K atoms to the Au cluster. Actually, Hirshfeld charge of each K atom is almost same before and after the adsorption of the Au_{10} cluster on the OMS-2 surface.

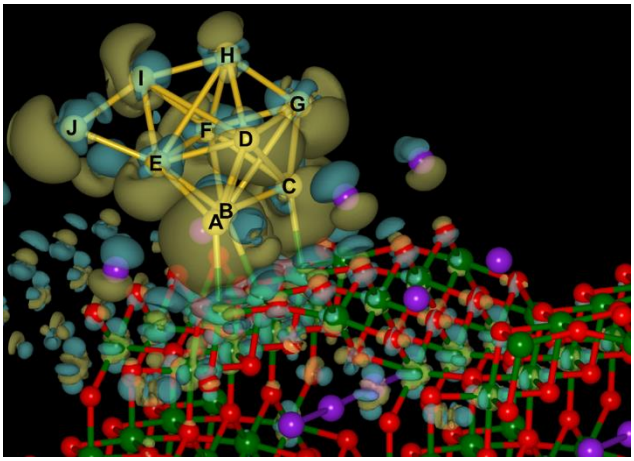

Figure 3. The electron density difference of the Au_{10}/OMS-2 model. Dark yellow isosurface: electron accumulation area, blue isosurface: electron depletion area. Isosurface value is 0.01 $Å^{-3}$. Red ball: oxygen, green ball: manganese, purple ball: potassium, yellow ball: gold.

Finally, density of states (DOS) of the Au_{10}/OMS-2 model was calculated (Figure 4). In present analysis, we focused on the DOS projected to all Au atoms and three Mn atoms bonded to the Au cluster because it was suggested that interaction between Mn and Au is important to the charge transfer by the electron density difference analysis (*cf.* Figure 3). The result of DOS analysis for the Au_{10}/OMS-2 model was shown in Figure 4b. Around the Fermi level, the energy level of valence bands of Au and Mn are well overlapped (pointed by red arrows in Figure 4b). Same DOS analysis was performed for the isolated OMS-2 model (OMS-2 without Au_{10}) and the isolated Au_{10} model (Au_{10} without OMS-2) by the single point calculation, respectively (Figure 4a and 3c). Comparing these DOS results, unfilled bands of the isolated Au_{10} model (pointed by red arrows in Figure 4c) were shifted to filled bands in the Au_{10}/OMS-2 model due to the interaction between Au and Mn. Actually, valence band of Mn of the isolated OMS-2 model (pointed by red arrow in Figure 4a) was also shifted to lower energy state in the Au_{10}/OMS-2

model. Combining with the result of electron density difference analysis, it was suggested that charge density around the OMS-2 surface was moved to the Au cluster through Au-Mn bonds. These results indicated that Au cluster supported on the OMS-2 support is negatively charged due to the charge transfer from the OMS-2 support through the interaction between Au and Mn.

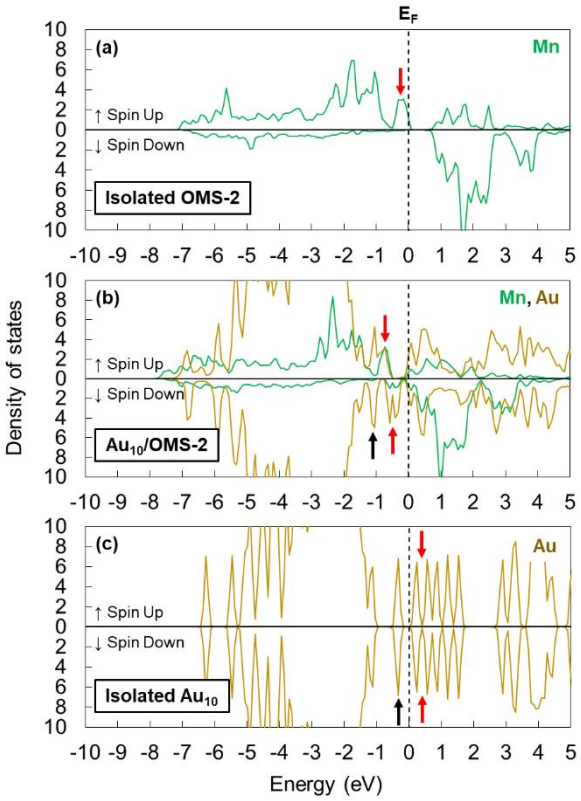

Figure 4. (a) Atom projected DOS of isolated OMS-2 model. (b) Atom projected DOS of the Au_{10}/OMS-2 model. (c) Atom projected DOS of isolated Au_{10} model. Green line: Sum of the total DOS projected to Mn atoms bonded to Au atoms. Yellow line: Sum of the total DOS projected to Au atoms. Fermi energy (E_F) was set to 0.0 eV.

3.1.2 Adsorption Structure of O_2 on the Au_{10}/OMS-2 Model

The α, β-dehydrogenation of 1-methyl-4-piperidone does not proceed on the Au/C catalyst without O_2 although the same reaction proceeds on the Au/C catalyst with O_2. This result suggested that O_2 is essential factor for this reaction while lattice oxygen of the OMS-2 support is not essential. Therefore, adsorption structures and electronic states of O_2 on the Au_{10}/OMS-2 model were investigated in this subsection. In this study, the most negatively charged adsorption site; Ads-site I (bridge site between Au^I and Au^J (*cf.* Figure 1a and Table 1)), and the most positively charged adsorption site; Ads-site II (bridge site between Au^B and Au^E (*cf.* Figure 1a and Table 1)) were selected as adsorption sites for O_2, respectively. Although bridge site between Au^B and Au^C is more positively charged adsorption site than Ads-site II, there is no enough space for O_2 adsorption around this adsorption site. On the other hand, O_2 adsorption and activation at the perimeter region between Au and the metal oxide support were pointed out as one of the key factors for the catalytic activity in other supported Au catalysts (e.g. Au/TiO_2 catalyst[45-49]). However, α, β-dehydrogenation of 1-methyl-4-piperidone also proceeds on the Au/C catalyst. This result suggested that lattice oxygen or its vacancy of the OMS-2 support are not essential factors for this reaction. Therefore, we focused on two adsorption sites at the Au cluster (i.e. Ads-site I and II) in present study.

Adsorption structures of O_2 on each adsorption site were shown in Figure 5. While deformation of the Au_{10} cluster occurred during geometry optimization, adsorption structure of O_2 on the Ads-site I was obtained (Figure 5a). On the other hand, during geometry optimization for O_2 on Ads-site II, O^B was moved from Au^E to Au^I (Ads-site II*: Figure 5b) even though O^B was bonded with Au^E at the initial structure. While Ads-site II is expected as unstable adsorption site, adsorption energies of Ads-site I and II* were calculated as -33.6 kcal/mol and -4.8 kcal/mol, respectively. These results represented that O_2 was adsorbed on both Ads-site I and II* stably,

and O_2 prefers more negatively charged site. Therefore, it was expected that O^B was moved from the positively charged Au^E (Ads-site II) to the negatively charged Au^I (Ads-site II*) during geometry optimization. As shown in Figure 5, O-O bond distance of adsorbed O_2 were elongated on both adsorption sites (1.43 Å (Ads-site I) and 1.41 Å (Ads-site II*)). In addition, adsorbed O_2 shown more than -0.40 negative charge (Table 2). These results suggested that adsorbed O_2 was activated due to charge transfer from the negatively charged Au cluster to π^* orbital of O_2. As discussed in Section 3.2, C-H bond of piperidone molecule is cleaved by this activated O_2 on the negatively charged Au cluster with lower activation energy.

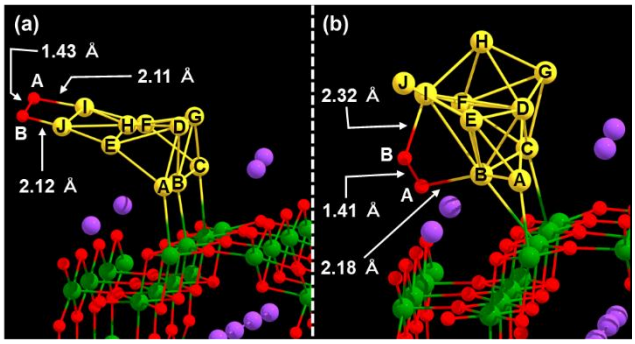

Figure 5. Adsorption structures of O_2 on (a) Ads-site I and (b) Ads-site II*. Red ball: oxygen, green ball: manganese, purple ball: potassium, yellow ball: gold.

Table 2. Hirshfeld charge of Au atoms and adsorbed O_2[a]

	O^A	O^B	Au^A	Au^B	Au^C	Au^D	Au^E
Ads-site I	-0.23	-0.23	-0.02	0.07	-0.02	-0.06	-0.08
Ads-site II*	-0.18	-0.22	0.03	0.15	0.01	-0.04	-0.03
	Au^F	Au^G	Au^H	Au^I	Au^J	O_2	Au_{10}
Ads-site I	-0.08	-0.06	0.01	0.00	0.00	-0.46	-0.24
Ads-site II*	-0.05	-0.15	-0.07	0.00	-0.18	-0.40	-0.33

[a]Indexes of each O and Au are same as shown in Figure 5.

3.2 Reaction Pathway of C-H bond Activation at the 1st Step of the Reaction

In this section, reaction pathways of C-H bond activation of 1-methyl-4-piperidone at the 1st step of the reaction were investigated with the Au_{20} model (Figure 1b). Because it was suggested that lattice oxygen of the OMS-2 support is not essential for this reaction as written in Section 2.2, the Au_{20} model was adopted for the investigation of reaction pathways. In addition, as shown in former sections, Au cluster on the OMS-2 support is negatively charged. Therefore, we focused on the relationship between charge state of Au cluster and catalytic activity for C-H bond activation of 1-methyl-4-piperidone. To investigate this relationship, three types of Au_{20} models; $Au_{20}^{0\pm}$, Au_{20}^{1-} and Au_{20}^{2-} models were constructed by changing total charge of the Au_{20} model. By using these models, two types of C-H bond activation pathways at the 1st step of the reaction (Scheme 2) were investigated. In the direct C-H bond activation pathway (Scheme 2a), C-H bond of 1-methyl-4-piperidone is directly activated by Au atoms. Because it was suggested that O_2 is the essential factor for the reaction, C-H bond activation by O_2 adsorbed on the Au cluster (Scheme 2b: the indirect C-H bond activation pathway by O_2) was also investigated. As discussed below, it was suggested that the indirect C-H bond activation by adsorbed O_2 (Scheme 2b) is the main reaction pathway at the 1st step of the reaction.

Scheme 2. Direct C-H bond activation pathway and indirect C-H bond activation pathway

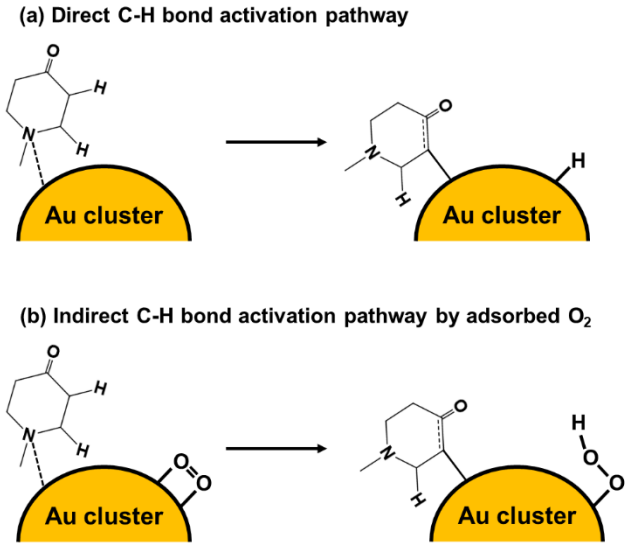

3.2.1 C-H bond Activation at the 1st Step of the Reaction: Direct C-H bond Activation Pathway

First, direct C-H bond activation pathway on Au_{20} models was investigated. In this pathway, C-H bond of 1-methyl-4-piperidone is directly activated on Au surface (Scheme 2a). In this study, the most stable adsorption structure of the reactant molecule was selected as the reactant state. Because 1-methyl-4-piperidone is adsorbed on the Au_{20} model by nitrogen atom, there are three possible adsorption sites in the Au_{20} model; OT1, OT2 and OT3 sites (Figure 10). First, adsorption energies of 1-methyl-4-piperidone on these sites were calculated in each charged model. Adsorption energies of 1-methyl-4-piperidone on each adsorption site were shown in Table 3. In the $Au_{20}^{0\pm}$ model, OT1 site is the most stable adsorption site (adsorption energy = -22.8 kcal/mol). In the Au_{20}^{1-} model and Au_{20}^{2-} model, OT2 and OT3 sites are more stable adsorption sites than OT1 site (adsorption energies of OT2 and OT3 sites are -20.6 kcal/mol in the Au_{20}^{1-} model and -30.0 kcal/mol in the Au_{20}^{2-} model, respectively).

Table 3. Adsorption energies of 1-methyl-4-piperidone on Au_{20} models[a]

E_{ads} (kcal/mol)	OT1	OT2	OT3
$Au_{20}^{0\pm}$model	-22.8	-20.5	-21.0
Au_{20}^{1-}model	-18.5	-20.6	-20.6
Au_{20}^{2-}model	-23.0	-30.0	-30.0

[a]For the definitions of each adsorption site (i.e. OT1, OT2 and OT3), see Figure 10.

Therefore, 1-methyl-4-piperidone on OT1 site is reactant state of the $Au_{20}^{0\pm}$ model, on OT2 site or OT3 site are reactant states of the Au_{20}^{1-} model and Au_{20}^{2-} models, respectively. From these reactant states, all possible direct C-H bond activation pathways on neighbor Au atoms of the reactant molecule were investigated. In addition, both α_C-H bond activation pathway and β_C-H bond activation pathway (*cf.* Scheme 1) were investigated as the 1st step of the reaction.

Potential energy diagrams of direct α_C-H bond activation pathways on each model were shown in Figure 6 as broken lines. Reaction pathways with the lowest activation energy among obtained pathways based on the above procedure were shown in this diagram. In addition, optimized structures of each state of reaction pathways were also shown in Figure 7. As shown in Figure 6, activation energies of this reaction pathway were higher than 40 kcal/mol in all models ($Au_{20}^{0\pm}$ model: E_{aA1} = 54.2 kcal/mol, Au_{20}^{1-} model: E_{aB1} = 44.8 kcal/mol and Au_{20}^{2-} model: E_{aC1} = 44.7 kcal/mol, respectively). Furthermore, these reaction pathways were calculated as endothermic reaction because product states (A2, B2 and C2 in Figure 6 and 6) were unstable than reactant states (A1, B1 and C1 in Figure 6 and 6) in all models by 44.2 kcal/mol, 41.9 kcal/mol and 18.7 kcal/mol, respectively. Although direct β_C-H bond activation pathways were also investigated (see Figure 8 and 9), activation energies of the direct β_C-H bond activation were higher than those of the direct α_C-H bond activation in the Au_{20}^{1-} and Au_{20}^{2-} models by 0.7 kcal/mol and 8.7 kcal/mol, respectively (*cf.* E_{aB3} and E_{aC3} in Figure 8). On the other hand,

activation energy of the direct β_C-H bond activation in the $Au_{20}^{0\pm}$ model was lower than that of direct the α_C-H bond activation by 11.8 kcal/mol. However, reactant state of the β_C-H bond activation (A3 in Figure 9) is physisorption structure of 1-methyl-4-piperidone, and A3 state is unstable than A1 state (reactant state of α_C-H bond activation; Figure 7) by 3.9 kcal/mol. We could not find transition state for the direct β_C-H bond activation which is connected to chemisorbed 1-methyl-4-piperidone on OT1 site in the $Au_{20}^{0\pm}$ model. In addition, product states of the direct β_C-H bond activation pathways (A4, C6 and B5 in Figure 8 and 9) were unstable than reactant states (A3, B1 and C5 in Figure 8 and 9) by 41.3 kcal/mol, 34.5 kcal/mol and 51.8 kcal/mol, respectively. Therefore, the direct β_C-H activation pathways were also calculated as endothermic reaction with high activation energies (> 40 kcal/mol). From these results, it was investigated that direct C-H bond activation on the Au/OMS-2 catalyst is unfavorable reaction pathway. In addition, the charge state of the Au cluster does not affect the qualitative trend (i.e. endothermic reaction with large activation barrier) of this pathway.

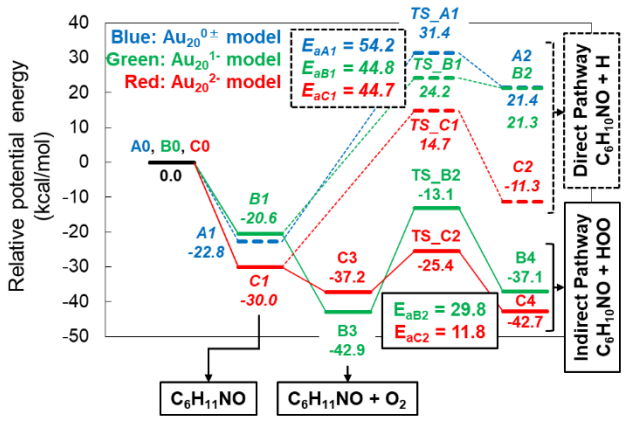

Figure 6. Potential energy diagram of α_C-H bond activation at the 1st step of the reaction. Broken lines: direct α_C-H activation pathways, solid lines: indirect α_C-H bond activation pathways. Energies of A0, B0, and C0 states are defined as the sum of the energies of the isolated species: $Au_{20}^{0\pm}$, O_2, and 1-methyl-4-piperidone for A0; Au_{20}^{1-}, O_2, and 1-methyl-4-piperidone for B0; Au_{20}^{2-}, O_2, and 1-methyl-4-piperidone for C0.

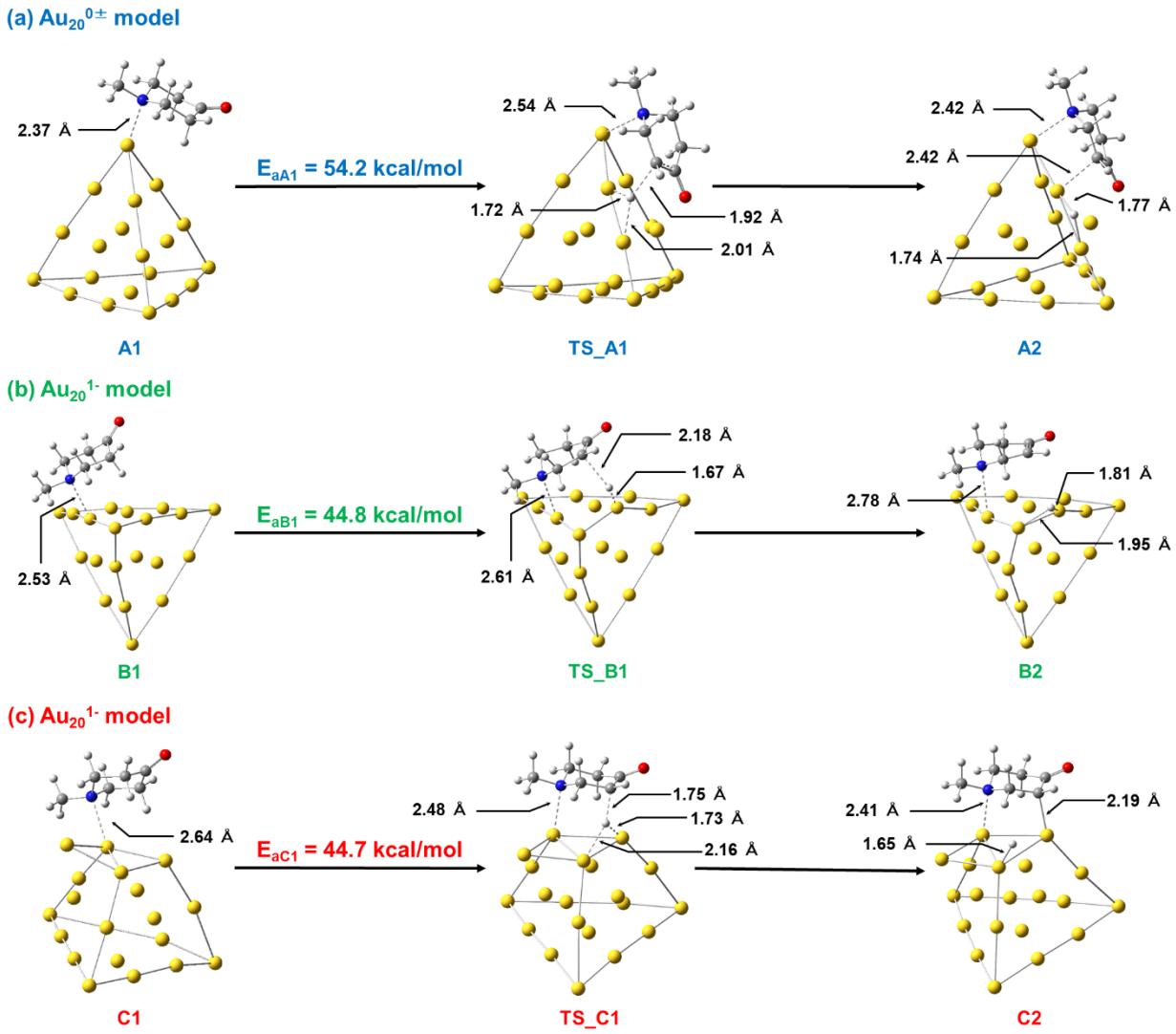

Figure 7. Optimized structures of the reactant, product and transition states of the direct α_C-H bond activation at the 1st step of the reaction on the (a) $Au_{20}^{0\pm}$ model, (b) Au_{20}^{1-} model and (c) Au_{20}^{2-} model. Red ball: oxygen, blue ball: nitrogen, gray ball: carbon, white ball: hydrogen, yellow ball: gold.

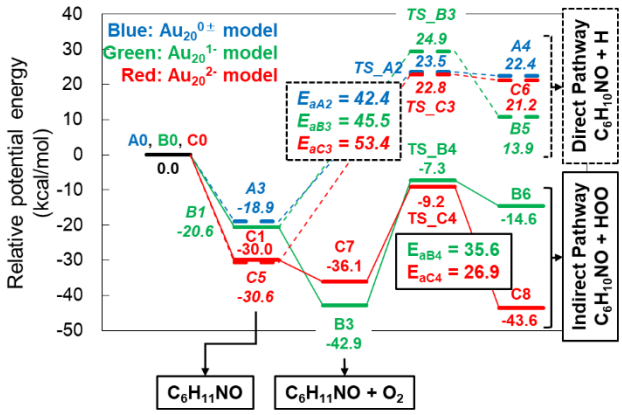

Figure 8. Potential energy diagram of β_C-H bond activation at the 1st step of the reaction. Broken lines: direct β_C-H activation pathways, solid lines: indirect β_C-H bond activation pathways. Energies of A0, B0, and C0 states are defined as the sum of the energies of the isolated species: $Au_{20}^{0\pm}$, O_2, and 1-methyl-4-piperidone for A0; Au_{20}^{1-}, O_2, and 1-methyl-4-piperidone for B0; Au_{20}^{2-}, O_2, and 1-methyl-4-piperidone for C0.

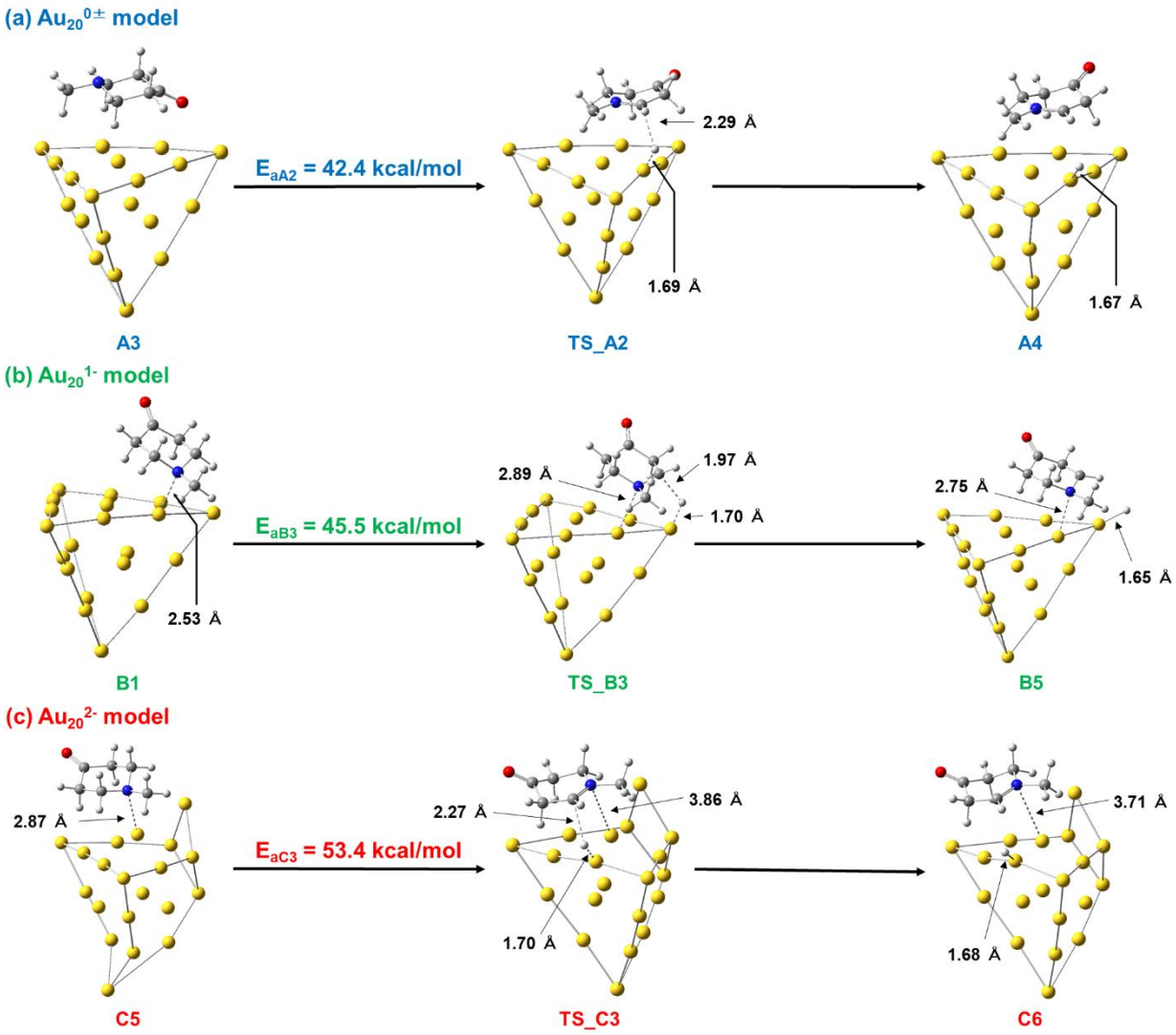

Figure 9. Optimized structures of the reactant, product and transition states of direct β_C-H bond activation at the 1st step of the reaction on the (a) $Au_{20}^{0\pm}$ model, (b) Au_{20}^{1-} model and (c) Au_{20}^{2-} model. Red ball: oxygen, blue ball: nitrogen, gray ball: carbon, white ball: hydrogen, yellow ball: gold.

3.2.2 C-H bond Activation at the 1st Step of the Reaction: Indirect C-H bond Activation Pathway

It was suggested that O_2 is essential for the reaction by the experimental result on the Au/C catalyst. Therefore, indirect C-H activation pathway by adsorbed O_2 at the 1st step of the reaction was investigated with the Au_{20} model in this subsection. In this pathway, α- or β-hydrogen atom is moved from 1-methyl-4-piperidone to adsorbed O_2 (Scheme 2b). This indirect C-H bond activation mechanism by adsorbed O_2 on Au cluster was also reported by previous theoretical study for methanol oxidation[18] and C-H activation of several small hydrocarbon species[21]. First, adsorption structures of O_2 on the Au_{20} model were investigated based on previous theoretical study by Ehara and Sakurai *et al*[18]. Adsorption sites of O_2 on the Au_{20} model considered in present study were shown in Figure 10, and adsorption energies of O_2 on these adsorption sites were summarized in Table 4. In the $Au_{20}^{0\pm}$ model, adsorption energies for any adsorption sites were calculated as positive values. This result indicated that O_2 is not adsorbed on $Au_{20}^{0\pm}$ model stably. On the other hand, adsorption energies showed negative values both in the Au_{20}^{1-} model and Au_{20}^{2-} model (except for that of OT2 site in the Au_{20}^{2-} model). This result indicated that O_2 is adsorbed on negatively charged Au_{20} models stably. The most stable adsorption site is BR1 site in both models. Comparing adsorption energies for BR1 site in both models, O_2 is adsorbed on the Au_{20}^{1-} model stronger than on the Au_{20}^{2-} model by 8.6 kcal/mol. In addition, O-O bond distance is elongated as negative charge of the Au_{20} model increases. More details for electronic structure of adsorbed O_2 were shown in Section 3.3.

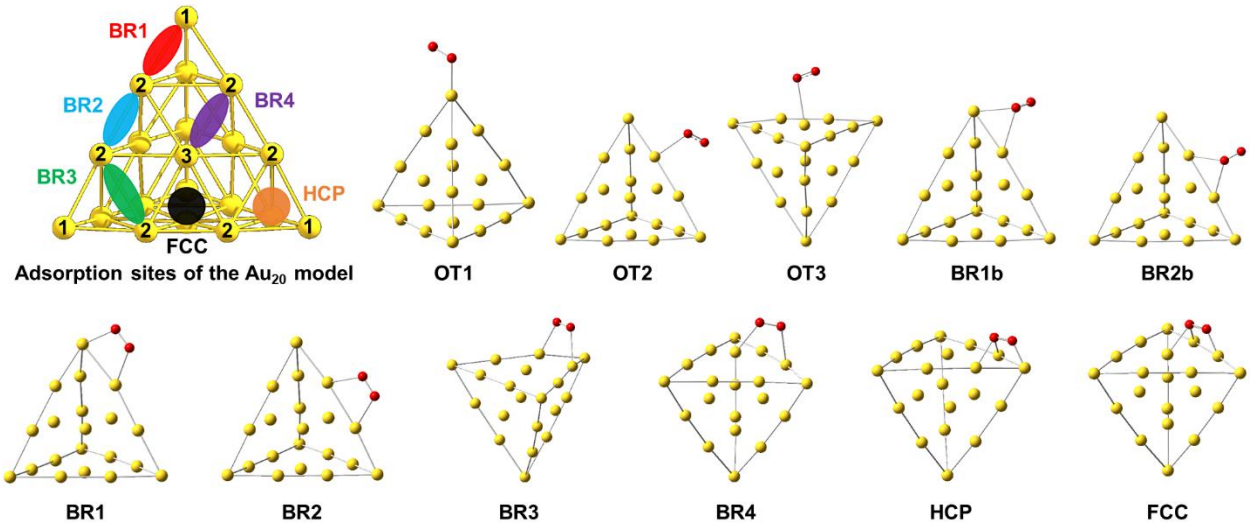

Figure 10. Adsorption sites of the Au_{20} model (numbers on each Au atom represent OT1 site, OT2 site and OT3 site, respectively), and examples of adsorption structures of O_2 on each adsorption site. Yellow ball: gold, red ball: oxygen.

Table 4. Adsorption energies and O-O bond distances of O_2 on each Au_{20} model

		OT1	OT2	OT3	HCP	FCC
$Au_{20}^{0\pm}$model	E_{ads} (kcal/mol)	27.4	28.5	30.4	Converged to BR1b	Converged to OT2
	O-O distance (Å)	1.23	1.23	1.20		
Au_{20}^{1-}model	E_{ads} (kcal/mol)	-18.0	-11.2[b]	-7.6	Converged to BR1	Converged to BR4
	O-O distance (Å)	1.29	1.28[b]	1.23		
Au_{20}^{2-}model	E_{ads} (kcal/mol)	-0.1	4.1[b]	Converged to BR2	-6.2	-3.9
	O-O distance (Å)	1.31	1.32[b]		1.41	1.38

		BR1	BR2	BR3	BR4
$Au_{20}^{0\pm}$model	E_{ads} (kcal/mol)	25.3[a]	31.4	28.6	29.0
	O-O distance (Å)	1.25[a]	1.20	1.22	1.22
Au_{20}^{1-}model	E_{ads} (kcal/mol)	-21.1	-16.1	-12.5	-11.7
	O-O distance (Å)	1.30	1.29	1.29	1.29
Au_{20}^{2-}model	E_{ads} (kcal/mol)	-12.5	-5.1	Converged to HCP	Converged to FCC
	O-O distance (Å)	1.40	1.35		

[a]Converged to BR2b. [b]Converged to BR1b.

In the present study, adsorption structures of O_2 on the $Au_{20}^{0\pm}$ model and Au_{20}^{2-} model were calculated as singlet state, and O_2 on the Au_{20}^{1-} model was calculated as doublet state, respectively. If adsorption structure was calculated as triplet state in the $Au_{20}^{0\pm}$ model, O_2 was adsorbed as physisorbed (or desorbed) structure with long Au-O distance (> 2.6 Å) although adsorption energies showed small negative values (-5 ~ -6 kcal/mol). Therefore, it was investigated that O_2 is not adsorbed on the $Au_{20}^{0\pm}$ model both in singlet state and triplet state. If adsorption structures were calculated as quartet state in the Au_{20}^{1-} model, similar physisorbed (or desorbed) adsorption structures were also obtained with smaller adsorption energies (-5 ~ -6 kcal/mol) than those in doublet state. Therefore, it was investigated that O_2 is adsorbed on the Au_{20}^{1-} model stably in doublet state. If adsorption structures were calculated as triplet state in the Au_{20}^{2-} model, stable chemisorption structures were obtained. The most stable adsorption site in triplet state is also BR1 site, and adsorption energy was calculated as -21.7 kcal/mol which is larger than that in singlet state by 9.2 kcal/mol. However, co-adsorption structure of O_2 and 1-methyl-4-piperidone on the Au_{20}^{2-} (C3 in Figure 11) in triplet state is stable than that in singlet state only by 5.7 kcal/mol. In addition, transition state for the indirect C-H activation by O_2 (TS_C2) and its product state (C4) are unstable in triplet state than those in singlet state by 4.5 kcal/mol and 5.9 kcal/mol, respectively. From these results, the $Au_{20}^{0\pm}$ model and Au_{20}^{2-} model were calculated as singlet state, and the Au_{20}^{1-} model was calculated as doublet state in present study. In addition, it was pointed out that O_2 dissociation on both neutral Au cluster and negatively charged Au cluster are unfavorable (except for very *special* size cluster) by previous theoretical study[30]. Furthermore, Au cluster on the OMS-2 support is negatively charged as shown in Section 3.1. Therefore, the indirect C-H activation pathway by adsorbed O_2 was investigated with the Au_{20}^{1-} model and Au_{20}^{2-} model. From the results of Table 4, BR1 site (i.e.

the most stable adsorption site of both models) was selected as adsorption site of O_2 at the reactant state. In addition, 1-methyl-4-piperidone was put on neighboring adsorption sites of O_2 on BR1 site. From such co-adsorption structures of O_2 and 1-methyl-4-piperidone, all possible indirect α_ or β_C-H bond activation pathways were investigated.

Potential energy diagrams of indirect α_C-H bond activation pathways on each model were shown in Figure 6 as solid lines. Reaction pathways with the lowest activation energy among obtained pathways based on the above procedure were shown in this diagram. As shown in Figure 6, activation energies of this reaction pathway were lower than 30 kcal/mol in both models (Au_{20}^{1-} model: E_{aB2} = 29.8 kcal/mol and Au_{20}^{2-} model: E_{aC2} = 11.8 kcal/mol, respectively). These values are lower than those of the direct C-H bond activation pathway more than 15 kcal/mol. Furthermore, relative stability of the product state compared with the reactant state is considerably changed. In the Au_{20}^{1-} model, reaction energy (E_r: energy difference between reactant state (E[R]) and product state (E[P]); E_r = E[P] – E[R]) of the indirect pathway is only +5.8 kcal/mol although that of the direct pathway is +41.9 kcal/mol. Especially, reaction energy of the indirect pathway in the Au_{20}^{2-} model is -5.5 kcal/mol while that of the direct pathway is +18.7 kcal/mol. This result suggested that indirect α_C-H bond activation on the Au_{20}^{2-} model proceeds as exothermic reaction with relatively low activation energy (11.8 kcal/mol). In addition, indirect β_C-H bond activation pathway was also investigated (Figure 8 and Figure 12). However, activation energies of the indirect β_C-H bond activation were higher than those of the indirect α_C-H bond activation by 5.8 kcal/mol in the Au_{20}^{1-} model and 15.1 kcal/mol in the Au_{20}^{2-} model, respectively. The difference of the activation barrier between α_C-H bond activation and β_C-H bond activation could be explained by stability of the conjugate base. Product molecule (conjugate base) of α-deprotonation of 1-methyl-4-piperidone is more

stable than that of β-deprotonation by 36.1 kcal/mol in gas phase. In brief, acidity of α-hydrogen is higher than β-hydrogen. This is one of the reason why activation energy of α_C-H bond activation is lower than that of β_C-H bond activation in the indirect C-H bond activation pathway. From these results, it was suggested that the indirect α_C-H bond activation by adsorbed O_2 is the main pathway of the 1st reaction step. In addition, this reaction pathway proceeds on the negatively charged Au cluster, and activation energy is lower in more negatively charged Au cluster.

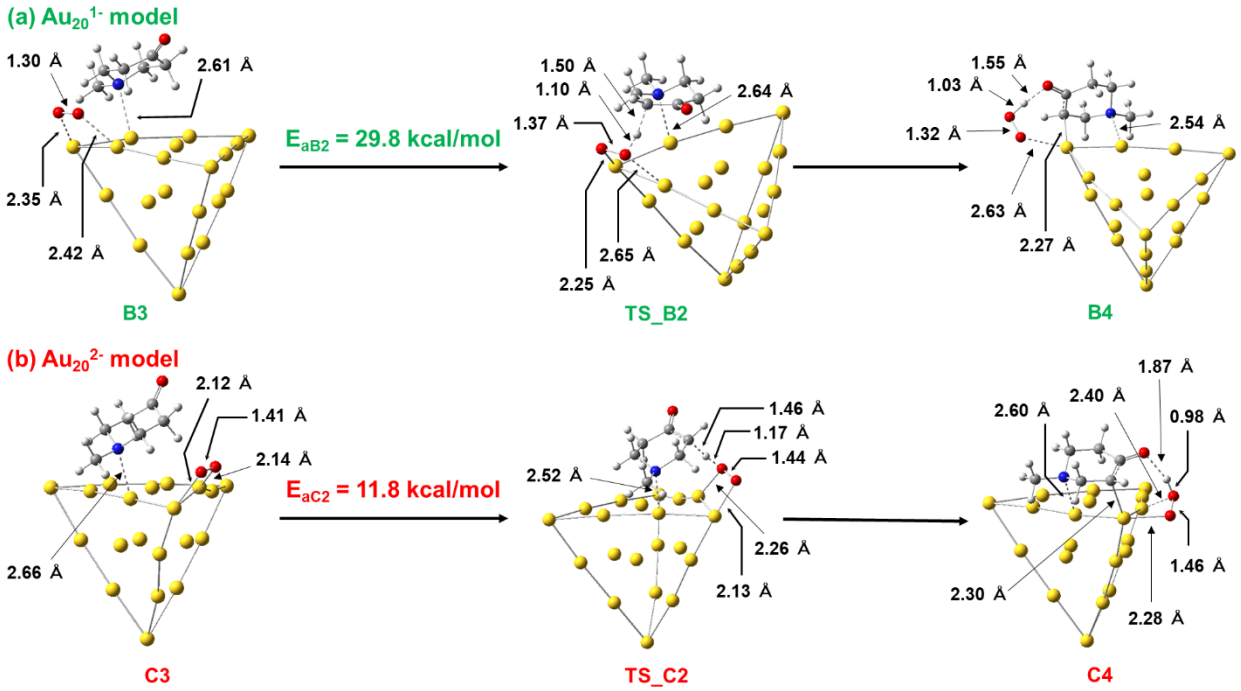

Figure 11. Optimized structures of the reactant, product and transition states of indirect α_C-H bond activation at the 1st step of the reaction on the (a) Au_{20}^{1-} model and (b) Au_{20}^{2-} model. Red ball: oxygen, blue ball: nitrogen, gray ball: carbon, white ball: hydrogen, yellow ball: gold.

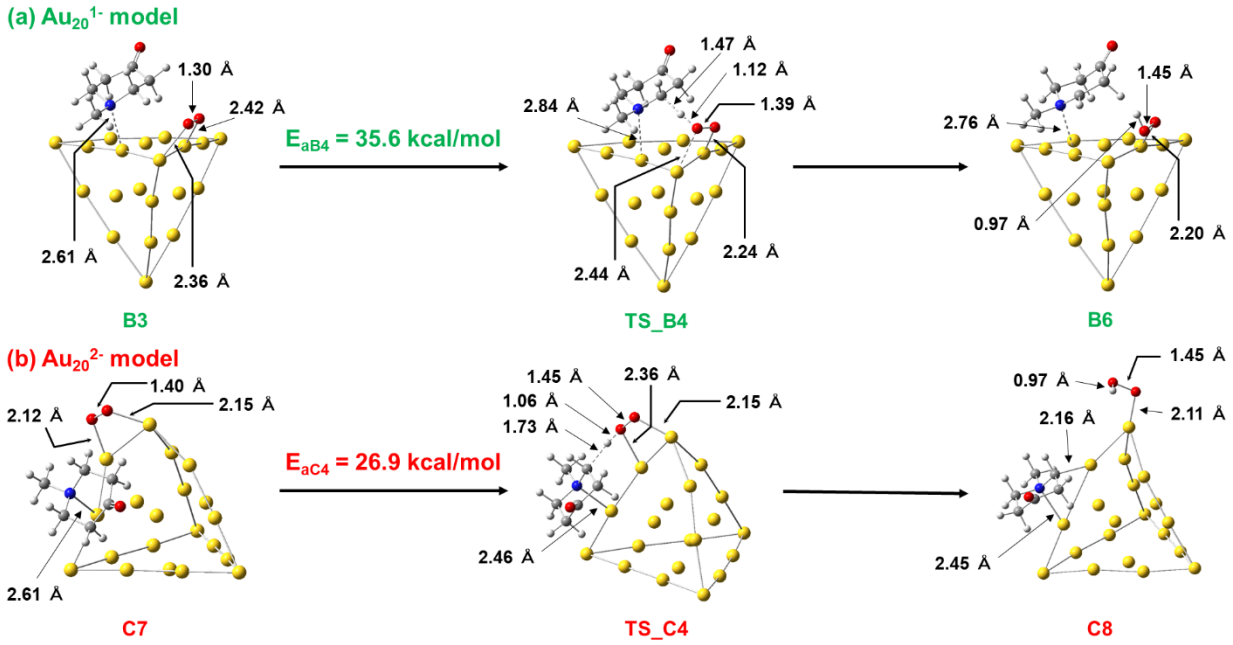

Figure 12. Optimized structures of the reactant, product and transition states of indirect β_C-H bond activation at the 1st step of the reaction on the (a) Au_{20}^{1-} model and (b) Au_{20}^{2-} model. Red ball: oxygen, blue ball: nitrogen, gray ball: carbon, white ball: hydrogen, yellow ball: gold.

3.3 Electronic Structure of O_2 on the Au Cluster

From the results of former sections, the indirect α_C-H bond activation pathway by adsorbed O_2 was suggested as the main reaction pathway at the 1st step of the reaction. In this section, electronic structure of adsorbed O_2 on the Au_{20} model was investigated to understand the relationship between the charge state of Au cluster and O_2 activation. As shown in below, O_2 is well activated for hydrogen abstraction via charge transfer from the negatively charged Au cluster.

First, the highest occupied molecular orbital (HOMO) of the most stable adsorption structure of O_2 on each Au_{20} model (*cf.* Table 4) was investigated. As shown in Figure8, HOMO is

delocalized on both Au_{20} region and π^* orbital of O_2 in the $Au_{20}^{0\pm}$ model and Au_{20}^{1-} model. However, HOMO of β-spin (HOMO (β)) is more localized on π^* orbital of O_2 than HOMO of α-spin (HOMO (α)) or HOMO of the $Au_{20}^{0\pm}$ model. On the other hand, HOMO is almost localized on π^* orbital of O_2 in the Au_{20}^{2-} model. Actually, O-O bond distance and negative charge on O_2 are larger in more negatively charged model as shown in Figure 14 and Table 6. From these results, it was investigated that O_2 is well activated on negatively charged Au_{20} models due to the charge transfer from Au cluster to π^* orbital of O_2. Furthermore, electronic structure of adsorbed O_2 on the Au_{20} model and that on the Au_{10}/OMS-2 model was compared.

As shown in Section 2, computational settings were different between the Au_{10}/OMS-2 model (PBE functional with FHI-aims code) and the Au_{20} model (M06 functional with Gaussian 09 code). Therefore, difference between these computational settings were investigated by using adsorption structure of O_2 on the Au_{20} model. Optimized adsorption structures by using the calculation setting for the Au_{10}/OMS-2 model were shown in Figure 13. Comparing the result in Figure 14, maximum difference for Au-O bond is 0.2 Å, and for O-O bond is 0.04 Å, respectively. In addition, root-mean-square-deviation (RMSD: see Eq. S1) between optimized structures in Figure 14 and Figure 13 is less than 0.16 Å in each model.

$$\mathrm{RMSD} = \sqrt{\frac{1}{N}\sum_{t=1}^{N} d_i^2} \quad \ldots \text{(S1)}$$

Where, N is total number of atoms in the system, and d_i is distance between corresponding atoms between two models. Therefore, it was investigated that there is only small difference for the geometry between two settings. Furthermore, results of Hirshfeld charge analysis for adsorbed O_2 were shown in Table 5. Although difference of Hirshfeld charge in the Au_{20}^{1-} model and Au_{20}^{2-} model is slightly large, qualitative tendency of Hirshfeld charge of O_2 is same between two settings (i.e. Hirshfeld charge of O_2 becomes more negative as negative charge of the Au_{20}

model increases). From these results, it was investigated that qualitative tendency of O_2 adsorption on the Au_{20} model by each calculation setting agrees well.

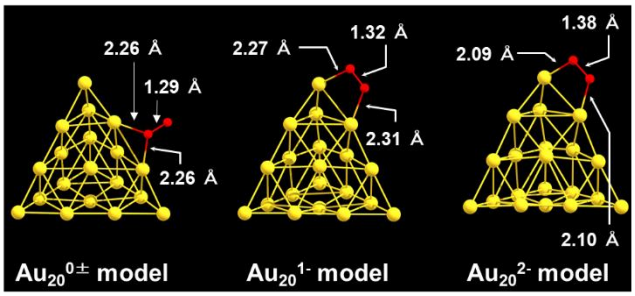

Figure 13. Adsorption structures of O_2 on each Au_{20} model optimized by using the calculation setting for the Au_{10}/OMS-2 model. Yellow ball: gold, red ball: oxygen.

Table 5. Hirshfeld charge of O_2 on each Au_{20} model

	$Au_{20}^{0\pm}$ model	Au_{20}^{1-} model	Au_{20}^{2-} model
FHI-aims[a]	-0.24	-0.31	-0.51
Gaussian[b]	-0.31	-0.50	-0.78

[a]Result by calculation setting for the Au_{10}/OMS-2 model. [b]Result by calculation setting for the Au_{20} model.

As shown in Section 3.1.2, sum of Hirshfeld charge of the Au_{10} cluster and O_2 is -0.70 when O_2 is adsorbed on the Ads-site I of the Au_{10}/OMS-2 model (*cf.* Table 2). In addition, both natural population analysis (NPA) charge and Hirshfeld charge of O_2 on the Au_{20}^{1-} model (-0.54 and -0.50, respectively) are similar with Hirshfeld charge of O_2 on the Ads-site I (-0.46). On the other hand, geometry structure (O-O bond and Au-O bond distances) of O_2 on the Ads-site I is similar with that on the Au_{20}^{2-} model (*cf.* Figure 5a and Figure 14). Especially, O-O bond distances of O_2 on the Ads-site I and the Au_{20}^{2-} model are 1.43 Å and 1.40 Å, respectively while that on the Au_{20}^{1-} model is 1.30 Å. From these results, charge state of O_2 on the Au_{10}/OMS-2 model is

similar with that on the Au_{20}^{1-} model, and geometry structure of O_2 on the Au_{10}/OMS-2 model is similar with that on the Au_{20}^{2-} model. Therefore, it was suggested that electronic structure of O_2 on the Au_{10}/OMS-2 model is well represented by negatively charged Au_{20} models.

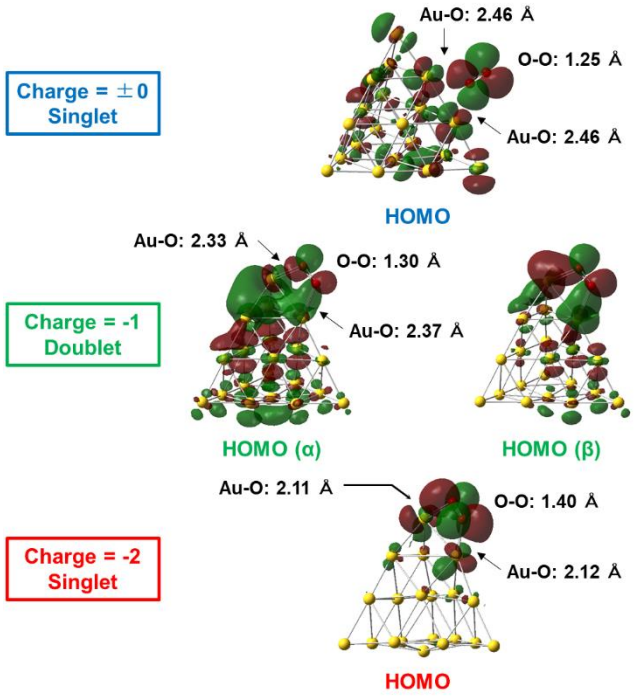

Figure 14. HOMO of adsorption structures of O_2 on each Au_{20} model. Isosurface value is 0.02 $Å^{-3}$. Red ball: oxygen, yellow ball: gold.

Table 6. Electronic charge of adsorbed O_2 on each model.

	$Au_{20}^{0\pm}$ model	Au_{20}^{1-} model	Au_{20}^{2-} model	Au_{10}/OMS-2 model (Ads-site I)
NPA Charge of O_2	-0.27	-0.54	-0.95	-
Hirshfeld Charge of O_2	-0.31	-0.50	-0.78	-0.46

Next, energy levels of HOMO, the singly occupied molecular orbital (SOMO) and the lowest unoccupied molecular orbital (LUMO) of isolated Au_{20} models and O_2 molecule were investigated, respectively. As shown in Figure 15, HOMO (SOMO) levels of isolated Au_{20} models go up as total charge becomes more negatively. Especially, HOMO levels of the Au_{20}^{1-} model and the Au_{20}^{2-} model are higher than LUMO level of O_2. On the other hand, HOMO level of the $Au_{20}^{0\pm}$ model is lower than LUMO level of O_2. This is one of the reason why O_2 is well activated on negatively charged Au_{20} models. However, orbital energy of HOMO of the Au_{20}^{2-} model shows positive value because the Au_{20}^{2-} model and the Au_{20}^{1-} model are artificial models with additional excess electrons. Although there is possibility of overestimate the activity of these models, it was expected that such negatively charged Au cluster is stabilized by the interaction between the OMS-2 support in the Au/OMS-2 catalyst. Actually, Fermi energy of the Au_{10}/OMS-2 model was calculated as -4.71 eV even though the Au_{10} cluster is negatively charged in the Au_{10}/OMS-2 model. In addition, adsorption structure of O_2 on the Au_{10}/OMS-2 model is only represented by negatively charged Au_{20} models without drastic over activation of O_2 as shown in above. From these results, it was investigated that O_2 on negatively charged Au_{20} models is well activated by charge transfer from Au cluster to O_2 due to the difference of HOMO level and LUMO level between Au_{20} models and O_2. In addition, it was suggested that this is one of the reason why the indirect C-H bond activation by O_2 proceeds with low activation energy.

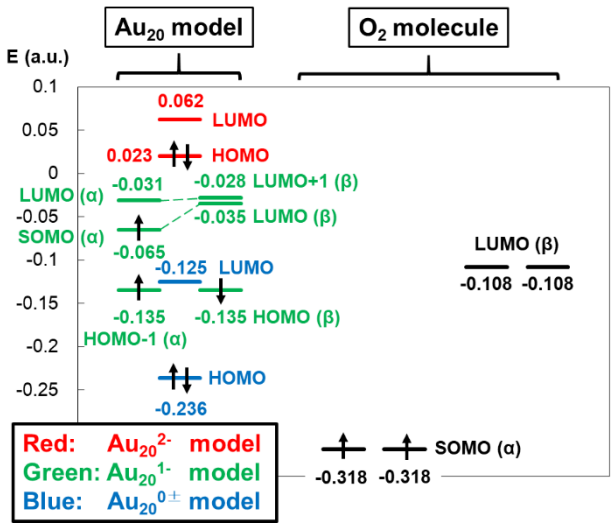

Figure 15. Orbital energy diagram of isolated Au_{20} models and O_2.

Finally, affinities for hydrogen of adsorbed O_2 was calculated to investigate the interaction between activated O_2 and hydrogen. First, adsorption structure of HOO species on the Au_{20}^{1-} model and Au_{20}^{2-} model were calculated, respectively. Initial structures for geometry optimization of each adsorption structure were taken from product states of the indirect pathway at the 1st reaction step. Next, hydrogen affinities of adsorbed O_2 (HA_{O2}) was calculated as Eq. 2.

$$HA_{O2} = \left[E(AuHOO) - \left(E(AuO_2) + E(H)\right)\right] \ \ldots \ (2)$$

Where, E(AuHOO) and Au(AuO_2) are potential energies of adsorption structures of HOO species and O_2 on the Au_{20} model, respectively. E(H) is potential energy of isolated hydrogen atom. HA_{O2} of the Au_{20}^{1-} model and Au_{20}^{2-} model were calculated as -75.3 kcal/mol and -86.9 kcal/mol, respectively. This result clearly indicated that interaction between hydrogen atom and adsorbed O_2 on the Au_{20}^{2-} model is stronger than that on the Au_{20}^{1-} model by 11.6 kcal/mol. This result could be explained by the difference of the degree of O_2 activation on each model as shown in above. Therefore, it was suggested that this is one of the reason for lower activation

energy of the indirect pathway on the Au_{20}^{2-} model compared with that on the Au_{20}^{1-} model. In addition, hydrogen affinity of gas phase (isolated) O_2 molecule and O_2^- anion were calculated as -53.8 kcal/mol and -61.0 kcal/mol, respectively. These values are weaker than those of adsorbed O_2 on negatively charged Au_{20} models. Therefore, it was suggested that adsorbed O_2 on the negatively charged Au cluster is well activated for hydrogen abstraction than gas-phase superoxide anion.

From these results, it was suggested that O_2 on the negatively charged Au cluster is well activated due to the charge transfer from Au to O_2. In addition, the degree of O_2 activation on the Au_{20}^{2-} model is larger than that on the Au_{20}^{1-} model due to the difference of HOMO level of each Au_{20} model. Furthermore, hydrogen affinity of O_2 on the negatively charged Au cluster is larger than that of gas-phase O_2^- anion.

3.4 C-H bond Activation at the 2nd Step of the Reaction

As shown in former sections, it was suggested that the indirect α_C-H bond activation by adsorbed O_2 is the main reaction pathway at the 1st step of the reaction. In this section, β_C-H bond activation pathways at the 2nd step of the reaction were investigated. As shown in Scheme 3, there are four possible β_C-H bond activation pathways from the product state of the indirect α_C-H bond activation pathway; direct pathway, HOOH generation pathway, H_2O generation pathway and OH generation pathway. In the direct pathway, β_C-H bond is directly activated by Au atoms. In the HOOH generation pathway, β_C-H bond is activated by adsorbed HOO species generated by the indirect α_C-H bond activation at the 1st step of the reaction. In the H_2O generation pathway and the OH generation pathway, β_C-H bond is activated by adsorbed OH species or O atom generated by O-O bond cleavage of HOO species, respectively. In this section, these reaction pathways were investigated by using the Au_{20}^{1-} model and Au_{20}^{2-} model. As

shown in below, it was suggested that the OH generation pathway is the main reaction pathway at the 2nd step of the reaction.

Scheme 3. Four possible reaction pathways at the 2nd step of the reaction.

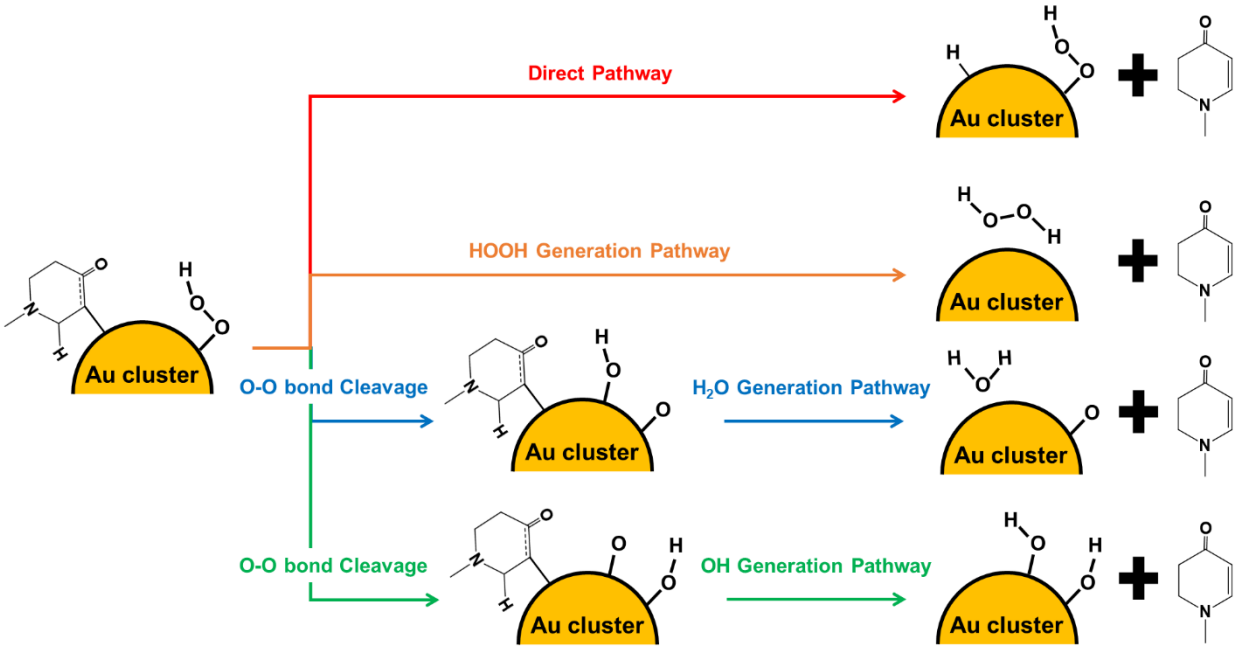

3.4.1 β_C-H bond Activation at the 2nd Step of the Reaction on the Au_{20}^{1-} Model

Potential energy diagram of reaction pathways at the 2nd step of the reaction on the Au_{20}^{1-} model was shown in Figure 16, and optimized conformations of each reaction pathway were also shown in Figure 17. In the direct pathway and the HOOH generation pathway, conformation change from B4 (product state of the 1st step of the reaction) to reactive conformations (Figure 17: B7 and B9, respectively) occurred before β_C-H bond activation. These conformations are unstable than B4 by 10.7 kcal/mol and 7.2 kcal/mol, respectively. These conformation changes are required for the interaction between β_C-H bond and Au atoms or HOO species. In this model, we could not find other sable reactant conformations which are connected to lower

transition states than those in Figure 16. On the other hand, in the H_2O generation pathway and the OH generation pathway, conformation change from B4 to more stable conformations (Figure 17: B11 and B14, respectively) occurred before O-O bond cleavage of HOO species. These conformations are more stable than B4 by 3.2 kcal/mol and 3.0 kcal/mol, respectively. In the OH generation pathway, activation energy for O-O bond cleavage (Figure 16: E_{aB9}) is higher than that for C-H bond activation (Figure 16: E_{aB10}) by 3.8 kcal/mol. On the other hand, activation energy for O-O bond cleavage (Figure 16: E_{aB7}) is lower than that for C-H bond activation (Figure 16: E_{aB8}) by 8.2 kcal/mol in the H_2O generation pathway. In addition, the highest activation energy of the OH generation pathway (E_{aB9} = 15.6 kcal/mol) is lower than that of the H_2O generation pathway (E_{aB8} = 24.9 kcal/mol) by 9.3 kcal/mol. Although activation energy for C-H bond activation in the HOOH generation pathway (E_{aB6} = 14.3 kcal/mol) is lower than the highest activation energy of the OH generation pathway (E_{aB9} = 15.6 kcal/mol) by 1.3 kcal/mol, reactant state of the HOOH generation pathway (B9) is unstable than that of the OH generation pathway (B14) by 10.2 kcal/mol. Furthermore, activation energy for C-H bond activation of the direct pathway (E_{aB5} = 23.6) is higher than the highest activation energy of the OH generation pathway (E_{aB9} = 15.6 kcal/mol) by 8.0 kcal/mol, and reactant state of the direct pathway (B7) is also unstable than that of the OH generation pathway (B14) by 13.7 kcal/mol. From these results, it was suggested that the OH generation pathway is the main reaction pathway of the 2nd step of the reaction on the Au_{20}^{1-} model. In addition, the highest activation energy of the OH generation pathway (E_{aB9} = 15.6 kcal/mol) is lower than that of the 1st reaction step (E_{aB2} = 29.8 kcal/mol) by 14.2 kcal/mol. Therefore, the rate determining step of the total reaction on the Au_{20}^{1-} model is α_C-H bond activation by adsorbed O_2 at the 1st step of the reaction.

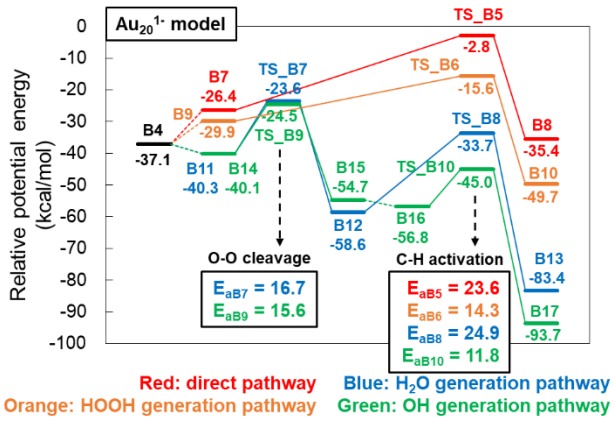

Figure 16. Potential energy diagram of β_C-H bond activation at the 2nd step of the reaction on the Au_{20}^{1-} model. Red line: direct pathway, orange line: HOOH generation pathway, blue line: H_2O generation pathway, green line: OH generation pathway. Reference point of relative potential energies is defined as the sum of the energies of the isolated species: Au_{20}^{1-}, O_2, and 1-methyl-4-piperidone.

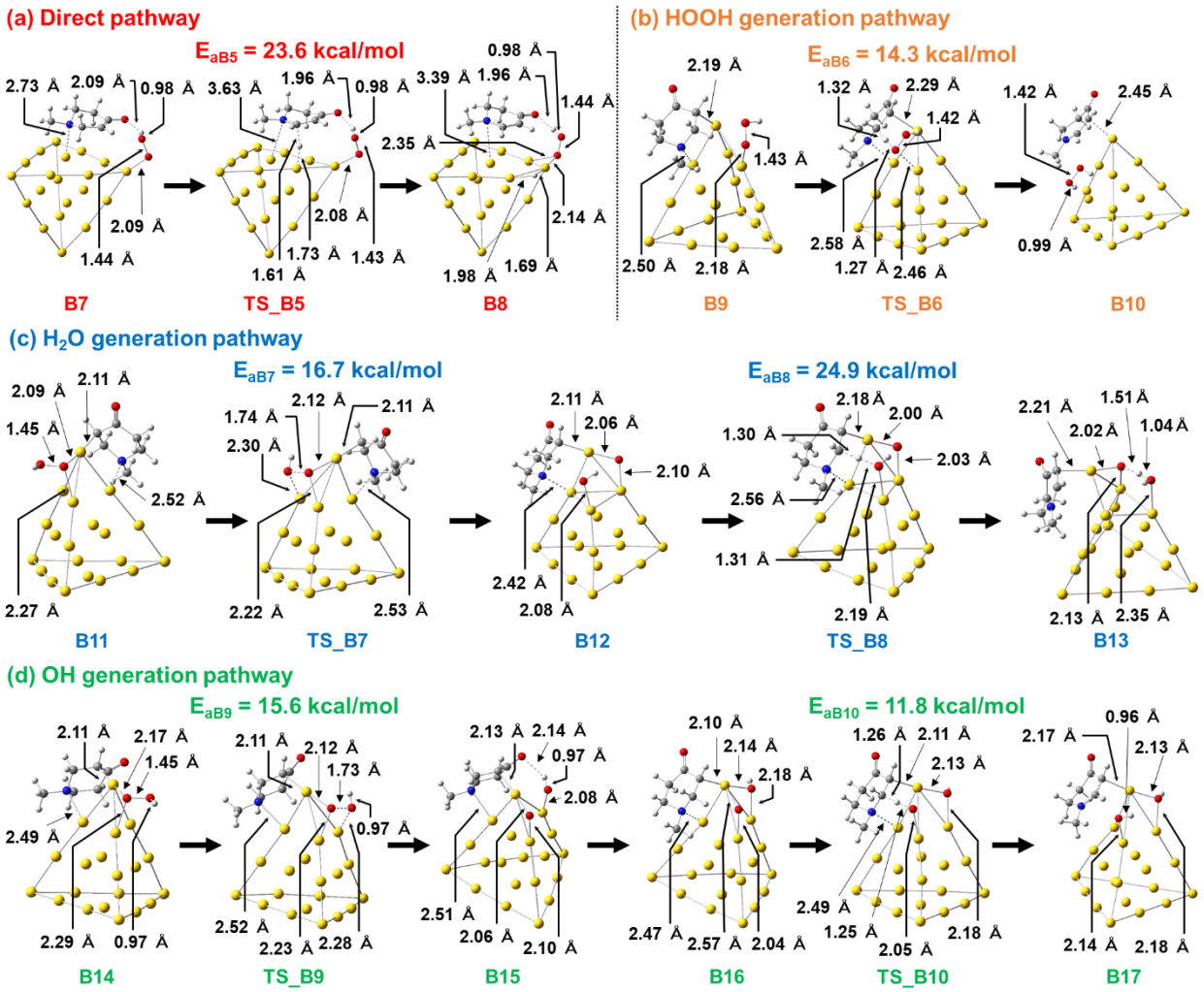

Figure 17. Optimized structures of the reactant, product and transition states of reaction pathways at the 2nd step of the reaction on the Au_{20}^{1-} model. Red ball: oxygen, blue ball: nitrogen, gray ball: carbon, white ball: hydrogen, yellow ball: gold.

3.4.2 β_C-H bond Activation at the 2nd Step of the Reaction on the Au_{20}^{2-} Model

Potential energy diagram of reaction pathways at the 2nd step of the reaction on the Au_{20}^{2-} model was shown in Figure 18, and optimized conformations of each reaction pathway were also shown in Figure 19. On the Au_{20}^{2-} model, conformation change from C4 to more stable conformations (Figure 19: C9, C11, C13 and C16) occurred in all reaction pathways. In both the

H_2O generation pathway and the OH generation pathway, activation energies for O-O bond cleavage (Figure 18: E_{aC7} and E_{aC9}, respectively) are lower than those for C-H bond activation (Figure 18: E_{aC8} and E_{aC10}, respectively) by 13.0 kcal/mol and 6.3 kcal/mol, respectively. In addition, activation energy for C-H bond activation of the OH generation pathway (E_{aC10} = 30.8 kcal/mol) is lower than that of the H_2O generation pathway (E_{aC8} = 37.0 kcal/mol) by 6.2 kcal/mol. Although activation energies for C-H bond activation of the direct pathway (E_{aC5} = 19.4 kcal/mol) and the HOOH generation pathway (E_{aC6} = 29.0 kcal/mol) are lower than that of the OH generation pathway (E_{aC10} = 30.8 kcal/mol) by 11.4 kcal/mol and 1.8 kcal/mol, respectively, reactant states of the direct pathway (C9) and the HOOH generation pathway (C11) are unstable than that of the OH generation pathway (C16) by 11.1 kcal/mol and 4.8 kcal/mol, respectively. From these results, it was suggested that the OH generation pathway is the main reaction pathway at the 2nd step of the reaction on the Au_{20}^{2-} model. In addition, activation energy for C-H bond activation of the OH generation pathway (E_{aC10} = 30.8 kcal/mol) is higher than that of α_C-H bond activation at the 1st step of the reaction (E_{aC2} = 11.8 kcal/mol) by 19.0 kcal/mol. Therefore, the rate determining step of the total reaction on the Au_{20}^{2-} model is β_C-H bond activation by OH species at the 2nd step of the reaction. Therefore, rate determining step is different between the Au_{20}^{1-} model and Au_{20}^{2-} model, and activation energy of the rate determining step (29.8 kcal/mol in the Au_{20}^{1-} model, 30.8 kcal/mol in the Au_{20}^{2-} model) is almost same in each model.

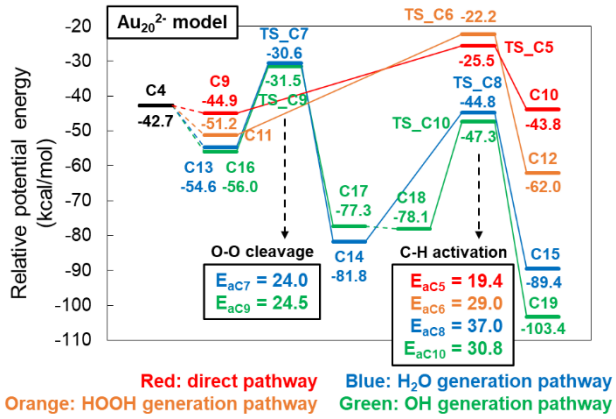

Figure 18. Potential energy diagram of β_C-H bond activation at the 2nd step of the reaction on the Au_{20}^{2-} model. Red line: direct pathway, orange line: HOOH generation pathway, blue line: H_2O generation pathway, green line: OH generation pathway. Reference point of relative potential energies is defined as the sum of the energies of the isolated species: Au_{20}^{2-}, O_2, and 1-methyl-4-piperidone.

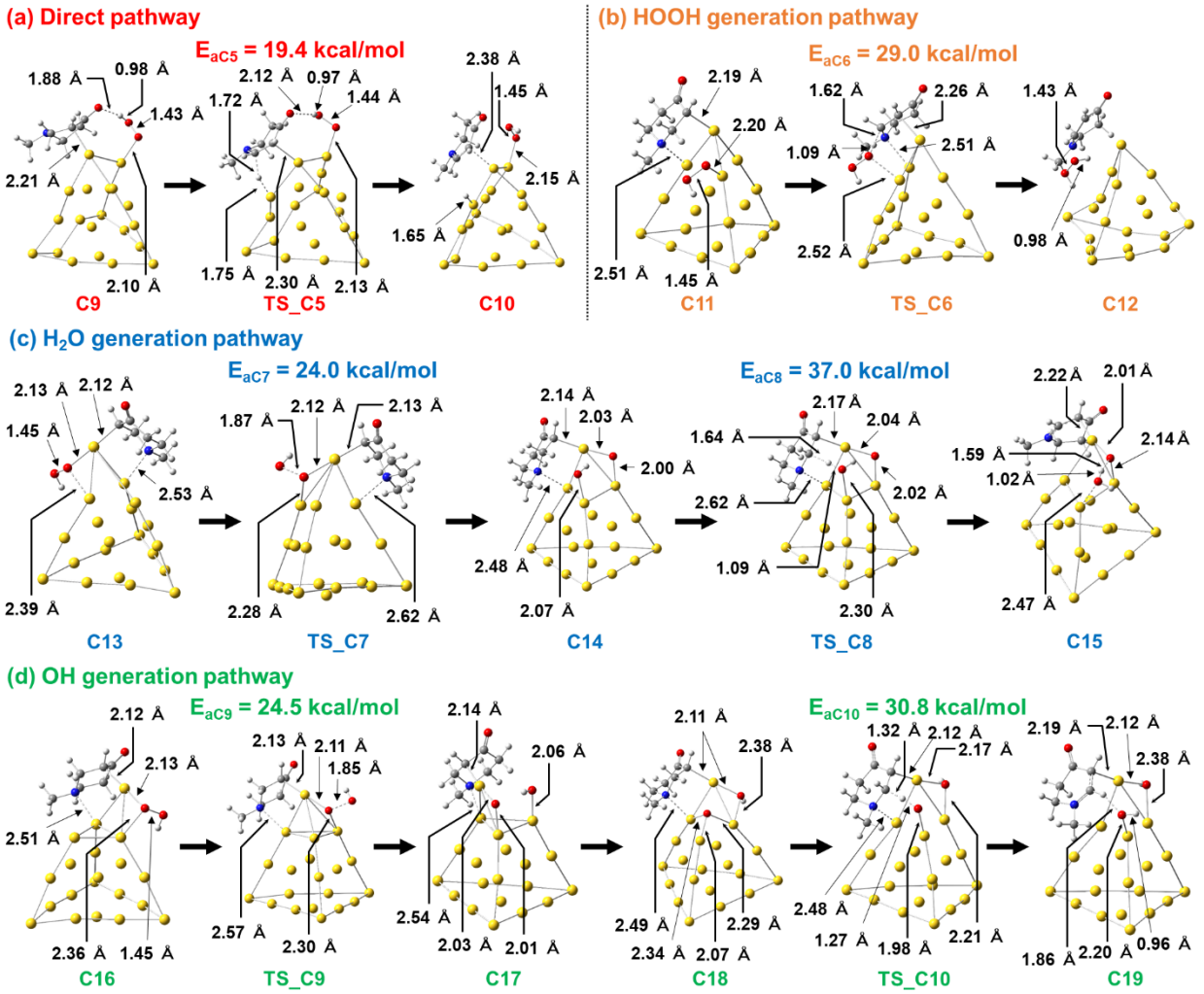

Figure 19. Optimized structures of the reactant, product and transition states of reaction pathways at the 2nd step of the reaction on the Au_{20}^{2-} model. Red ball: oxygen, blue ball: nitrogen, gray ball: carbon, white ball: hydrogen, yellow ball: gold.

3.5 Charge Analysis for the 2nd Step of the Reaction

In this section, the effect of charge state of Au cluster for each reaction pathway at the 2nd step of the reaction was investigated based on natural population analysis (NPA). First, O-O bond cleavage of HOO species was analyzed. As shown in Figure 17, two oxygen atoms of HOO

species both interact with Au atoms at transition states of O-O bond cleavage on the Au_{20}^{1-} model (TS_B7 and TS_B9). On the other hand, OH group of HOO does not interact with Au at transition states of O-O bond cleavage on the Au_{20}^{2-} model (Figure 19: TS_C7 and TS_C9). Therefore, it was suggested that these unstable conformations of transition states on the Au_{20}^{2-} model induce higher activation energies for O-O bond cleavage (E_{aC7} = 24.0 kcal/mol and E_{aC9} = 24.5 kcal/mol) compared with those on the Au_{20}^{1-} model (E_{aB7} = 16.7 kcal/mol and E_{aB9} = 15.6 kcal/mol). NPA charge of Au_{20} cluster at B11 and B14 (reactant state of O-O bond cleavage in the Au_{20}^{1-} model) were -0.23 and -0.24, respectively. On the other hand, these were calculated as -1.14 (at C13 (*cf.* Figure 19)) and -1.15 (at C16) in the Au_{20}^{2-} model. Therefore, it was suggested that negative charge on oxygen atom of OH group avoids interaction with large negative charge on Au in the Au_{20}^{2-} model. Actually, interaction between OH group and Au at the transition state of O-O bond cleavage could not find in the Au_{20}^{2-} model even if transition state structure in the Au_{20}^{1-} model was used as initial structure for transition state optimization.

Next, β_C-H bond activation at the OH generation pathway was analyzed. At the reactant state of β_C-H bond cleavage on each model (i.e. B16 and C18), NPA charge of intermediated molecule ($C_6H_{10}NO$) was calculated as -0.20 and -0.33, respectively. On the other hand, NPA charge of product molecule (C_6H_9NO) at the product state on each model (i.e. B17 and C19) was calculated as +0.31 and +0.26, respectively. In addition, β_hydrogen is activated as proton in the OH generation pathway. Therefore, negative charge is moved from intermediate molecule to Au cluster during the reaction. Actually, NPA charge of Au_{20} cluster becomes more negative as the reaction proceeds in both models. Comparing NPA charge of the Au_{20} cluster at the reactant state, it was calculated as +0.31 in the Au_{20}^{1-} model (i.e. at B16) while that in the Au_{20}^{2-} model was calculated as -0.20 (i.e. at C18). Therefore, it was suggested that charge transfer from the

intermediate molecule to the Au_{20} cluster proceeds easily in the Au_{20}^{1-} model compared with that in the Au_{20}^{2-} model due to the difference of charge state of the Au_{20} cluster at the reactant state. The tendency of charge state is almost same with this mechanism in the H_2O generation pathway and the HOOH generation pathway in which β_hydrogen is activated as proton. Actually, activation energies of these pathways in the Au_{20}^{1-} model (E_{aB10} = 11.8 kcal/mol, E_{aB8} = 24.9 kcal/mol and E_{aB6} = 14.3 kcal/mol, respectively) are lower than those in the Au_{20}^{2-} model (E_{aC10} = 30.8 kcal/mol, E_{aC8} = 37.0 kcal/mol and E_{aC6} = 29.0 kcal/mol, respectively).

Finally, β_C-H bond activation in the direct pathway was analyzed. NPA charge of β_hydrogen atom at the transition state of the direct pathway was calculated as +0.02 in the Au_{20}^{1-} model (i.e. at TS_B5) and -0.19 in the Au_{20}^{2-} model (i.e. at TS_C5), respectively. On the other hand, NPA charge of β_hydrogen at the transition state of other reaction pathways were more than +0.35 in both models. From this result, it was suggested that β_hydrogen is not activated as proton in the direct pathway. In the Au_{20}^{2-} model, the intermediate molecule at the reactant state is negatively charged (NPA charge = -0.45), and the product molecule is positively charged at the product state (NPA charge = +0.19) just like other pathways as shown in above. However, negative charge can move not only from the intermediate molecule but also with β_hydrogen atom to the Au_{20} cluster in the direct pathway. Therefore, it was suggested that charge transfer from the intermediate molecule to the Au_{20} cluster in the direct pathway proceeds more naturally than that in other pathways. Actually, activation energy of the direct pathway (E_{aC5} = 19.4 kcal/mol) is lower than that of other pathways in the Au_{20}^{2-} model while the reactant state of the direct pathway is unstable than that of other pathways. On the other hand, NPA charge of the intermediate molecule at the reactant state is +0.24 in the Au_{20}^{1-} model. In brief, negative charge of the intermediate molecule was already moved to the Au_{20} cluster at the

reactant state of the Au_{20}^{1-} model. In addition, the intermediate molecule is adsorbed on the Au_{20}^{1-} model by Au-N bond while it is adsorbed by Au-C bond in the Au_{20}^{2-} model, and this reactant state (B7 in Figure 17) is unstable than other reactant states (*cf.* Figure 16). Furthermore, the intermediate molecule is almost physisorbed structure at the transition state in the Au_{20}^{1-} model (TS_B5 in Figure 17). In the Au_{20}^{1-} model, we could not find transition state with keeping Au-C bond. From these results, it was investigated that charge state and adsorption structure of the intermediate molecule at the reactant state in the Au_{20}^{1-} model are different from those in the Au_{20}^{2-} model. In addition, the conformation of the transition state in the Au_{20}^{1-} model is unstable than that in the Au_{20}^{2-} model. Actually, activation energy of the direct pathway in the Au_{20}^{1-} model (E_{aB5} = 23.6 kcal/mol) is higher than that in the Au_{20}^{2-} model (E_{aC5} = 19.4 kcal/mol).

From these results, it was suggested that negative charge of the intermediate molecule generated by α-deprotonation of 1-methyl-4-piperidone is moved to the Au cluster during the β_C-H bond activation at the 2nd step of the reaction. Therefore, this reaction is unfavorable on the Au cluster with large negative charge. This is one of the reason why activation energies of the OH generation pathway at the 2nd step of the reaction are higher in the Au_{20}^{2-} model compared with those in the Au_{20}^{1-} model.

4. Conclusions

The Au/OMS-2 catalyst is the efficient heterogeneous catalyst for selective α, β-dehydrogenation of β-N-substituted saturated ketones. In this study, the reaction mechanism of α, β-dehydrogenation of 1-methyl-4-piperidone was investigated by DFT calculations. Whole reaction scheme was shown in Scheme 4.

Scheme 4. Whole reaction scheme for α, β-dehydrogenation of 1-methyl-4-piperidone on the Au/OMS-2 catalyst[a]

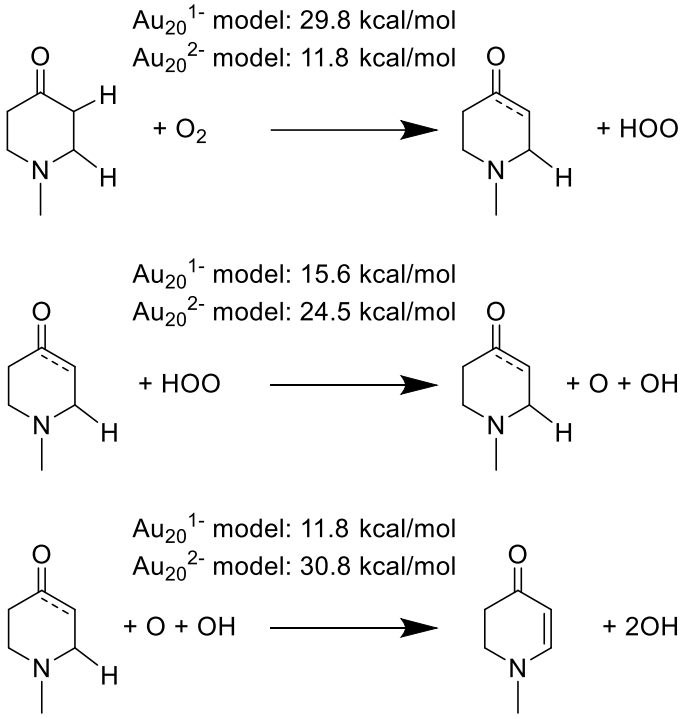

[a]The numbers upper on the arrows are activation energies on the Au_{20}^{1-} model and Au_{20}^{2-} model, respectively.

First, α_C-H bond of 1-methyl-4-piperidone is activated by O_2 adsorbed on the Au cluster. This reaction pathway is more favorable than C-H bond activation by Au surface or β_C-H bond activation. This result supports the experimental result of the Au/C model catalyst (Au catalyst without the effect of lattice oxygen of the OMS-2 support) on which O_2 is essential for the reaction. In addition, it was investigated that Au cluster on the OMS-2 support is negatively charged due to the charge transfer from the OMS-2 support to the Au cluster. Furthermore, O_2 adsorbed on the negatively charged Au cluster is well activated for hydrogen abstraction, and

this is one of the reason why aerobic C-H bond activation proceeds on the Au/OMS-2 catalyst. In particular, the degree of the O_2 activation is increased in more negatively charged Au cluster. According to this trend, activation barrier for the α_C-H bond cleavage by adsorbed O_2 is lower in more negatively charged Au cluster.

Finally, remaining β_C-H bond is activated by adsorbed O atom generated by O-O bond cleavage of adsorbed HOO species. This reaction pathway is more favorable than other possible pathways; β_C-H bond activation by Au surface, HOO species or OH species. Because the product molecule is neutral molecule, negative charge of the intermediated molecule generated by α-deprotonation of 1-methyl-4-piperidone at the 1st reaction step is moved to the Au cluster during this reaction. Therefore, activation barrier for this reaction step is higher in more negatively charged Au cluster. From these results, the rate-determining step of the total reaction is 1st α_C-H bond activation step in the Au_{20}^{1-} model. On the other hand, the rate-determining step of the total reaction is 2nd β_C-H bond activation step in the Au_{20}^{2-} model.

REFERENCES

1. Negri, G.; Kascheres, C.; Kascheres, A. J., Recent development in preparation reactivity and biological activity of enaminoketones and enaminothiones and their utilization to prepare heterocyclic compounds. *J. Heterocycl. Chem.* **2004,** *41* (4), 461-491.
2. Elassar, A. Z. A.; El-Khair, A. A., Recent developments in the chemistry of enaminones. *Tetrahedron* **2003,** *59* (43), 8463-8480.
3. Chattopadhyay, A. K.; Hanessian, S., Cyclic enaminones. Part I: stereocontrolled synthesis using diastereoselective and catalytic asymmetric methods. *Chem. Commun.* **2015,** *51* (92), 16437-16449.
4. Chattopadhyay, A. K.; Hanessian, S., Cyclic enaminones. Part II: applications as versatile intermediates in alkaloid synthesis. *Chem. Commun.* **2015,** *51* (92), 16450-16467.
5. Izawa, Y.; Pun, D.; Stahl, S. S., Palladium-Catalyzed Aerobic Dehydrogenation of Substituted Cyclohexanones to Phenols. *Science* **2011,** *333* (6039), 209-213.
6. Diao, T. N.; Stahl, S. S., Synthesis of Cyclic Enones via Direct Palladium-Catalyzed Aerobic Dehydrogenation of Ketones. *J. Am. Chem. Soc.* **2011,** *133* (37), 14566-14569.

7. Diao, T. N.; Wadzinski, T. J.; Stahl, S. S., Direct aerobic alpha,beta-dehydrogenation of aldehydes and ketones with a Pd (TFA)(2)/4,5-diazafluorenone catalyst. *Chem. Sci.* **2012,** *3* (3), 887-891.
8. Pun, D.; Diao, T. N.; Stahl, S. S., Aerobic Dehydrogenation of Cyclohexanone to Phenol Catalyzed by Pd(TFA)(2)/2-Dimethylaminopyridine: Evidence for the Role of Pd Nanoparticles. *J. Am. Chem. Soc.* **2013,** *135* (22), 8213-8221.
9. Izawa, Y.; Zheng, C. W.; Stahl, S. S., Aerobic Oxidative Heck/Dehydrogenation Reactions of Cyclohexenones: Efficient Access to meta-Substituted Phenols. *Angew. Chem. Int. Ed.* **2013,** *52* (13), 3672-3675.
10. Diao, T. N.; Pun, D.; Stahl, S. S., Aerobic Dehydrogenation of Cyclohexanone to Cyclohexenone Catalyzed by Pd(DMSO)(2)(TFA)(2): Evidence for Ligand-Controlled Chemoselectivity. *J. Am. Chem. Soc.* **2013,** *135* (22), 8205-8212.
11. Gao, W. M.; He, Z. Q.; Qian, Y.; Zhao, J.; Huang, Y., General palladium-catalyzed aerobic dehydrogenation to generate double bonds. *Chem. Sci.* **2012,** *3* (3), 883-886.
12. Zhang, X. W.; Wang, D. Y.; Emge, T. J.; Goldman, A. S., Dehydrogenation of ketones by pincer-ligated iridium: Formation and reactivity of novel enone complexes. *Inorg. Chim. Acta* **2011,** *369* (1), 253-259.
13. Kusumoto, S.; Akiyama, M.; Nozaki, K., Acceptor less Dehydrogenation of C-C Single Bonds Adjacent to Functional Groups by Metal-Ligand Cooperation. *J. Am. Chem. Soc.* **2013,** *135* (50), 18726-18729.
14. Zhang, Z. Z.; Hashiguchi, T.; Ishida, T.; Hamasaki, A.; Honma, T.; Ohashi, H.; Yokoyama, T.; Tokunaga, M., Aerobic oxidation of cyclohexanones to phenols and aryl ethers over supported Pd catalysts. *Organic Chemistry Frontiers* **2015,** *2* (6), 654-660.
15. Jin, X. J.; Taniguchi, K.; Yamaguchi, K.; Mizuno, N., Au-Pd alloy nanoparticles supported on layered double hydroxide for heterogeneously catalyzed aerobic oxidative dehydrogenation of cyclohexanols and cyclohexanones to phenols. *Chem. Sci.* **2016,** *7* (8), 5371-5383.
16. Yoshii, D.; Jin, X. J.; Yatabe, T.; Hasegawa, J.; Yamaguchi, K.; Mizuno, N., Gold nanoparticles on OMS-2 for heterogeneously catalyzed aerobic oxidative alpha, beta-dehydrogenation of beta-heteroatom-substituted ketones. *Chem. Commun.* **2016,** *52* (99), 14314-14317.
17. Boronat, M.; Combita, D.; Concepcion, P.; Corma, A.; Garcia, H.; Juarez, R.; Laursen, S.; Lopez-Castro, J. D., Making C-C Bonds with Gold: Identification of Selective Gold Sites for Homo- and Cross-Coupling Reactions between Iodobenzene and Alkynes. *J. Phys. Chem. C* **2012,** *116* (47), 24855-24867.
18. Bobuatong, K.; Karanjit, S.; Fukuda, R.; Ehara, M.; Sakurai, H., Aerobic oxidation of methanol to formic acid on Au-20(-): a theoretical study on the reaction mechanism. *Phys. Chem. Chem. Phys.* **2012,** *14* (9), 3103-3111.
19. Ato, Y.; Hayashi, A.; Koga, H.; Kawakami, T.; Yamanaka, S.; Okumura, M., Theoretical study of aerobic oxidation of alcohols over Au-38 nanocluster by a two-step-modeling approach. *Chem. Phys. Lett.* **2019,** *724*, 115-121.
20. Shang, C.; Liu, Z. P., Origin and Activity of Gold Nanoparticles as Aerobic Oxidation Catalysts in Aqueous Solution. *J. Am. Chem. Soc.* **2011,** *133* (25), 9938-9947.
21. Chang, C. R.; Huang, Z. Q.; Li, J., Hydrogenation of molecular oxygen to hydroperoxyl: An alternative pathway for O-2 activation on nanogold catalysts. *Nano Research* **2015,** *8* (11), 3737-3748.

22. Okumura, M.; Kitagawa, Y.; Kawakami, T.; Haruta, M., Theoretical investigation of the hetero-junction effect in PVP-stabilized Au-13 clusters. The role of PVP in their catalytic activities. *Chem. Phys. Lett.* **2008,** *459* (1-6), 133-136.
23. Sakata, K.; Ato, Y.; Tada, K.; Koga, H.; Yamanaka, S.; Kawakami, T.; Saito, T.; Okumura, M., Theoretical Investigation for Heterojunction Effects in Polymer-stabilized Au Nanocluster Catalysis: Difference in Catalytic Activity between Au:PVP and Au:PAA. *Chem. Lett.* **2016,** *45* (3), 344-346.
24. Engel, J.; Francis, S.; Roldan, A., The influence of support materials on the structural and electronic properties of gold nanoparticles - a DFT study. *Phys. Chem. Chem. Phys.* **2019,** *21* (35), 19011-19025.
25. Freund, H. J.; Pacchioni, G., Oxide ultra-thin films on metals: new materials for the design of supported metal catalysts. *Chem. Soc. Rev.* **2008,** *37* (10), 2224-2242.
26. Pacchioni, G.; Freund, H. J., Controlling the charge state of supported nanoparticles in catalysis: lessons from model systems. *Chem. Soc. Rev.* **2018,** *47* (22), 8474-8502.
27. Boronat, M.; Concepcion, P.; Corma, A., Unravelling the Nature of Gold Surface Sites by Combining IR Spectroscopy and DFT Calculations. Implications in Catalysis. *J. Phys. Chem. C* **2009,** *113* (38), 16772-16784.
28. Tang, D. Y.; Hu, C. W., DFT Insight into CO Oxidation Catalyzed by Gold Nanoclusters: Charge Effect and Multi-State Reactivity. *Journal of Physical Chemistry Letters* **2011,** *2* (23), 2972-2977.
29. Yoon, B.; Hakkinen, H.; Landman, U.; Worz, A. S.; Antonietti, J. M.; Abbet, S.; Judai, K.; Heiz, U., Charging effects on bonding and catalyzed oxidation of CO on Au-8 clusters on MgO. *Science* **2005,** *307* (5708), 403-407.
30. Roldan, A.; Ricart, J. M.; Illas, F.; Pacchioni, G., O-2 adsorption and dissociation on neutral, positively and negatively charged Au-n (n=5-79) clusters. *Phys. Chem. Chem. Phys.* **2010,** *12* (36), 10723-10729.
31. Gao, M.; Horita, D.; Ono, Y.; Lyalin, A.; Maeda, S.; Taketsugu, T., Isomerization in Gold Clusters upon O-2 Adsorption. *J. Phys. Chem. C* **2017,** *121* (5), 2661-2668.
32. Yoon, B.; Hakkinen, H.; Landman, U., Interaction of O-2 with gold clusters: Molecular and dissociative adsorption. *J. Phys. Chem. A* **2003,** *107* (20), 4066-4071.
33. Okumura, M.; Kitagawa, Y.; Haruta, M.; Yamaguchi, K., DFT studies of interaction between O-2 and Au clusters. The role of anionic surface Au atoms on Au clusters for catalyzed oxygenation. *Chem. Phys. Lett.* **2001,** *346* (1-2), 163-168.
34. Tompsett, D. A.; Parker, S. C.; Islam, M. S., Surface properties of alpha-MnO2: relevance to catalytic and supercapacitor behaviour. *J. Mater. Chem. A* **2014,** *2* (37), 15509-15518.
35. Gao, T.; Glerup, M.; Krumeich, F.; Nesper, R.; Fjellvag, H.; Norby, P., Microstructures and spectroscopic properties of cryptomelane-type manganese dioxide nanofibers. *J. Phys. Chem. C* **2008,** *112* (34), 13134-13140.
36. Blum, V.; Gehrke, R.; Hanke, F.; Havu, P.; Havu, V.; Ren, X. G.; Reuter, K.; Scheffler, M., Ab initio molecular simulations with numeric atom-centered orbitals. *Comput. Phys. Commun.* **2009,** *180* (11), 2175-2196.
37. Perdew, J. P.; Burke, K.; Ernzerhof, M., Generalized gradient approximation made simple. *Phys. Rev. Lett.* **1996,** *77* (18), 3865-3868.
38. Cockayne, E.; Li, L., First-principles DFT+U studies of the atomic, electronic, and magnetic structure of alpha-MnO2 (cryptomelane). *Chem. Phys. Lett.* **2012,** *544*, 53-58.

39. Li, J.; Li, X.; Zhai, H. J.; Wang, L. S., Au-20: A tetrahedral cluster. *Science* **2003,** *299* (5608), 864-867.
40. M. J. Frisch, G. W. T., H. B. Schlegel, G. E. Scuseria, M. A. Robb, J. R. Cheeseman, G. Scalmani, V. Barone, G. A. Petersson, H. Nakatsuji, X. Li, M. Caricato, A. Marenich, J. Bloino, B. G. Janesko, R. Gomperts, B. Mennucci, H. P. Hratchian, J. V. Ortiz, A. F. Izmaylov, J. L. Sonnenberg, D. Williams-Young, F. Ding, F. Lipparini, F. Egidi, J. Goings, B. Peng, A. Petrone, T. Henderson, D. Ranasinghe, V. G. Zakrzewski, J. Gao, N. Rega, G. Zheng, W. Liang, M. Hada, M. Ehara, K. Toyota, R. Fukuda, J. Hasegawa, M. Ishida, T. Nakajima, Y. Honda, O. Kitao, H. Nakai, T. Vreven, K. Throssell, J. A. Montgomery, Jr., J. E. Peralta, F. Ogliaro, M. Bearpark, J. J. Heyd, E. Brothers, K. N. Kudin, V. N. Staroverov, T. Keith, R. Kobayashi, J. Normand, K. Raghavachari, A. Rendell, J. C. Burant, S. S. Iyengar, J. Tomasi, M. Cossi, J. M. Millam, M. Klene, C. Adamo, R. Cammi, J. W. Ochterski, R. L. Martin, K. Morokuma, O. Farkas, J. B. Foresman, and D. J. Fox, *Gaussian 09, revision B.01* **2016,** *Gaussian, Inc., Wallingford, CT*.
41. Zhao, Y.; Truhlar, D. G., The M06 suite of density functionals for main group thermochemistry, thermochemical kinetics, noncovalent interactions, excited states, and transition elements: two new functionals and systematic testing of four M06-class functionals and 12 other functionals. *Theor. Chem. Acc.* **2008,** *120* (1-3), 215-241.
42. Andrae, D.; Haussermann, U.; Dolg, M.; Stoll, H.; Preuss, H., Energy-adjusted abinitio pseudopotentials for the 2nd and 3rd row transition-elements. *Theoret. Chim. Acta* **1990,** *77* (2), 123-141.
43. Hehre, W. J.; Ditchfield, R.; Pople, J. A., Self-consistent molecular-orbital methods .12. Further extensions of gaussian-type basis sets for use in molecular-orbital studies of organic-molecules. *J. Chem. Phys.* **1972,** *56* (5), 2257-2261.
44. Hirshfeld, F. L., Bonded-Atom Fragments for Describing Molecular Charge-Densities. *Theoret. Chim. Acta* **1977,** *44* (2), 129-138.
45. Green, I. X.; Tang, W. J.; Neurock, M.; Yates, J. T., Spectroscopic Observation of Dual Catalytic Sites During Oxidation of CO on a Au/TiO2 Catalyst. *Science* **2011,** *333* (6043), 736-739.
46. Liu, L. C.; Corma, A., Metal Catalysts for Heterogeneous Catalysis: From Single Atoms to Nanoclusters and Nanoparticles. *Chem. Rev.* **2018,** *118* (10), 4981-5079.
47. Ishida, T.; Koga, H.; Okumura, M.; Haruta, M., Advances in Gold Catalysis and Understanding the Catalytic Mechanism. *Chemical Record* **2016,** *16* (5), 2278-2293.
48. Liu, Z. P.; Hu, P.; Alavi, A., Catalytic role of gold in gold-based catalysts: A density functional theory study on the CO oxidation on gold. *J. Am. Chem. Soc.* **2002,** *124* (49), 14770-14779.
49. Koga, H.; Tada, K.; Okumura, M., DFT study of CO oxidation over Au/TiO2(110): The extent of the reactive perimeter zone. *Chem. Phys. Lett.* **2014,** *610*, 76-81.

Chapter 5

Theoretical Study for C-H bond Activation on Pd Cluster: Agostic Interaction on Pd Cluster Induced by OAc Ligands

1. Introduction

1, 4-palladium migration reaction through aromatic C-H bond activation is one of the efficient way for fused polycycles compounds synthesis[1-7]. Recently, a novel 1,7-palladium migration reaction by homogeneous Pd complex catalyst for N1-substituted benzotriazole synthesis was reported by Ren et al[8]. N1-substituted benzotriazole is payed attention as the important compound for cancer treatment[9]. Reaction mechanism for 1-(4-cyanophenyl)benzotriazole (**2b**) synthesis from 1-(2-bromo-4-cyanophenyl)-3-methyl-3-phenyltriazene (**1b**) proposed by Ren et al.[8] was shown in Scheme 1. Although C(sp^2)-H bonds activation by Pd nanoparticle catalysts were reported[10], N1-substituted benzotriazole synthesis via the 1,7-palladium migration reaction by heterogeneous Pd catalytic system was not reported until the development of a sulfur-modified Au-supported Pd material (SAPd) catalyst[11]. In the SAPd catalyst, immobilized Pd nanoparticles act as efficient heterogeneous catalyst[12-17].

Scheme 1. Reaction mechanism for N1-subsituted benzotriazole synthesis via 1, 7-palladium migration reaction by homogeneous Pd complex catalyst[a] by Ren et al.[8]

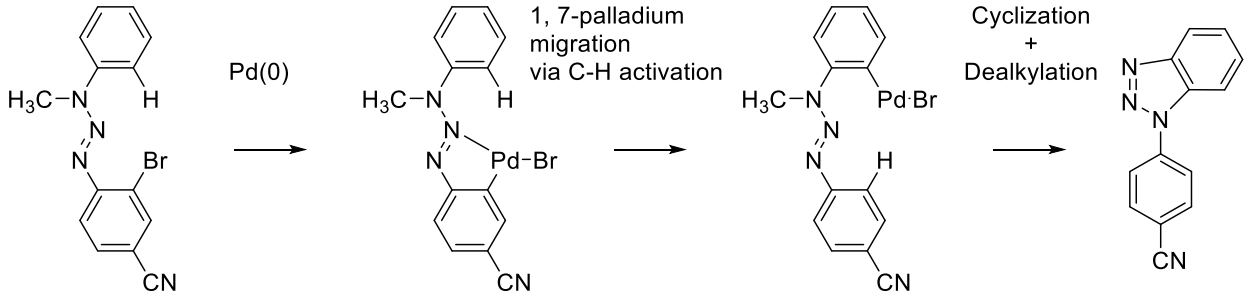

[a]Ligands of the Pd complex catalyst are omitted in this scheme.

One of the important reaction step of the 1, 7-palladium migration reaction is aromatic C-H bond activation by the Pd catalyst. It was suggested that this reaction step proceeds with a five-membered palladacycle intermediate[8, 11] which was also pointed out as the intermediate of 1, 4-palladium migration reactions[18-21]. However, detail of aromatic C-H bond activation mechanism of the 1, 7-palladium migration reaction on the Pd catalyst is not fully understood. Especially, aromatic C-H bond activation on the heterogeneous Pd nanoparticle catalyst is particularly interesting. In addition, the 1, 7-palladium migration reaction does not proceed on the SAPd catalyst without $PhI(OAc)_2$ oxidant[11]. Therefore, effect of OAc ligands to the reaction is also interesting. There are several theoretical studies for aromatic C-H bond activation by homogeneous Pd catalysts with OAc ligands[22-36]. However, theoretical study for the aromatic C-H bond activation on the heterogeneous Pd cluster catalyst was not reported in the best of our knowledge although theoretical study for $C(sp^3)$-H bond activation on Pd cluster catalysts were reported[37-40]. Furthermore, the effect of OAc ligand for the C-H bond activation on the heterogeneous Pd cluster catalyst is not clear. Therefore, the aromatic C-H bond activation mechanism of the 1, 7-palladium migration reaction on the SAPd catalyst was investigated by density functional theory (DFT) calculations in this study. In particular, we focused on the effect of OAc ligands for the C-H bond activation.

This chapter is organized as follows. In the next section, computational models and the detail for DFT calculations are discussed. In Subsection 3.1-3.2, C-H bond activation pathways on the Pd cluster w/ or w/o OAc ligand are discussed. In Subsection 3.3, electronic effect of OAc ligand for the C-H bond activation is analyzed by using molecular orbital analysis. A concluding remark is given in Section 4.

2. Computational Details

2.1 Computational Models

To investigate the C-H bond activation mechanism and the effect of OAc ligands on the SAPd catalyst, several computational models were constructed (Figure 1). In present study, simple model systems were adopted to give the simple sight for the complex catalytic systems. In addition, 1-(2-bromo)-3-methyl-3-phenyltriazene (**1a** in Figure 1a) was used as a reactant molecule in our calculation. 1, 7-palladium migration reaction for this reactant molecule also experimentally proceeds both in the homogeneous Pd complex catalyst[8] and the SAPd catalyst[11].

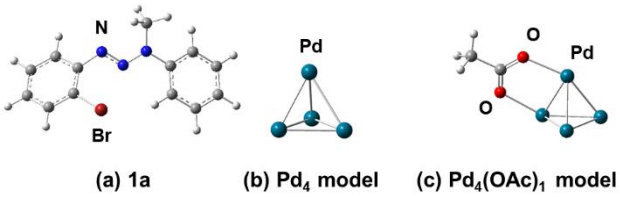

Figure 1. Computational models. (a) 1-(2-bromo)-3-methyl-3-phenyltriazene (**1a**), (b) Pd_4 model, (c) $Pd_4(OAc)_1$ model. White: hydrogen, gray: carbon, blue: nitrogen, dark red: bromide, blue green: palladium, red: oxygen.

2.1.1 Pd_4 Model

Pd_4 model constructed by four Pd atoms was adopted for a computational model of the Pd cluster catalyst in simple form. Because there are two possible conformations in the Pd_4 model; square structure and tetrahedral structure, stability of these conformations in several spin state were investigated. As shown in Table 1, the tetrahedral structure in triplet state is the most stable state in our calculation. Therefore, tetrahedral structure and triplet state were adopted in this study (Figure 1b).

Table 1. Stability of the Pd_4 model in each state

	Tetrahedral structure			Square structure		
	Singlet	Triplet	Quintet	Singlet	Triplet	Quintet
ΔE (kcal/mol)[a]	0.0	-15.4	16.0	0.1	2.2	29.8

[a]Relative potential energy compared with the tetrahedral structure in singlet state.

2.1.2 $Pd_4(OAc)_1$ Model

To investigate the effect of OAc ligand, $Pd_4(OAc)_1$ model was constructed (Figure 1c). An OAc ligand was adsorbed on the Pd_4 model in this model. Because this OAc ligand was come from $PhI(OAc)_2$[11], total charge of the $Pd_4(OAc)_1$ model was calculated as neutral. Quartet state is more stable spin state of the $Pd_4(OAc)_1$ model than doublet state and sextet state by 6.9 kcal/mol and 42.2 kcal/mol, respectively. However, adsorption structures of the reactant molecule (**1a**) on the $Pd_4(OAc)_1$ model in quartet state are unstable those in doublet state in some cases. In addition, transition states and product states of C-H bond activation of **1a** in doublet state are more stable than those in quartet state. Therefore, the $Pd_4(OAc)_1$ model was calculated as doublet state in present study.

2.2 DFT Calculations

Both geometry optimizations and single-point energy calculations were performed using DFT at the B3LYP functional level[41, 42] with the D3 version of Grimme's dispersion function[43]. We employed the Stuttgart/Dresden basis set with effective core potential[44] for Pd atoms. The 6-31+G (d, p) basis sets[45, 46] were used for the other atoms. The polarizable continuum model[47] was adopted to incorporate the solvation effect of *N*,*N-dimethylformamide*. The Ultra Fine Grid (99,590 grid) was used for the integration grid of numerical integration. All reactants, products, and transition state structures were connected by intrinsic reaction coordinate (IRC) calculations.

In addition, normal mode analysis was performed, and we confirmed that each of the equilibrium and transition states contained zero and one imaginary frequency, respectively. All calculations were carried out using the Gaussian 09 program package[48].

In this study, activation energy (E_a) and reaction energy (E_r) are defined by Eq.1 and Eq.2, respectively.

$$E_a = E(TS) - E(R) \quad \ldots (1)$$

$$E_r = E(P) - E(R) \quad \ldots (2)$$

Where, E(TS), E(R) and E(P) are potential energies of transition state, reactant state and product state, respectively.

3. Results and Discussion

In this section, C-H bond activation pathways of **1a** and the effect of OAc ligand were investigated by using the Pd_4 model and $Pd_4(OAc)_1$ model. As discussed in below, activation energy for the C-H bond activation is lower in the $Pd_4(OAc)_1$ model than that in the Pd_4 model due to agostic interaction between C-H bond and Pd cluster in the presence of OAc ligand.

3.1 C-H bond Activation on the Pd(0) Cluster

In this subsection, C-H bond activation pathways of **1a** on the Pd(0) cluster without OAc ligand were investigated by using the Pd_4 model. As shown in Scheme 1, it was expected that C-H bond activation occurs after Ph-Br bond cleavage in the homogeneous catalyst system. In this study, C-H bond activation pathways both before and after Ph-Br bond cleavage were investigated.

First, C-H bond activation pathway at the 1st step of the reaction (i.e. before Ph-Br bond cleavage) was investigated. As shown in Figure 2a, C-H bond of **1a** is activated by the Pd cluster

via five-membered palladacycle intermediate generation (Figure 2a: A2) which was suggested in previous studies[8, 11]. The planer structure of five-membered palladacycle forms conjugated system, and this conformation is more stable than other non-planer conformations. Activation energy and reaction energy for this reaction were calculated as 20.7 kcal/mol and 0.0 kcal/mol, respectively. Next, C-H bond activation pathway at the 2nd step of the reaction (i.e. after Ph-Br bond cleavage) was investigated. As shown in Figure 2b, this reaction also proceeds via five-membered palladacycle intermediate generation (Figure 2b: A4). Activation energy and reaction energy for this reaction were calculated as 29.8 kcal/mol and 8.5 kcal/mol, respectively. Although activation energy for the C-H bond activation at the 1st step of the reaction is lower than that at the 2nd step of the reaction by 9.1 kcal/mol, activation energy and reaction energy for Ph-Br bond cleavage at the 1st step of the reaction was calculated as 3.8 kcal/mol and -41.4 kcal/mol, respectively. Therefore, it was suggested that Ph-Br bond activation is more favorable than the C-H bond activation at the 1st step of the reaction as pointed out in the previous study[8].

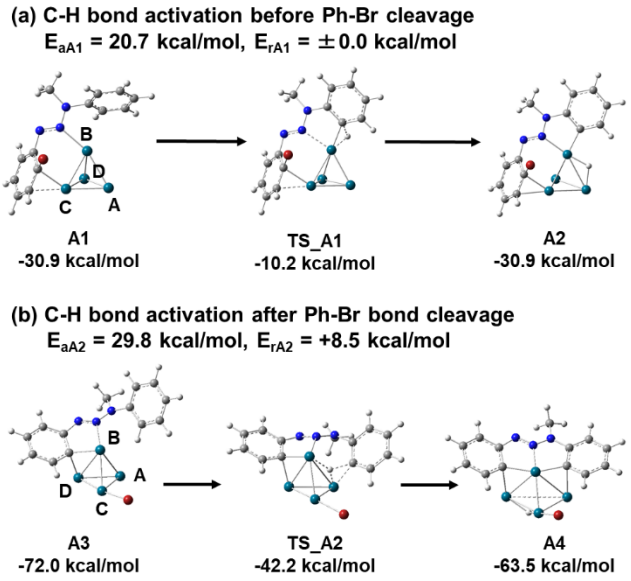

Figure 2. C-H bond activation pathways on the Pd_4 model. (a) C-H bond activation before Ph-Br bond cleavage, (b) C-H bond activation after Ph-Br bond cleavage. Numbers under structure names represent relative potential energies. Reference point of relative potential energy is sum of potential energies of isolated Pd_4 and **1a** molecule. White: hydrogen, gray: carbon, blue: nitrogen, dark red: bromide, blue green: palladium.

3.2 C-H bond Activation on the $Pd_4(OAc)_1$ Model

In this subsection, the effect of OAc ligand for the C-H bond activation was investigated by using the $Pd_4(OAc)_1$ model. As well as the former section, C-H bond activation pathways before or after Ph-Br bond activation were investigated on the $Pd_4(OAc)_1$ model.

First, C-H bond activation at the 1st step of the reaction was investigated. As shown in Figure 3a, C-H bond of **1a** is also activated on the $Pd_4(OAc)_1$ model via five-membered palladacycle intermediate (Figure 3a: B2) generation. In the $Pd_4(OAc)_1$ model, the five-membered pallada cycle structure is also more stable than other non-planer conformations as in the Pd_4 model. Activation energy for this reaction was calculated as 10.0 kcal/mol, and it is lower than that on

the Pd_4 model by 10.7 kcal/mol. In addition, calculated reaction energy of this reaction shows exothermic value (Figure 3a: E_{rB1} = -21.8 kcal/mol) while it was calculated as 0.0 kcal/mol in the Pd_4 model (*cf.* Figure 2a). In this pathway, C-H bond activation takes place on Pd atom on which OAc ligand was not adsorbed. Although C-H bond activation pathway on Pd atom bonded with OAc ligand was also investigated, reactant state of such pathway is unstable than B1 by 7.9 kcal/mol.

Next, C-H bond activation at the 2nd step of the reaction was investigated (Figure 3b). This reaction also proceeds with generating five-membered palladacycle intermediate (Figure 3b: B4). Activation barrier for this reaction was calculated as 9.6 kcal/mol, and it is lower than that on the Pd_4 model by 20.2 kcal/mol. In addition, calculated reaction energy shows exothermic value (Figure 3b: E_{rB2} = -3.3 kcal/mol) while it shows endothermic value in the Pd_4 model (Figure 2b: E_{rA2} = 8.5 kcal/mol). These results suggested that C-H bond activation of **1a** is more favorable in the presence of OAc ligand both from kinetic and thermodynamic points of view.

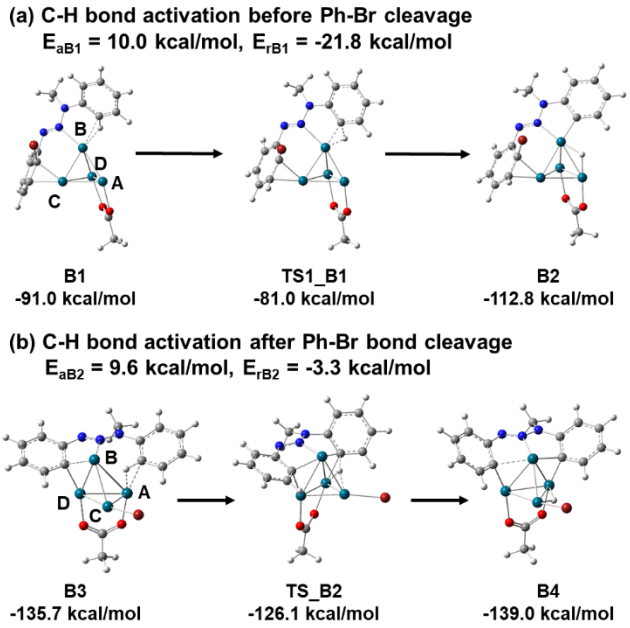

Figure 3. C-H bond activation pathways on the $Pd_4(OAc)_1$ model. (a) C-H bond activation before Ph-Br bond cleavage, (b) C-H bond activation after Ph-Br bond cleavage. Numbers under structure names represent relative potential energies. Reference point of relative potential energy is sum of potential energies of isolated Pd_4, OAc and **1a** molecule. White: hydrogen, gray: carbon, blue: nitrogen, dark red: bromide, blue green: palladium, red: oxygen.

3.3 Analysis for Electronic Effect of OAc ligand

As shown in former sections, C-H bond activation of **1a** is more favorable in the $Pd_4(OAc)_1$ model than that in the Pd_4 model. Therefore, electronic effect of OAc ligand for the C-H bond activation was investigated in this subsection. As shown in Figure 3, distance between C-H bond and Pd is close at the reactant state in the $Pd_4(OAc)_1$ model. Actually, in B1, Pd^B-H distance is 2.13 Å and Pd^B-C distance is 2.43 Å, and in B3, Pd^A-H distance is 1.95 Å and Pd^A-C distance is 2.33 Å, respectively. In addition, C-H bond distance in B1 and B3 are 1.10 Å and 1.12 Å, respectively. These short Pd-H distance and elongated C-H bond are typical configuration of

agostic interaction between C-H bond and Pd atom[49]. C-H bond activation via agnostic-intermediate was also reported in previous theoretical studies for aromatic C-H bond activation by homogeneous $Pd(OAc)_2$ catalyst[22, 25, 26, 29, 30, 35]. On the other hand, C-H bond is far from Pd atoms at the reactant state of the Pd_4 model (Figure 2). In A1, Pd^B-H distance is 2.64 Å and Pd^B-C distance is 2.72 Å, and in A3, Pd^A-H distance is 2.68 Å and Pd^A-C distance is 3.73 Å, respectively. Furthermore, C-H bond distance in A1 and A3 are 1.09 Å. These results suggested that there is no agostic interaction between C-H bond and Pd atom in the Pd_4 model. Even if B1 or B3 without OAc ligand were used as initial structures for geometry optimization, these were optimized to non-agostic conformations. This result suggested that OAc ligand is required for the agotic interaction in this system.

Next, orbital interaction between C-H bond and Pd atoms was investigated by using natural bond orbital (NBO) analysis[50]. Results of the second-order perturbative estimates of donor-acceptor interactions for B3 were shown in Figure 4. Electron donation from C-H σ-bond to Pd^A s-orbital was found in both α and β-spin orbitals (the second-order perturbation energies for this interaction (ΔE) are 8.21 kcal/mol and 6.82 kcal/mol, respectively). This electron donation from C-H σ-bond to Pd s-orbital was also reported in previous theoretical study for the homogeneous $Pd(OAc)_2$ catalyst[35]. Electron back-donation from d-orbitals of Pd^A and Pd^B to C-H σ*-orbital were also found in both α and β-spin orbitals, and back-donation from Pd^A-Pd^B σ-bond to C-H σ*-orbital was found in β-spin orbital. Total ΔE value for these back-donations in α and β-spin orbitals were 4.01 kcal/mol and 4.86 kcal/mol, respectively. These results indicated that there is the agnostic interaction between C-H bond and Pd atoms through these electron donations or back-donations in the $Pd_4(OAc)_1$ model. On the other hand, such donation or back-donation between C-H bond and Pd atoms were not found (ΔE value is less than 1.00 kcal/mol) in A3 (Pd_4

model). Orbital energy of Pd^A s-orbital (acceptor of the donation from C-H σ-bond) in α and β-spin orbitals were calculated as +0.252 hartree and +0.268 hartree in B3, respectively. On the other hand, these were calculated as +0.434 hartree and +0.425 hartree in A3, respectively. These results suggested that empty Pd s-orbital was stabilized in the $Pd_4(OAc)_1$ model compared with the Pd_4 model, and this is one of the reason why the agostic interaction was found only in the $Pd_4(OAc)_1$ model.

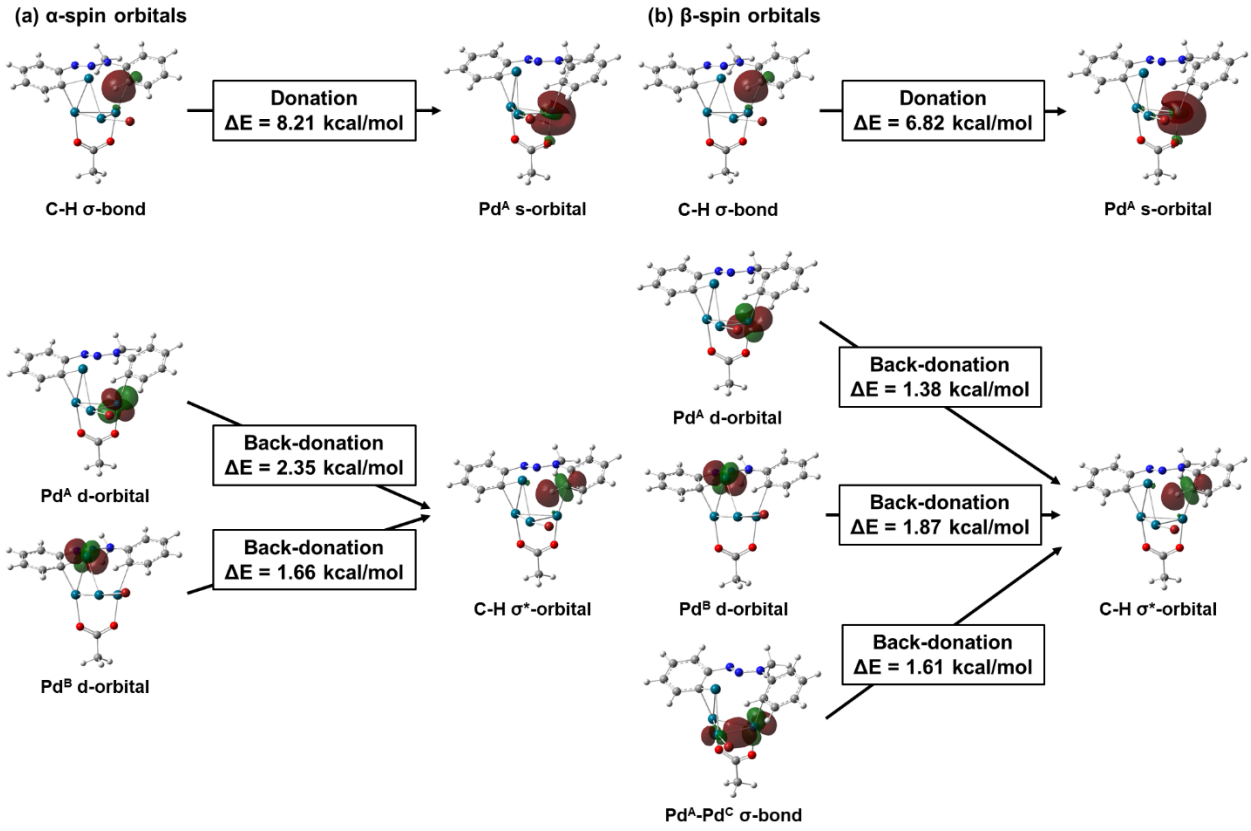

Figure 4. The second-order perturbative estimates of donor-acceptor interactions for B3. ΔE: the second-order perturbation energy for each interaction.

4. Conclusions

The SAPd catalyst is efficient heterogeneous Pd nanoparticle catalyst for N1-substituted benzotriazole synthesis via the 1,7-palladium migration reaction from phenyltriazene. In this study, reaction mechanism for aromatic C-H bond activation of phenyltriazene during the 1, 7-palladium migration reaction on the heterogeneous Pd cluster catalyst was investigated by using DFT calculations. In addition, effect of OAc ligand for the C-H bond activation was also investigated because OAc ligand is an essential factor of the SAPd catalytic system. Aromatic C-H bond of phenyltriazene molecule is activated by the Pd cluster via five-membered palladacycle intermediate generation. This five-membered palladacycle is stable planer conjugated conformation. The C-H bond activation of phenyltriazene is more favorable in the Pd cluster with OAc ligand than that in the Pd cluster without OAc ligand. In the presence of OAc ligand, C-H bond is activated at the reactant state through the agostic interaction between C-H bond and Pd cluster. Based on NBO analysis, it was suggested that empty s-orbital of Pd atom is stabilized due to the interaction between OAc ligand and Pd cluster. This interaction induces electron donation from C-H σ-bond to Pd s-orbital. From these results, it was suggested that the agostic interaction between C-H bond and the Pd cluster induced by OAc ligand is one of the reason why OAc ligand is required for the SAPd catalytic system. This mechanism was also reported in theoretical studies for homogeneous $Pd(OAc)_2$ catalytic system, Therefore, our present study is one of a good example for the relationship of the reaction mechanism between homogeneous catalytic systems and heterogeneous catalytic systems.

REFERENCES

1. Campo, M. A.; Larock, R. C., Novel 1,4-palladium migration in organopalladium intermediates derived from o-iodobiaryis. *J. Am. Chem. Soc.* **2002,** *124* (48), 14326-14327.
2. Campo, M. A.; Huang, Q. H.; Yao, T. L.; Tian, Q. P.; Larock, R. C., 1,4-Palladium migration via C-H activation, followed by arylation: Synthesis of fused polycycles. *J. Am. Chem. Soc.* **2003,** *125* (38), 11506-11507.
3. Huang, Q. H.; Fazio, A.; Dai, G. X.; Campo, M. A.; Larock, R. C., Pd-catalyzed alkyl to aryl migration and cyclization: An efficient synthesis of fused polycycles via multiple C-H activation. *J. Am. Chem. Soc.* **2004,** *126* (24), 7460-7461.
4. Campo, M. A.; Zhang, H. M.; Yao, T. L.; Ibdah, A.; McCulla, R. D.; Huang, Q. H.; Zhao, J.; Jenks, W. S.; Larock, R. C., Aryl to aryl palladium migration in the Heck and Suzuki coupling of o-halobiaryls. *J. Am. Chem. Soc.* **2007,** *129* (19), 6298-6307.
5. Zhao, J.; Yue, D. W.; Campo, M. A.; Larock, R. C., An aryl to imidoyl palladium migration process involving intramolecular C-H activation. *J. Am. Chem. Soc.* **2007,** *129* (16), 5288-5295.
6. Karig, G.; Moon, M. T.; Thasana, N.; Gallagher, T., C-H activation and palladium migration within biaryls under Heck reaction conditions. *Org. Lett.* **2002,** *4* (18), 3115-3118.
7. Masselot, D.; Charmant, J. P. H.; Gallagher, T., Intercepting palladacycles derived by C-H insertion. A mechanism-driven entry to heterocyclic tetraphenylenes. *J. Am. Chem. Soc.* **2006,** *128* (3), 694-695.
8. Zhou, J.; He, J. J.; Wang, B. J.; Yang, W. J.; Ren, H. J., 1,7-Palladium Migration via C-H Activation, Followed by Intramolecular Amination: Regioselective Synthesis of Benzotriazoles. *J. Am. Chem. Soc.* **2011,** *133* (18), 6868-6870.
9. Uyttenhove, C.; Pilotte, L.; Theate, I.; Stroobant, V.; Colau, D.; Parmentier, N.; Boon, T.; Van den Eynde, B. J., Evidence for a tumoral immune resistance mechanism based on tryptophan degradation by indoleamine 2,3-dioxygenase. *Nature Medicine* **2003,** *9* (10), 1269-1274.
10. Chng, L. L.; Zhang, J.; Yang, J. H.; Amoura, M.; Ying, J. Y., C-C Bond Formation via C-H Activation and C-N Bond Formation via Oxidative Amination Catalyzed by Palladium-Polyoxometalate Nanomaterials Using Dioxygen as the Terminal Oxidant. *Adv. Synth. Catal.* **2011,** *353* (16), 2988-2998.
11. Takagi, K.; Al-Amin, M.; Hoshiya, N.; Wouters, J.; Sugimoto, H.; Shiro, Y.; Fukuda, H.; Shuto, S.; Arisawa, M., Palladium-Nanoparticle-Catalyzed 1,7-Palladium Migration Involving C-H Activation, Followed by Intramolecular Amination: Regioselective Synthesis of N1-Arylbenzotriazoles and an Evaluation of Their Inhibitory Activity toward Indoleamine 2,3-Dioxygenase. *J. Org. Chem.* **2014,** *79* (13), 6366-6371.
12. Hoshiya, N.; Shimoda, M.; Yoshikawa, H.; Yamashita, Y.; Shuto, S.; Arisawa, M., Sulfur Modification of Au via Treatment with Piranha Solution Provides Low-Pd Releasing and Recyclable Pd Material, SAPd. *J. Am. Chem. Soc.* **2010,** *132* (21), 7270-+.
13. Hoshiya, N.; Shuto, S.; Arisawa, M., The Actual Active Species of Sulfur-Modified Gold-Supported Palladium as a Highly Effective Palladium Reservoir in the Suzuki-Miyaura Coupling. *Adv. Synth. Catal.* **2011,** *353* (5), 743-748.
14. Al-Amin, M.; Honma, T.; Hoshiya, N.; Shuto, S.; Arisawa, M., Ligand-Free Buchwald-Hartwig Aromatic Aminations of Aryl Halides Catalyzed by Low-Leaching and Highly

Recyclable Sulfur-Modified Gold-Supported Palladium Material. *Adv. Synth. Catal.* **2012,** *354* (6), 1061-1068.
15. Al-Amin, M.; Arai, S.; Hoshiya, N.; Honma, T.; Tamenori, Y.; Sato, T.; Yokoyama, M.; Ishii, A.; Takeuchi, M.; Maruko, T.; Shuto, S.; Arisawa, M., Development of Second Generation Gold-Supported Palladium Material with Low-Leaching and Recyclable Characteristics in Aromatic Amination. *J. Org. Chem.* **2013,** *78* (15), 7575-7581.
16. Al-Amin, M.; Akimoto, M.; Tameno, T.; Ohki, Y.; Takahashi, N.; Hoshiya, N.; Shuto, S.; Arisawa, M., Suzuki-Miyaura cross-coupling reactions using a low-leaching and highly recyclable gold-supported palladium material and two types of microwave equipments. *Green Chem.* **2013,** *15* (5), 1142-1145.
17. Arisawa, M.; Sato, T.; Hoshiya, N.; Al-Amin, M.; Kogami, Y.; Shuto, S., Ligand-Free Suzuki-Miyaura Coupling with Sulfur-Modified Gold-Supported Palladium in the Synthesis of a Conformationally-Restricted Cyclopropane Compound Library with Three-Dimensional Diversity. *ACS Comb. Sci.* **2014,** *16* (5), 215-220.
18. Dyker, G., Palladacycles as reactive intermediates. *Chem. Ber. Recl.* **1997,** *130* (11), 1567-1578.
19. Catellani, M., Catalytic multistep reactions via palladacycles. *Synlett* **2003,** (3), 298-313.
20. Dupont, J.; Consorti, C. S.; Spencer, J., The potential of palladacycles: More than just precatalysts. *Chem. Rev.* **2005,** *105* (6), 2527-2571.
21. Ma, S. M.; Gu, Z. H., 1,4-Migration of rhodium and palladium in catalytic organometallic reactions. *Angew. Chem. Int. Ed.* **2005,** *44* (46), 7512-7517.
22. Biswas, B.; Sugimoto, M.; Sakaki, S., C-H bond activation of benzene and methane by M(eta(2)-O2CH)(2) (M = Pd or Pt). A theoretical study. *Organometallics* **2000,** *19* (19), 3895-3908.
23. Sakaki, S., Theoretical and Computational Study of a Complex System Consisting of Transition Metal Element(s): How to Understand and Predict Its Geometry, Bonding Nature, Molecular Property, and Reaction Behavior. *Bull. Chem. Soc. Jpn.* **2015,** *88* (7), 889-938.
24. Guan, W.; Sayyed, F. B.; Zeng, G. X.; Sakaki, S., sigma-Bond Activation of Small Molecules and Reactions Catalyzed by Transition-Metal Complexes: Theoretical Understanding of Electronic Processes. *Inorg. Chem.* **2014,** *53* (13), 6444-6457.
25. Davies, D. L.; Macgregor, S. A.; McMullin, C. L., Computational Studies of Carboxylate-Assisted C-H Activation and Functionalization at Group 8-10 Transition Metal Centers. *Chem. Rev.* **2017,** *117* (13), 8649-8709.
26. Davies, D. L.; Donald, S. M. A.; Macgregor, S. A., Computational study of the mechanism of cyclometalation by palladium acetate. *J. Am. Chem. Soc.* **2005,** *127* (40), 13754-13755.
27. Sperger, T.; Sanhueza, I. A.; Kalvet, I.; Schoenebeck, F., Computational Studies of Synthetically Relevant Homogeneous Organometallic Catalysis Involving Ni, Pd, Ir, and Rh: An Overview of Commonly Employed DFT Methods and Mechanistic Insights. *Chem. Rev.* **2015,** *115* (17), 9532-9586.
28. Roiban, G. D.; Serrano, E.; Soler, T.; Aullon, G.; Grosu, I.; Cativiela, C.; Martinez, M.; Urriolabeitia, E. P., Regioselective Orthopalladation of (Z)-2-Aryl-4-Arylidene-5(4H)-Oxazolones: Scope, Kinetico-Mechanistic, and Density Functional Theory Studies of the C-H Bond Activation. *Inorg. Chem.* **2011,** *50* (17), 8132-8143.
29. Laga, E.; Garcia-Montero, A.; Sayago, F. J.; Soler, T.; Moncho, S.; Cativiela, C.; Martinez, M.; Urriolabeitia, E. P., Cyclopalladation and Reactivity of Amino Esters through C-H

Bond Activation: Experimental, Kinetic, and Density Functional Theory Mechanistic Studies. *Chem.-Eur. J.* **2013,** *19* (51), 17398-17412.
30. Li, H.; Ma, X. L.; Zhang, B. H.; Lei, M., DFT Study on the Mechanism of Tandem Oxidative Acetoxylation/Ortho C-H Activation/Carbocyclization Catalyzed by Pd(OAc)(2). *Organometallics* **2016,** *35* (19), 3301-3310.
31. Zhang, L.; Fang, D. C., An Explicit Interpretation of the Directing Group Effect for the Pd(OAc)(2)-Catalyzed Aromatic C-H Activations. *J. Org. Chem.* **2016,** *81* (17), 7400-7410.
32. Zhang, L.; Fang, D. C., Explicit roles of diverse directing groups in determining transition state energy and reaction exothermicity of C-H activation pathways. *Org. Chem. Front.* **2017,** *4* (7), 1250-1260.
33. Zhang, L. L.; Zhang, L.; Li, S. J.; Fang, D. C., DFT studies on the distinct mechanisms of C-H activation and oxidation reactions mediated by mononuclear- and binuclear-palladium. *Dalton Trans.* **2018,** *47* (17), 6102-6111.
34. Usui, K.; Haines, B. E.; Musaev, D. G.; Sarpong, R., Understanding Regiodivergence in a Pd(II)-Mediated Site-Selective C-H Alkynylation. *ACS Catal.* **2018,** *8* (5), 4516-4527.
35. Sajjad, M. A.; Harrison, J. A.; Nielson, A. J., NBO Orbital Interaction Analysis for the Ambiphilic Metal-Ligand Activation/Concerted Metalation Deprotonation (AMLA/CMD) Mechanism Involved in the Cyclopalladation Reaction of N,N-Dimethylbenzylamine with Palladium Acetate. *Organometallics* **2018,** *37* (21), 3659-3669.
36. Harrison, J. A.; Nielson, A. J.; Sajjad, M. A.; Schwerdtfeger, P., Evaluation of the Agostic and Syndetic Donations in Aromatic Ring Agostic Interactions Involved in Heteroatom Ligand-Directed C-H Bond Activation. *Organometallics* **2019,** *38* (9), 1903-1916.
37. Cui, Q.; Musaev, D. G.; Morokuma, K., Molecular orbital study of H-2 and CH4 activation on small metal clusters. I. Pt, Pd, Pt-2, and Pd-2. *J. Chem. Phys.* **1998,** *108* (20), 8418-8428.
38. Russell, J.; Zapol, P.; Kral, P.; Curtiss, L. A., Methane bond activation by Pt and Pd subnanometer clusters supported on graphene and carbon nanotubes. *Chem. Phys. Lett.* **2012,** *536*, 9-13.
39. Kozlov, S. M.; Neyman, K. M., Insights from methane decomposition on nanostructured palladium. *J. Catal.* **2016,** *337*, 111-121.
40. Bertani, V.; Cavallotti, C.; Masi, M.; Carra, S., A theoretical analysis of the molecular events involved in hydrocarbons reactivity on palladium clusters. *J. Mol. Catal. A-Chem.* **2003,** *204*, 771-778.
41. Becke, A. D., Density-functional thermochemistry .3. The role of exact exchange. *J. Chem. Phys.* **1993,** *98* (7), 5648-5652.
42. Lee, C. T.; Yang, W. T.; Parr, R. G., Development of the colle-salvetti correlation-energy formula into a functional of the electron-density. *Phys. Rev. B* **1988,** *37* (2), 785-789.
43. Grimme, S.; Antony, J.; Ehrlich, S.; Krieg, H., A consistent and accurate ab initio parametrization of density functional dispersion correction (DFT-D) for the 94 elements H-Pu. *J. Chem. Phys.* **2010,** *132* (15).
44. Andrae, D.; Haussermann, U.; Dolg, M.; Stoll, H.; Preuss, H., Energy-adjusted abinitio pseudopotentials for the 2nd and 3rd row transition-elements. *Theoret. Chim. Acta* **1990,** *77* (2), 123-141.
45. Hehre, W. J.; Ditchfield, R.; Pople, J. A., Self-consistent molecular-orbital methods .12. Further extensions of gaussian-type basis sets for use in molecular-orbital studies of organic-molecules. *J. Chem. Phys.* **1972,** *56* (5), 2257-2261.

46. Harihara.Pc; Pople, J. A., Influence of Polarization Functions on Molecular-Orbital Hydrogenation Energies. *Theoret. Chim. Acta* **1973,** *28* (3), 213-222.
47. Tomasi, J.; Mennucci, B.; Cammi, R., Quantum mechanical continuum solvation models. *Chem. Rev.* **2005,** *105* (8), 2999-3093.
48. M. J. Frisch, G. W. T., H. B. Schlegel, G. E. Scuseria, M. A. Robb, J. R. Cheeseman, G. Scalmani, V. Barone, G. A. Petersson, H. Nakatsuji, X. Li, M. Caricato, A. Marenich, J. Bloino, B. G. Janesko, R. Gomperts, B. Mennucci, H. P. Hratchian, J. V. Ortiz, A. F. Izmaylov, J. L. Sonnenberg, D. Williams-Young, F. Ding, F. Lipparini, F. Egidi, J. Goings, B. Peng, A. Petrone, T. Henderson, D. Ranasinghe, V. G. Zakrzewski, J. Gao, N. Rega, G. Zheng, W. Liang, M. Hada, M. Ehara, K. Toyota, R. Fukuda, J. Hasegawa, M. Ishida, T. Nakajima, Y. Honda, O. Kitao, H. Nakai, T. Vreven, K. Throssell, J. A. Montgomery, Jr., J. E. Peralta, F. Ogliaro, M. Bearpark, J. J. Heyd, E. Brothers, K. N. Kudin, V. N. Staroverov, T. Keith, R. Kobayashi, J. Normand, K. Raghavachari, A. Rendell, J. C. Burant, S. S. Iyengar, J. Tomasi, M. Cossi, J. M. Millam, M. Klene, C. Adamo, R. Cammi, J. W. Ochterski, R. L. Martin, K. Morokuma, O. Farkas, J. B. Foresman, and D. J. Fox, *Gaussian 09, revision E.01* **2016,** *Gaussian, Inc., Wallingford, CT*.
49. Koga, N.; Obara, S.; Kitaura, K.; Morokuma, K., Role of Agostic Interaction in Beta-Elimination of Pd and Ni Complexes - an Abinitio Mo Study. *J. Am. Chem. Soc.* **1985,** *107* (24), 7109-7116.
50. E. D. Glendening, J. K. B., A. E. Reed, J. E. Carpenter, J. A. Bohmann, C. M. Morales, C. R. Landis, and F. Weinhold, NBO 6.0. *(Theoretical Chemistry Institute, University of Wisconsin, Madison, WI, 2013); http://nbo6.chem.wisc.edu/*.

Chapter 6.

General Conclusion

In the present thesis, theoretical studies for understanding activation mechanism of unreactive bonds by metal cluster catalysts are summarized.

In Chapter 2, the role of hydrogen acceptor molecule for the selective aniline synthesis by the Pd cluster catalyst was discussed. Based on the calculated adsorption energies of styrene and imine on both Pd(111) and Pd(100) facets modeled with the Pd_{13} cluster, styrene is adsorbed more strongly on both facets compared than imine is. This result consistently interpreted the experimental result of the competitive hydrogenation of styrene and imine; the preferential adsorption of styrene over imine promotes hydrogenation of styrene more than imine. These results suggested that styrene acts as hydrogen acceptor. On the other hand, the results with the slab model showed opposite adsorption trend in the (111) facet; calculated adsorption energy of imine is larger than that of styrene. The energy decomposition analysis showed that the deformation of styrene on the (111) facet of the slab model is larger than that on the cluster model. This result suggested that edge structure or flexibility of the cluster is important factors for preferential adsorption of styrene on the Pd nanoparticle.

In chapter 3, DFT study on the complete oxidation mechanism of ethylene by the silica supported Pt catalyst was described. Calculated results suggested that ethylene is sequentially oxidized to HCHO via ethylene dioxide intermediate on the edge area of the Pt cluster. In addition, activation energy for the C-C σ-bond cleavage with the silica supported Pt cluster model is smaller than that with bare Pt cluster model. This result was explained by the reservoir effect, in which the siloxide groups take electrons from the Pt moiety, reduces the activation energy of the C-C bond cleavage step by taking electrons from the σ(C-C) orbital. Furthermore, CO_2 and H_2O generation pathways from HCHO were also described. The rate determining step

of the total reaction is CO oxidation step, and this result is consistent with the experimental results.

In chapter 4, C-H bond activation mechanism of piperidone molecule on the Au cluster catalyst was discussed. DFT calculations suggested that Au cluster on the OMS-2 support is negatively charged due to the charge transfer from OMS-2 to the Au cluster. In addition, O_2 molecule which is adsorbed on the negatively charged Au cluster is activated enough to abstract hydrogen atom from piperidone. This is the reason why C-H bond activation by adsorbed O_2 is favorable reaction pathway rather than that directly by Au surface. In addition, activation energy of the C-H bond cleavage by the adsorbed O_2 decreases with more negatively charged Au cluster because the adsorbed O_2 is activated more significantly.

In chapter 5, DFT investigation of the C-H bond activation mechanism on the Pd cluster catalyst was described. From the DFT results, activation energy for the Ph-H bond cleavage reaction decreased in the presence of OAc ligand on the Pd cluster. Because the 5s orbital of Pd is stabilized by the interaction with OAc ligand, electron donation from Ph-H σ-bond to Pd 5s orbital is induced by the Pd cluster with OAc ligand. In addition, electron back-donation from Pd 4d orbital to Ph-H σ*-orbital also occurs. In brief, the Ph-H bond is activated by this agostic-type interaction between the Ph-H bond and the Pd cluster in the presence of OAc ligand.

From these mechanistic studies, some important points for the unreactive bond activation by the metal cluster catalyst were suggested. First, catalytic activity is strongly affected by charge state of the metal cluster. As shown in Chapter 3-5, positively or negatively charged metal cluster can accelerate the unreactive bond activation, which is induced by electronic donation from the unreactive bond to cationic metal or back-donation from anionic metal to anti-bonding orbital of the unreactive bond. Such charge states are generated by the metal-support interaction

or interaction with ligand. In this case, active site is around the interface region between metal cluster and support or ligand. Therefore, search for better combination of metal, support and ligand focused on the charge state of the metal cluster is one of the effective strategies for the new catalyst design.

The second point is structure of the metal cluster. As discussed in Chapter 1 and 2, the structure of the metal surface (facet structure, edge effect, flexibility, and so on) affects the interaction between the adsorbate and the metal cluster. Therefore, both the electronic structure and the atomic configuration of the metal cluster are affected by the support or ligand concertedly.

In this thesis, the author focused on the active site generated by the interaction with other ingredients (e.g. support material). By means of theoretical calculations, the role and nature of the active site for the catalytic reaction were investigated. Although some key findings about the catalytic reaction mechanism are suggested as written in above, more practical proposal for the new catalytic design from the theoretical calculation is the next step of this study. To achieve this goal, more efficient modeling of the catalytic system should be required to fill up the gap between theoretical model and the reaction condition. For example, multi scale modeling and kinetic modeling which can describe the reaction hopping several active sites and its temperature dependence. Because the catalyst design includes not only the selection of materials but also design of the reaction condition, the effect of reaction temperature and pressure should be properly incorporated in the future modelling for efficient catalyst optimization.

Acknowledgements

First of all, I am most grateful for Professor Jun-ya Hasegawa. He supervised my doctoral degree, and always encourages my research. A chemist's view based on molecular science grows through his suggestions and attitude. He gives me a lot of opportunities for growth, and I really glad to study under his teachings.

I would like to thank for my collaborators. The researches in chapter 2 and 4 are collaboration studies with Professor Kazuya Yamaguchi (the University of Tokyo) and co-workers in his laboratory. The research in chapter 3 is a collaboration study with Professor Atsushi Fukuoka (Hokkaido University) and co-workers in his laboratory. He also gave me great suggestions for as advisor of my doctoral degree. The research in chapter 5 is a collaboration study with Professor Mitsuhiro Arisawa (Osaka University) and co-workers in his laboratory. I really glad to join the collaboration studies with them, and they gave me a lot of knowledges and suggestions.

I also would like to thank for Professor Tetsuya Taketsugu and Professor Ken-ichi Shimizu (Hokkaido University). They gave great suggestions for this thesis as advisors of my doctoral degree, and that led improvements of this thesis.

I am grateful for Dr. Naoki Nakatani (Tokyo Metropolitan University). He gave me a lot of knowledges and attitude for research during my bachelor and master degree as assistant professor in Hasegawa laboratory. I really glad to work with him at my early days. I am also grateful for Professor Akira Nakayama (the University of Tokyo). He gave me a lot of great suggestions both for research and my course. He added new insights and ideas to my research as associate professor of Hasegawa laboratory. I also would like to thank for other members of Hasegawa laboratory. In particular, my research life always supported by warm hospitalities of Ms. Yoko Hokaku and Ms. Akiko Doi as secretaries.

Finally, I am grateful for my families. They always encourages and supports my research. I could not do research without their support.

March 25, 2020

Ray Miyazaki